UNIVERSITÄTSKLINIKUM HAMBURG-EPPENDORF

Klinik und Poliklinik für Neurologie
Univ-Prof. Dr.med. Tim Ullrich Magnus

Engineered Nanoparticles with Recombinant Thrombolytic Agents for Targeted Drug Delivery in Ischemic Stroke with Magnetic Particle Imaging (MPI) and the Development and Characterization of optimized MPI Tracers

zur Erlangung des Doktorgrades PhD
an der Medizinischen Fakultät der Universität Hamburg.

vorgelegt von:

Javier Rández Garbayo
aus Cintruénigo, Spanien

Hamburg 2025

(wird von der Medizinischen Fakultät ausgefüllt)

Angenommen von der
Medizinischen Fakultät der Universität Hamburg am: 03. 11.2025

Veröffentlicht mit Genehmigung der
Medizinischen Fakultät der Universität Hamburg.

Prüfungsausschuss, der/die Vorsitzende:
Prof. Dr. med. Tim Magnus

Prüfungsausschuss, zweite/r Gutachter/in:
Prof. Dr-Ing. Tobias Knopp

Table of contents

Background and motivation

Over the past few decades, the importance of early disease detection and prevention has gained considerable attention (Beyer et al., 2021; Dalla Palma, 2006; Gunderman, 2005). Early diagnosis plays a pivotal role in improving treatment outcomes and is essential for effective patient management (European Society of Radiology 2009, 2010; ‘Medical Imaging in Personalised Medicine’, 2015). The advancement of medical technologies, particularly imaging, has revolutionized how healthcare providers monitor and visualize internal body structures. This non-invasive approach offers detailed, multi-dimensional data for diagnosis, monitoring, and prognosis (Kasban, El-Bendary, & Salama, 2015; Kherlopian et al., 2008), enabling better disease management and personalized care (Liu et al., 2010).

The rise in medical imaging modalities over recent years has introduced techniques tailored to specific diagnostic applications. These imaging modalities are based on different physical principles, each offering unique benefits for disease detection (Kasban et al., 2015; Kherlopian et al., 2008). A significant milestone in the field was reached in 2005 when Gleich and Weizenecker introduced Magnetic Particle Imaging (MPI) (Gleich & Weizenecker, 2005). This emerging modality offers a unique set of advantages, particularly in cases where conventional imaging methods like MRI, CT, or PET might not be optimal. MPI works by detecting superparamagnetic nanoparticles, commonly iron oxide particles, in real-time, with high sensitivity and temporal resolution. Importantly, the magnetic fields used in MPI are safe for patients, and the nanoparticles themselves are biocompatible, stable, and cleared naturally by the liver (Juergen Weizenecker, Gleich, & Borgert, 2008). In addition to its imaging capabilities, MPI allows for the steering of nanoparticles via magnetic force (Griese et al., 2020) and the extraction of functional information such as temperature and viscosity from the imaging data (Szwargulski et al., 2020).

Over the last 15 years, MPI has demonstrated promising potential in several medical applications, including vascular imaging, cell tracking, and disease detection, specifically ischemic stroke (Ludewig et al., 2017; Szwargulski et al., 2020; Zhou et al., 2018). In ischemic stroke, a blood clot blocks a cerebral artery, leading to reduced oxygen supply in the affected brain region. Typically, medications delivered through the bloodstream may not reach the infarct site in sufficient concentrations to dissolve the clot and restore blood flow. This challenge makes the case for exploring MPI's potential not just for improving stroke diagnosis but also for delivering targeted therapy. The objective of this thesis is to investigate the ability of MPI to accelerate stroke diagnosis while enabling treatment via MPI-targeted therapy. Our first goal is to immobilize magnetic nanoparticles (MNP) used in MPI with thrombolytic agents, using MPI's magnetic navigation capabilities to direct the nanoparticles to the infarct core. This targeted approach simulates a real-world ischemic stroke scenario, with the goal of achieving localized thrombolysis of the clot.

As MPI continues to evolve toward clinical applications, several hardware advancements are underway to enable imaging at a human scale. However, these advancements require the development of customized MPI tracers to fully harness the modality’s potential. Iron oxide nanoparticles, which can be synthesized through various chemical processes such as co-precipitation, microemulsion, or thermal decomposition (Mosayebi, Kiyasatfar, & Laurent, 2017; Teja & Koh, 2009), still face challenges in terms of reproducibility and precise control over particle size and shape. Additionally, the synthesis process often requires ligand exchange reactions to stabilize nanoparticles in aqueous media (Turcheniuk, Tarasevych, Kukhar, Boukherroub, & Szunerits, 2013). One promising alternative that addresses many of these challenges is the use of magnetosomes, biogenic magnetic nanoparticles synthesized by magnetotactic bacteria. These magnetosomes offer a biogenic solution to the difficulties of particle synthesis and have been shown to possess exceptional characteristics for MPI tracers. The second part of this thesis focuses on developing and investigating genetically engineered magnetosomes with varying morphological and magnetic characteristics, ultimately seeking the optimal MPI tracer for improved imaging performance.

1. Introduction

1.1. Medical imaging

Medical images account for about 90% of all healthcare data ("The Digital Universe Driving Data Growth in Healthcare", published by EMC, with research and analysis from IDC (12/13)), which undoubtedly become one of the most critical sources of evidence for clinical diagnosis, analysis and medical intervention. Medical imaging is a very active field, that uses non-invasive technology that acquires signals by physical principles such as sound, light and electromagnetic waves among others. It also refers to the image analysis methods and the interpretation of medical data that involves the extraction of image information such as color, texture and shape. The first developed imaging modalities are in the morphological technology field. They use either sound waves or a specific range of the electromagnetic spectrum to receive structural information about biological tissue directly.

X-Ray and Computed Tomography

The oldest non-invasive method, X-ray radiography, employs an X-ray apparatus to create a tiny quantity of ionizing or non-ionizing radiation. A latent picture of the internal body structures on an X-ray film is created (Doi Kunio, 2006; Filler, 2009). The improved version of X-Ray is Computed Tomography (CT) imaging. CT uses cross-sectional X-ray images taken from different angles, making a 3D image reconstruction of complex body structures and acquiring volumetric data. CT has dramatically impacted the monitoring and detection of various types of cancers, such as skeleton, kidney, and bladder (Hodson, Husband, & Macdonald, 1979; Levine et al., 1979). It also can identify metastases to the brain, liver, and lungs (Alfaraj, Al Dahlawi, AlObaid, Aldukhayyil, & Al Rumaih, 2022; LeRoux, Berger, Elliott, & Tamimi, 1991). The impact of radiation that increases the possibility of developing cancer in life is still controversial (Hussain et al., 2022; Kasban et al., 2015).

Ultrasonography

Ultrasound (US) is a well-established anatomical and physiological clinical imaging technology based on scanning small parts or intra-operative, operating with a frequency between 10 and 20 MHz. The different frequencies of the reflection wave result from the mechanical properties of various soft tissue structures that can be measured and transformed into an essentially 2D real-time image (Moran & Thomson, 2020). Many electronics and technologies could manipulate ultrasound frequencies. Therefore, compared to other techniques, US imaging rapidly became a standard bedside, low-cost, free radiation, and painless clinical diagnosis imaging modality. Conversely, it has a lower specificity and spatial resolution than CT and Magnetic Resonance Imaging (MRI). The US is mainly used to image organs of the abdomen, glands, echocardiography, and the development of the fetus during pregnancy, among others (Kasban et al., 2015; Moran & Thomson, 2020).

Nuclear Medicine

In nuclear medicine, radiolabeled tracers are injected and monitored. Nuclear medicine's molecular imaging can be combined with other imaging modalities, such as MRI, to manage patients (Massoud & Gambhir, 2003).

Positron Emission Tomography (PET) is a nuclear medicine imaging technique that provides functional information at cellular and molecular levels, based on the use of radioactive isotopes that generate a positron decay for tracking physiological processes such as protein-protein interaction, tissue blood flow, metabolism, neurotransmitter activity, and cell death, among others (Phelps, 2000). The total concentration of target-specific radiotracers intravenously injected contributes to determining normal and disease-related states of tissue function and response to treatment (Crișan et al., 2022). The most common molecule applied in PET is fluorodeoxyglucose (FDG), which has radioactive fluorine and is readily taken up by tumors (Buck et al., 2003). Further positron-emitting isotopes frequently used are labeled Carbon-11, Nitrogen-13, Oxygen-15, and Fluorine-1 (Crișan et al., 2022).

Single Photon Emission Computed Tomography (SPECT) shares many features with PET, as the information provided is related to the metabolism of diseases. However, the isotopes used in SPECT imaging are decayed by gamma emission (Massoud & Gambhir, 2003). Using combined modalities like PET/CT devices and SPECT, functional processes can be localized within the body to enhance the accuracy of diagnosis for different types of cancers (breast, cervical, colorectal, head, lung…) and cardiovascular and neurological diseases (Buck et al., 2003; Ciernik et al., 2003; Joseph & Singh, 2023; Padma et al., 2003). PET is considered a more robust technique than SPECT for imaging because positron isotopes can be substituted for naturally occurring atoms for most molecular events. However, using radioactive materials makes this technique risky in handling the tracers and makes the patient radioactive for a variable period (Hussain et al., 2022). Moreover, it is an expensive modality with a relatively low spatial resolution (Crișan et al., 2022; Kasban et al., 2015).

1.1.1. Magnetic Imaging Techniques

The arrival of Magnetic Imaging Techniques (MIT) emerged as a revolutionary field due to their accuracy and safety. Progress in MIT scanning capabilities enabled medical diagnostics to achieve real-time imaging, higher sensitivity detection, and higher resolution images, resulting in better prognosis (Mukhatov, Le, Pham, & Do, 2023). The two primary modalities of magnetic imaging scanners are Magnetic Resonance Imaging (MRI) and Magnetic Particle Imaging (MPI).

Magnetic Resonance Imaging (MRI)

MRI was the most attractive scanning modality using frequency fields, providing non-invasive 3D body pictures of soft tissues and monitoring body chemistry. The three main components of MRI scanners are: first, a permanent magnet that generates a solid homogenous magnetic field. Secondly, a radio frequency (RF) part that comprises two coils: one transmitter coil to generate a revolving magnetic field for exciting a spin system and a receiver coil to convert the processing magnetization into electrical pulses. The MRI scanner's third part is a magnetic field gradient system composed of three orthogonal gradient coils for signal localization. MRI showed great applications for the detection of multiple sclerosis (Filippi et al., 2011), CNS injuries (Sinnecker et al., 2015), infections (Rangarajan, Das, Kumar, & Gupta, 2014), tumors (Filler, 2009), degradations and injuries in ligaments and muscles (Kalia, Leung, Sneag, Del Grande, &

Carrino, 2017), occlusion of blood vessels (Choyke et al., 1985), and bone tumors (Nascimento, Suchard, Hatem, & de Abreu, 2014). Nevertheless, MRI is expensive for its low sensitivity and time-consuming image scanning and processing. Furthermore, it cannot detect anomalies of intraluminal body parts, and sometimes, sedation may be required for patients who cannot remain still (Kasban et al., 2015).

Functional MRI (fMRI) is a modality of MRI used for mapping brain activity in response to a specified stimulus. The region of the brain that is stimulated increases oxygenated hemoglobin and the MRI image contrast changes due to the diamagnetic behavior of the oxygenated hemoglobin. With fMRI, we are able to measure tiny metabolic changes within the brain during activity (Glover, 2011).

Magnetic Particle imaging (MPI)

Magnetic Particle Imaging (MPI) is a cutting-edge tomographic imaging technique that leverages the magnetic properties of superparamagnetic nanoparticles to generate high-resolution, real-time 3D images without exposing the patient to radiation. Unlike MRI, which measures the magnetic properties of protons, MPI directly detects the spatial distribution of MNP within a target area. MPI is known for its excellent sensitivity, rapid temporal resolution (up to 46 Hz), and ability to visualize dynamic processes, making it particularly suited for vascular imaging and targeted therapies (Szwargulski et al., 2020).

The MPI system (Fig.1, top) consists of several key components, including electromagnetic coils that generate the drive field, receive coils that detect changes in magnetization, and selection coils that create a highly inhomogeneous magnetic field, known as the field-free point (FFP) or field-free line (FFL). The FFP or FFL is a critical aspect of MPI, as it spatially encodes the MNP's location and facilitates the creation of an image.

In MPI, superparamagnetic nanoparticles, typically iron oxide, are exposed to oscillating magnetic fields. These particles exhibit nonlinear magnetization behavior, which enables their detection through the harmonic signals they generate in response to the drive field. Importantly, MPI is a "background-free" imaging technique, meaning that only the MNP contribute to the signal, while biological tissues do not, resulting in high-contrast images (Szwargulski et al., 2020).

One of MPI’s distinguishing features is its ability to steer nanoparticles using magnetic forces, allowing for targeted drug delivery and localized therapies. Moreover, MPI offers functional imaging capabilities, such as measuring temperature and viscosity within the targeted area. These features open the door for multi-contrast applications (Fig.1 lower part), which can potentially enhance diagnostics and therapeutic interventions (Möddel, Meins, Dieckhoff, & Knopp, 2018; Salamon et al., 2020).

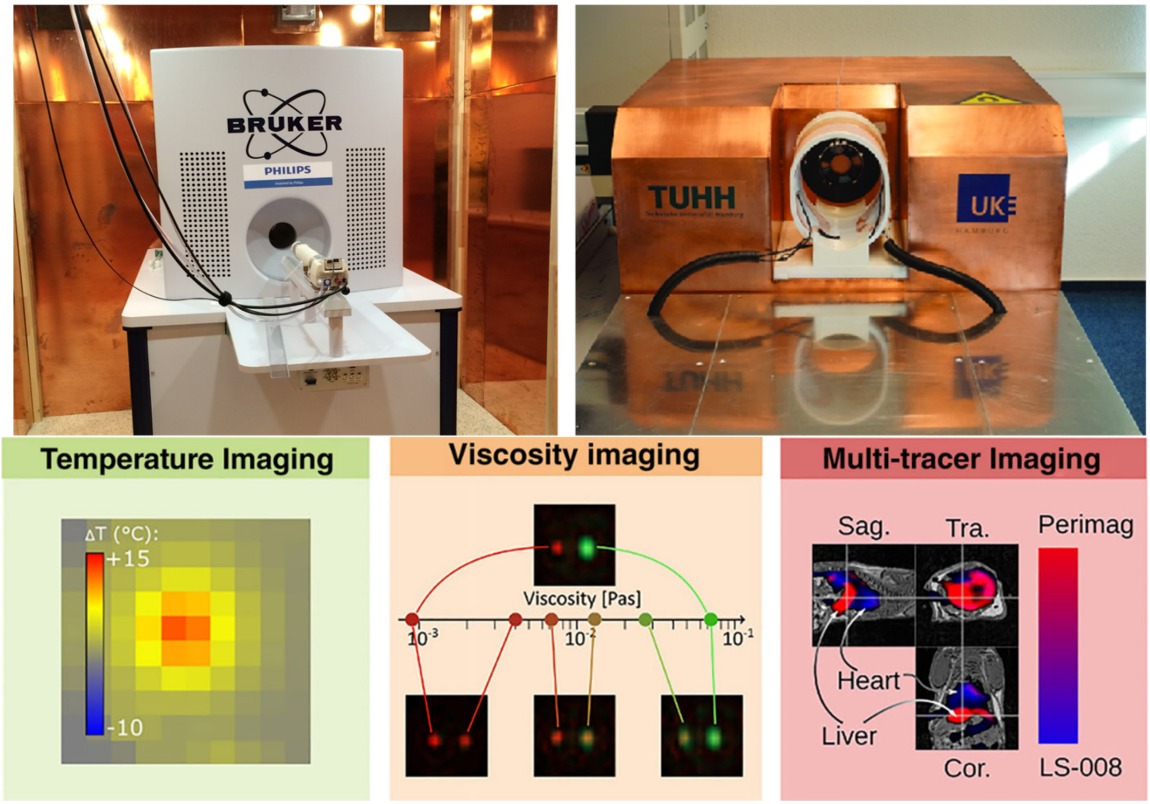

Figure 1. **Present MPI scanners and multi-contrast applications**. Upper part: Preclinical Bruker/Philips MPI scanner (left) and human head MPI scanner (right). Lower part: Application fields of multi-contrast MPI for the determination of additional information such as viscosity temperature (Salamon et al., 2020) left, (Möddel et al., 2018) (middle) and multitracker imaging (Szwargulski et al., 2018) (right). Modified picture from Ludewig,…Rández-Garbayo, et al., 2021).

In the past 20 years, MPI has progressed considerably in equipment development, magnetic particle preparation, and reconstruction algorithm research (Yin et al., 2022). Researchers have reported that MPI has one hundred times higher gradient strength than standard MRI machines and, therefore, significantly higher force and better navigation performance (Saritas et al., 2013). MPI has been successfully applied in our group in cardiovascular and cerebrovascular imaging (Ludewig et al., 2017). These promising achievements lead us to focus this doctoral thesis on using MPI research for biomedical imaging applications. Table 1 compares the performance of different imaging techniques that are discussed.

Table 1. Overview of imaging modalities and their main characteristics.

Modality	**Ultrasound**	**CT**	**MRI**	**PET**	**SPECT**	**MPI**
Main clinical application	Structural imaging	Structural imaging	Structural imaging	Tracer imaging	Tracer imaging	Tracer imaging
Spatial resolution	1 mm	<1 mm	1 mm	4 mm	3-10 mm	1 mm
Temporal Resolution	<1 second	Seconds	Seconds to hours	minutes	minutes	<1 second to minutes
Contast agent/tracer	Microbubbles	Iodine	Gadolinium, iron oxide particles	Radioactive tracers	Radioactive tracers	iron oxide particles
Sensitivity	Low	Low	Low	High	High	High
Depth	Low	High	High	High	High	High
Radiactivity	No	Yes	No	Yes	Yes	No
Patient risk	Heating and cavitation	Radiation	Heating and peripheral nerve simulation	Radiation	Radiation	Heating and peripheral nerve simulation
Cost	Low	Medium	High	High	Medium	Medium

Cost is based on the purchase price of imaging systems in the United States. Low cost: < 100.000 US $. Medium cost: 100.000-300.000 US $. High cost: >300.000 US $. Low Depth <10 cm. High depth: >50 cm. Following references (Hahn, Singh, Sharma, Brown, & Moudgil, 2011; Weissleder & Pittet, 2008)

1.2. Basic principles of Magnetic Particle Imaging (MPI)

1.2.1. Magnetic nanoparticles

MPI is a background-free imaging technique that heavily relies on tracking the spatial distribution of superparamagnetic components, and for that reason, the tracer material and its magnetic performance are crucial to create an image. Superparamagnetic iron oxide nanoparticles (SPIONs) have emerged as the most utilized magnetic nanoparticles for MPI applications because of their relatively easy synthesis, stability at room temperature, and high biocompatibility properties. To be more concrete, SPIONs consist of a small crystal phase, with a diameter range between 10 and 100 nm of synthetic magnetite (Fe_3O_4) or maghemite (γ-Fe_2O_3) core responsible for its magnetic behavior, and a magnetically neutral coating. When the particle coating is sufficiently thick, it prevents agglomeration of the particles avoiding particle-particle interactions and making each particle to behave as a single magnetic domain. At this point, SPIONs behave superparamagnetic, which allows for the most significant contribution to signal differentiation and detection in MPI (Biederer et al., 2009; Ferguson, Minard, & Krishnan, 2009). To address the magnetic properties of these particles in MPI, we must first describe their structure and characteristics. The characteristically desired structure of MPI tracers includes critical parameters such as the size and shape of the magnetic core with high monodispersity, and magnetic properties such as superparamagnetism, a short magnetic relaxation time, and high magnetic saturation, which are highly important for the signal generation (Bauer, Situ, Griswold, & Samia, 2015; Tomitaka et al., 2015).

1.2.2.Magnetic properties of superparamagnetic nanoparticles

To understand the behavior of a magnetic particle in typical MPI oscillating magnetic fields, we first consider the distinct types of magnetism in static magnetic fields. The magnetic moment, defined as the magnetic behavior of each particle, exhibits a parallel alignment of the atoms in ferromagnetic materials. The density of all magnetic moments is called magnetization, and the magnetization of ferromagnetic materials remains once exposed to a magnetic field. This magnetic property information can be extracted from its hysteresis loop, representing the relationship between the induced magnetic flux density (B) on the particles and the magnetizing force (H) generated by an external magnetic field. The hysteresis behavior of ferromagnetic materials is shown in Fig.2 left, where it is described by the magnetic saturation of the particles from a zero-field value, followed by a reduction of the magnetic field that comes with a different path back. Once again, when the magnetization reaches the magnetic field strength of zero, it has an offset to the starting magnetization, the so-called retentivity. When the magnetization reaches the opposite saturation by increasing the magnetic field, the coercivity is reached by crossing the x-axis. Coercivity is defined as the resistance of a magnetic material to change in magnetization when exposed to an external magnetic field. When the magnetic field reaches the opposite saturation and it is increased again, the hysteresis loop is completed symmetrically.

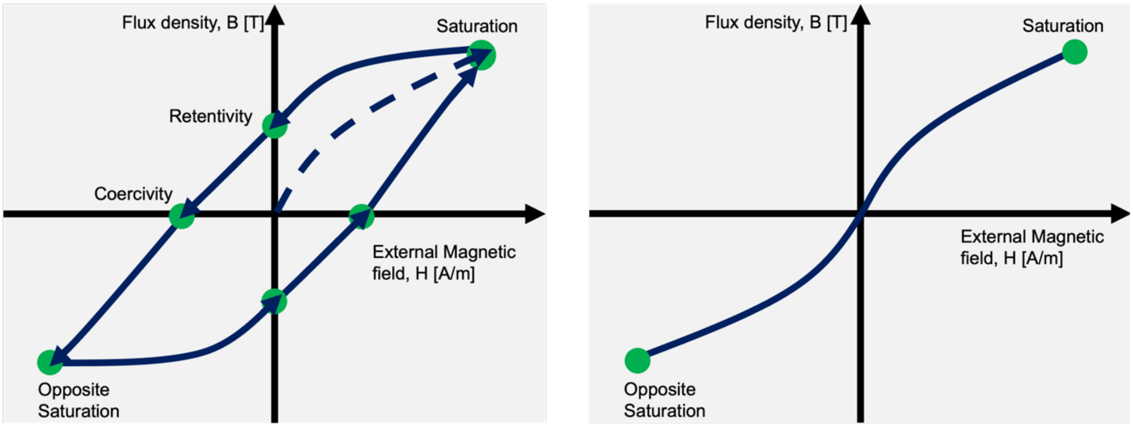

Figure 2. Sketch of the response of magnetic particles in terms of magnetic moment B (T) as a function of the external magnetic field H (A/m). Magnetization comparison of hysteresis curves for ferro- and superparamagnetic particles. (Left) Hysteresis behavior of ferromagnetic particles. (Right) Arrows indicate the direction of the transition. Hysteresis behavior of superparamagnetic particles following Langevin theory.

The denomination of superparamagnetism refers to a singular type of magnetism shown on small ferromagnetic nanoparticles. As a result, the magnetic core diameter must be below a threshold of 50 nm (Bauer et al., 2015; Ferguson et al., 2009). Superparamagnetic nanoparticles comprise a single ferromagnetic core domain whose magnetic moments align with the exposed magnetic field. Contrary to ferromagnetic, superparamagnetic materials do not show remanence magnetization when an external magnetic field is removed; the magnetic moments of the domains are randomly aligned again, and the net magnetic moment of this substance is zero. Therefore, the magnetization curve of superparamagnetic materials has no area in the hysteresis loop (Fig.2 right); the curve always follows the same track when an external magnetic field is increased and decreased, with non-linear behavior.

Another essential characteristic is the magnetic susceptibility of superparamagnetic nanoparticles, which determines how well a material can be magnetized within an external magnetic field, which is much larger than the paramagnetic but lower than ferromagnetic materials. In the case of magnetite, it is 70, which is reasonably high compared to other iron oxides such as hematite (0.0014) (Dar & Shivashankar, 2013). An additional significant parameter for superparamagnetic particles is the Curie Temperature (T_c). It is a material-dependent threshold temperature at which ferromagnetic materials lose their spontaneous magnetization and become paramagnetic. Therefore, all particles used in MPI must have a Curie Temperature far above the body temperature (37 ºC), which for SPION is expected to be above 426 ºC (or 699 K) (Levy, Giustetto, & Hoser, 2012).

To understand the sensitivity and the resolution within MPI performance, the relevance of the magnetization dynamics of the particles determined by the magnetic relaxation must be reviewed. When we apply a magnetic field on superparamagnetic material, its magnetization vector follows the direction of the applied field with certain delay. This delay is described as the relaxation time of the magnetic material and it is directly linked to the effective magnetic moment of the particle. Magnetic relaxation depends on the frequency applied, the particle size, magnetic anisotropy, hydrodynamic volume, and the viscosity of the media, among others. When the nanoparticles are in a liquid suspension under an external magnetic field, there are two rotation mechanisms for magnetic relaxation they can freely perform. The Néel and the Brownian relaxation, shown in Fig.3, can occur for the SPION in MPI on a timescale of nanoseconds. The Néel relaxation occurs when the internal magnetic moment of the particle rotates from one orientation to another without physical rotation of the particle, and it depends exponentially on the magnetic core. Néel relaxation dominates on particles in a liquid carrier medium (deionized water) as well as in a solid matrix. On the other hand, the Brownian rotation is based on the physical reorientation of the whole particle, affected linearly by the hydrodynamic particle volume. Consequently, in lower frequencies, if the suspension is enough viscose, Brownian relaxation will dominate, while in higher frequencies Néel relaxation will be dominant. Both mechanisms concur simultaneously, but the shorter of both relaxation times determines the total relaxation time. The progression from Néel to Brownian depends on the particle anisotropy, and the viscosity of the particles' suspension. However, Néel relaxation is prevalent in MPI particles, as the particle sizes are <50 nm with high anisotropy, whereas Brownian rotation dominates for larger core size SPION.

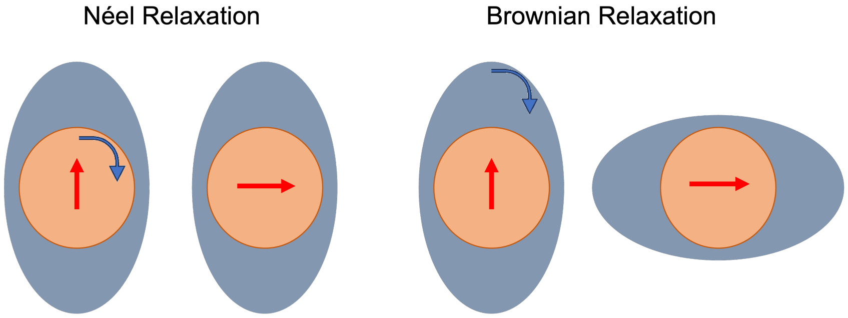

Figure 3. Néel rotation/relaxation (left). Brownian rotation/relaxation (right).

1.2.3. Generation of the particle signal

The principle of how the particles can be excited under the MPI oscillating magnetic fields and their magnetization response with a characteristic signal is complex. In this section, the signal generation in MPI is explained based on the presence of an external sinusoidal magnetic field, the so-called excitation or drive field, using send coils. The drive field is usually homogeneous in space, and all particles in a certain area of interest experience the same field. The magnetization curve of the particles by applying a time-dependent sinusoidal magnetic field is shown in Fig.4A. Its magnetization can be divided into a saturation part, where the magnetization is constant even when the applied field is increased, and a dynamic part, which shows a sharp increase under the applied drive field (see Fig.4B). The amplitude of the drive field must be sufficiency high to change the particles' magnetization within the non-linear areas of the magnetization curve, ideally in the vicinity of the saturation regions. The Langevin function in Fig.4A describes the magnetization of a single-domain MNP in a simplified manner, with the assumption that the particles are always in thermal equilibrium.

To detect the change in particles' magnetization based on changing the flux density, MPI measures the voltage induced in the receive coils (Fig. 4C). This magnetization progression in Fig.4C approaches a constant function when the drive field proceeds to higher field strengths, and the magnetization only flips its direction when the drive field changes in sign. The time-dependent magnetization of the particles within the dynamic region is detectable through a voltage signal with the help of Faraday's law of induction, shown in Fig.4D. One can see sharp peaks in the induced voltage signal whenever the magnetization rapidly changes and the particles flip their direction.

As the relationship between the drive field and the magnetization progression is non-linear, it creates disturbances in the induced particles' signal, which can be decomposed in harmonics and guarantee that both signals can be discriminated. On the contrary, particles with linear magnetization response would have the same frequency as the excitation frequency, and, as a result, no harmonics would be obtained from the particles' signal (Wawrzik, Ludwig, & Schilling, 2012). The initial excitation frequency is filtered out of the recorded signal since it is covered by the excitation signal. In addition, excluding the fundamental frequency potentially removes any background signal induced by the iron in the human body. The remaining unmasked higher harmonics of the particles are transformed into Fourier space, illustrated in Fig.4E, the basis of the raw MPI signal. The intensity of these higher harmonics and their amplitude are proportional to the concentration of MNP. Therefore, the performance of the particles depends on the signal strength above the noise level and the decay of the harmonic amplitudes; the higher the harmonic signals, the longer they can be detected and differentiated from the magnetic field frequency applied.

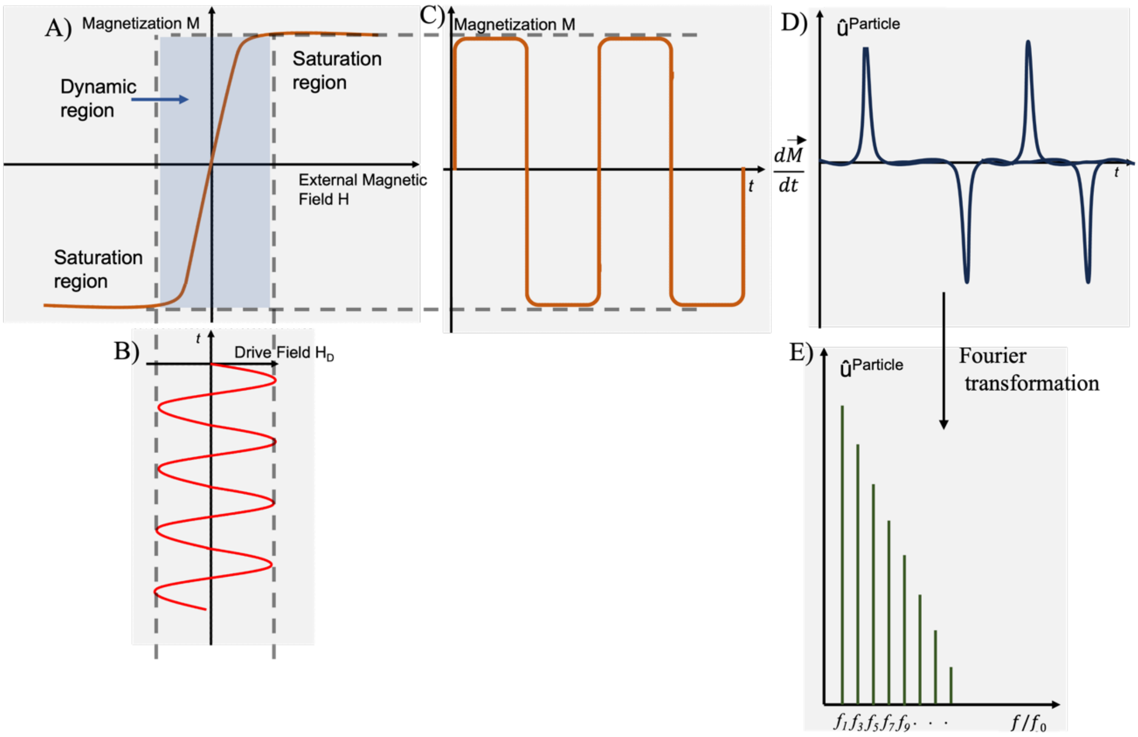

Figure 4. The basic principle of signal generation in MPI; non-linear magnetization progression and induced signal for a superparamagnetic material and sinusoidal drive field. (A) The non-linear magnetization curve of superparamagnetic particles modeled by the Langevin function. (B) A time-dependent sinusoidal magnetic field is used to excite non-saturated particles. (C) Periodic alternating magnetization behavior evoked by the sinusoidal drive field. (D) The voltage signal is induced by the magnetization change of the particle. (E) The responding time signal of the particles is transformed into Fourier space and its spectrum.

Increasing the drive field strength when the particles are saturated, will not change the particle magnetization, but it plays a major role in spatial encoding.

1.2.4. Spatial encoding

When the drive field has enough amplitude to penetrate the volume of interest, MPI can easily exhibit whether magnetic material is present or not. However, it is not possible to determine where this emitted signal is coming from and how much magnetic material is present at this particular point. In order to localize the particles at different positions within an area (spatial encoding), MPI generates a static magnetic field, which is highly inhomogeneous in space. This static inhomogeneous gradient magnetic field, the so-called gradient field, can be generated by a pair of permanent magnets or coils in Maxwell configuration. The opposing magnetic fields compensate for each other by developing one special location, the field free point (FFP) or the field free line (FFL), which is exclusively characterized by a magnetic field magnitude being zero. This zero-field area can be encoded to obtain the spatial distribution of the tracers within the selected field of view (FoV). When applying a strong gradient magnetic field to an area containing magnetic nanoparticles, these concomitant particles will be magnetically saturated in most positions in space. Uniquely within the selected small region around the FFP, the particles will be at zero magnetization, but with the possibility of being magnetizable within the dynamic range of the magnetization curve. When the drive field is superimposed on top of the gradient field, the particles with enough distance away from the FFP are saturated and do not react to the change of the total magnetic field (see Fig.5A and 5B). As a consequence, almost no MPI signal is induced in the receive coil (Fig. 5C-E). On the opposite way, only the particles within the FFP area experience a strong magnetization change by the drive field, flipping back and forth, as it is described in the previous *section 1.2.3.* This magnetization change leads to a measurable voltage signal in the receive coil, which has a direct relation to the FFP location achieving the spatial encoding. It is worth to mention that the drive field amplitude has to be smaller than the gradient field, otherwise saturated particles could magnetize again and contribute to the measurement signal. The size of the FFP or FFL area determines the resolution and sensitivity, therefore, FFL scanners are more sensitive since they allow us to examine more significant regions compared to FFP scanners. Since with the applied gradient field is possible to select the position at free to magnetize, it is also called the selection field in the MPI context.

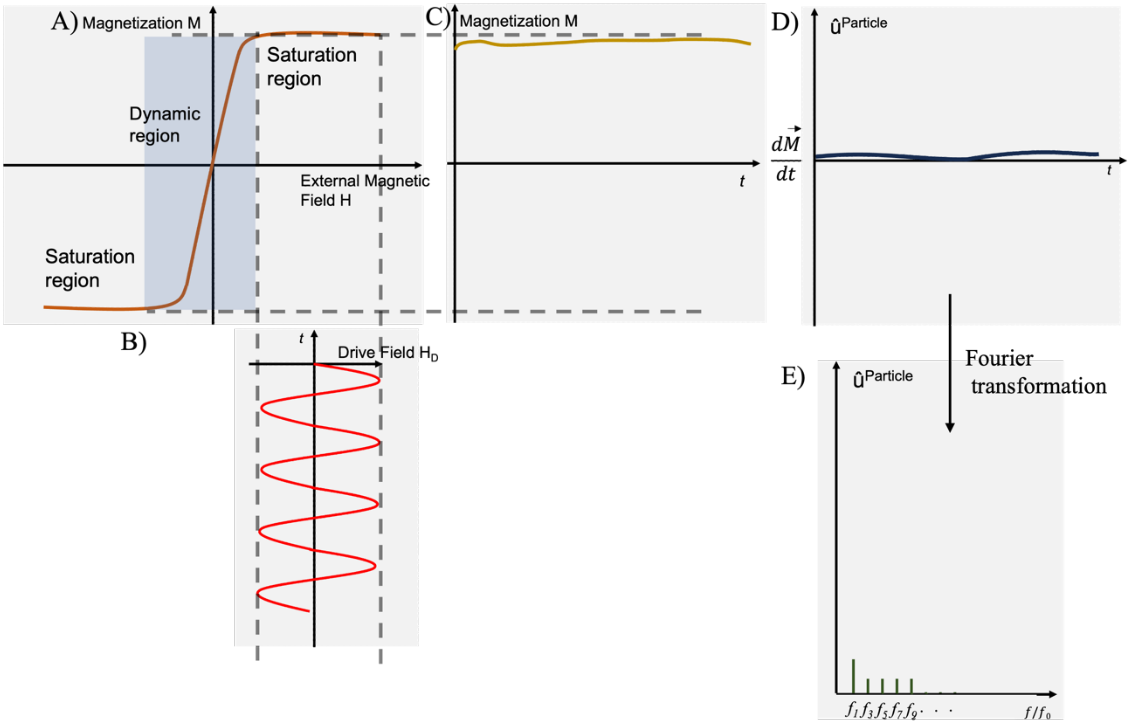

Figure 5. Particle response to a sinusoidal magnetic field with high offset. (A) The non-linear magnetization curve of superparamagnetic particles modeled by the Langevin function is saturated under a solid, constant magnetic field. (B) A time-dependent sinusoidal magnetic field is used to saturate particles. (C) The strong sinusoidal drive field evokes non-magnetization behavior. (D) The voltage signal of the particles' is transformed into Fourier space, and the spectrum of the particle signal results in noise in all frequencies. Hence, no signal is induced in the receive coil.

1.2.5. The system matrix, from data to image reconstruction

For the aim of MPI to determine the mapping of the spatial distribution of the particles, it is essential to pattern the relation between the induced signal and the particle distribution. It is not possible to determine the exact position of a particular particle using MPI, due to the nanometer particle size. Instead, MPI represents a map of the spatial particle concentration, which is defined as the number of particles per volume. MPI images are usually displayed as grey-scale images, where white indicates high particle concentration and in turn, black denotes no particles concentrated at that place (Fig.6 lower part).

The System Matrix (SM) based reconstruction approach was performed in this work. The SM procedure is a calibration-based technique in which the magnetization response of the MNP is measured. The magnetization response of a sample containing a known amount of magnetic material is determined using the system response distribution in all possible spatial positions of voxel within the FoV (Fig.6 Top). Usually, a robot arm operates the sample allocation in accurately defined positions. The combination of the harmonics' spectra of those measurements within the spatial points defines the SM.

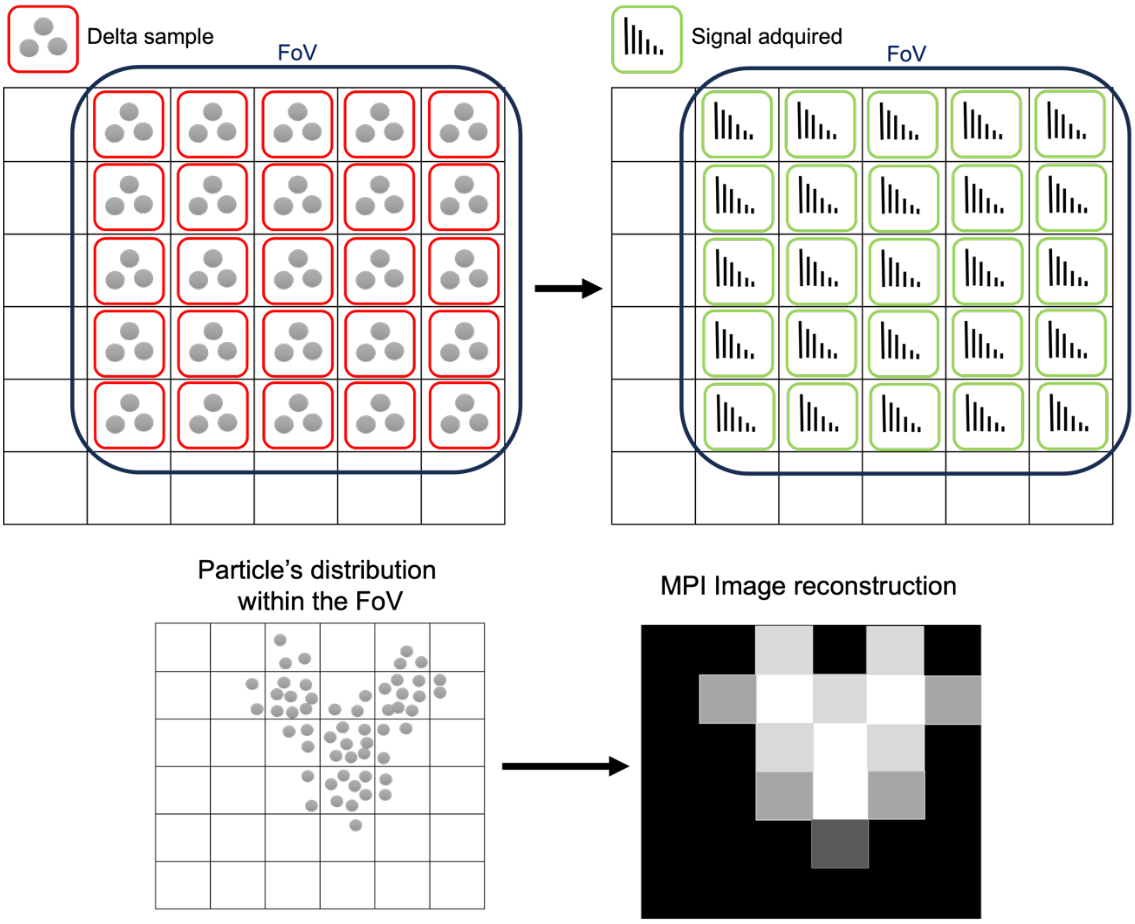

Figure 6. **System matrix procedure and image reconstruction**. Top Left; Delta sample is moved to each voxel through the FoV. Top Right: the spectrums acquired at each position. Lower part: Particles' distribution within the FoV and the MPI image reconstruction displayed as grey-scale.

The concentration of the particles during calibration should be higher than usual to gain a good Signal Noise to Ratio (SNR) (e.g., Resovist 0.15 M (Löwa, Radon, Kosch, & Wiekhorst, 2016)). SNR is a parameter that measures the level of a desired signal compared to the level of background noise. In summary, the SM information provides information on the particles' signal and its position in space, and the quality of the SM will correlate with the quality of the image reconstruction. Given a suitable calibration measurement, it is enough to read the amplitude of one selected harmonic from the signal response; its amplitude value will be proportional to the amount of superparamagnetic iron measured during the calibration measurements. Furthermore, SM highly depends on the particles' type and viscosity. As a result, it is specific for each tracer and their respective environment; any hardware modification needs a new SM process.

1.2.6. Sensitivity, spatial and temporal resolution

One of the most important parameters of an imaging method is the resolution, which basically describes how close two objects can be to each other such they can be clearly distinguished in the imaged picture. The distance from one maximum to the other maximum is defined as spatial resolution. Sensitivity is also an essential parameter of an imaging method. In this case, sensitivity determines the minimal amount of magnetic material that can be detected using MPI. Sensitivity and spatial resolution are linked to each other, this means that if the gradient strength increases, it improves the spatial resolution because the area with zero magnetic field, the FFP, becomes smaller, and the particle signal comes from a more accurate location. However, this assumption uniquely takes place when the particles have sufficiently high SNR. The particle core diameter has the greatest influence on the resolution, and the distribution of the particle core diameter within a sample limits the prediction of the resolution, because mono-size particles are not commercially available (Rahmer, Weizenecker, Gleich, & Borgert, 2009). Sensitivity can be also increased by averaging multiple measurements, however temporal resolution, the amount of time needed to revisit the data, would decrease.

1.3. Medical applications of MPI

To date, MPI has become a valuable tool in many clinically relevant applications such as diagnosis, therapy, and medical interventions:

- **Angiography.** MPI angiogram can overcome limitations such as the low temporal resolution in magnetic resonance angiography and the radiation for CT angiography. Furthermore, MPI provides functional parameters about the tissue perfusion to assess myocardial viability, for example. Molwitz et al., (2019) presented the first angiographic MPI imaging for human size.
- **Hyperthermia.** Due to their rapid magnetization, heat is generated at the site where the nanoparticles are administered systematically or locally (Tay et al., 2018). This hyperthermic effect can target tissue damage in the area surrounding the nanoparticles; unlike healthy tissue, which may confront temperatures of 42-45 ºC, cancerous cells will undergo apoptosis (Giustini et al., 2010).
- **Cell tracking.** MPI has been employed as a cell tracking technology because of its high sensitivity and the direct quantification of SPION content in labelled cells at any depth. SPIONs have great potential for in-vivo cell tracking performance due to their biocompatibility. Zheng et al., (2015) reported the highest sensitivity cell detection achieved among all imaging technologies. They could detect down to 200 labelled cells using an FFL projection MPI scanner.
- **Cancer and tumor detection.** During cancer development, the vasculature neoangiogenesis is predominantly leaky and chaotic, resulting in an Enhanced Permeability and Retention (EPR) effect. MPI nanoparticles have shown a good EPR effect on the location of cancer and tumor vessels in mice experiments (Arami et al., 2017).
- **Perfusion imaging.** The 3D real-time image of the brain's reperfusion after acute ischemic stroke with MPI eludes the high doses of radiation that CT-perfusion scans require (Ludewig et al., 2017).
- **Device visualization and manipulation.** Different types of magnetic nanoparticles can be injected into the bloodstream. Therefore, their relaxation can differentiate multi-color MPI between free and cell-bound

tracers (Szwargulski et al., 2020). Additionally, catheters can be coated with nanoparticles to track their position and perform the clinical intervention (Rahmer, Wirtz, Bontus, Borgert, & Gleich, 2017).

- **Magnetic Navigation:** MPI offers the possibility of combining therapeutic and diagnostic approaches for most interventions**.** The nanoparticles can be functionalized with chemotherapeutic molecules like doxorubicin (DOX) and more complex therapeutic compounds like siRNAs (Shrestha, Wang, Brey, Uribe, & Tang, 2021). Further, Magnetic Particle Imaging Navigation (MPIN) has already been successfully applied to navigate particles contactless, displaying enormous potential for targeted drug delivery (Griese et al., 2020).

This work is a crucial step toward clinical MPI stroke therapy. The location and measurement of the infarct core and the corresponding ischemic penumbra represent the target for any treatment approach. The preliminary work from our group already proved that MPI can quickly detect intracranial hemorrhage and ischemic stroke in a mouse model, which is an essential requirement for the clinical translation of MPI for point-of-care monitoring of different stroke subtypes (Ludewig et al., 2017). Our work is justified for the demonstration that MPI and magnetic particle navigation of thrombolytic functionalized particles can track the correct targeting and quickly re-establish the blood flow of the occluded vessel with a non-invasive procedure, for a rapid recoverable penumbra tissue and better clinical outcome in stroke patients.

1.3.1. Potential of MPI for acute ischemic stroke

The physiological mechanism of ischemic stroke is the occlusion of a cerebral artery (Fig.7.1), which reduces blood supply to the corresponding brain regions. We can name two stroke areas under this physiological event. The infarct core (Fig.7.2) is considered irreversibly damaged tissue, while the penumbra (Fig.7.3) is the hypoperfused brain region with an increased risk of necrosis but is still recoverable. The difference between the infarct core and the penumbra volume is commonly postulated as the tissue at risk. The infarct core necrosis can extend into the penumbra increasing the ratio of non-rescuable tissue. This observation conducts to a faster re-irrigation of the occluded artery will follow more preserved tissue and beneficial clinical outcomes (Tanaka et al., 2020). It has been shown that treatment decision-making time in acute ischemic stroke patients is essentially based on more accurate and precise imaging information to identify ischemic stroke for personalized and subsequently higher patient benefits from stroke treatment (Grøan et al., 2021). Therefore, quick stroke diagnosis based on imaging information for a hurry penumbra reperfusion intervention represents the target for any stroke treatment (e.g., thrombectomy and thrombolysis).

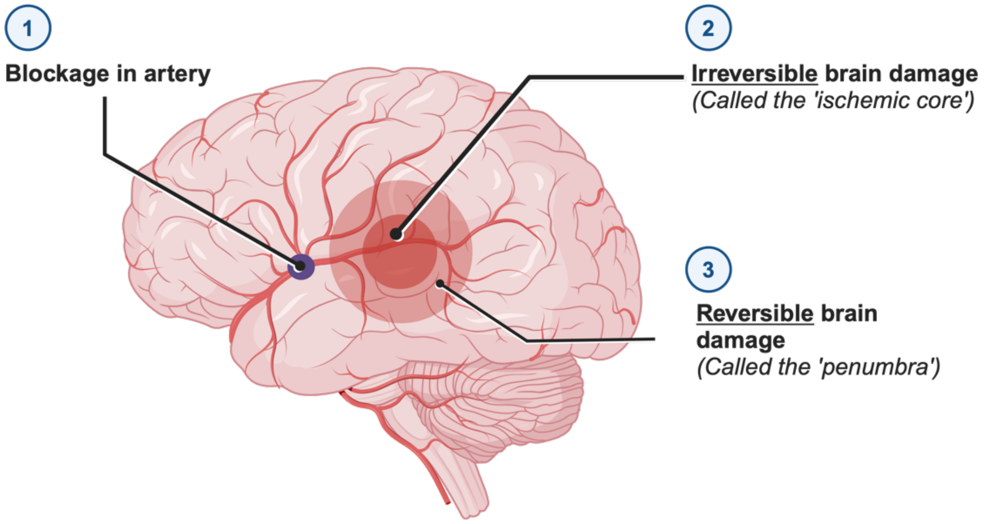

Figure 7. **Brief summary of the development of ischemic stroke**. 1. An ischemic stroke occurs when a blood clot blocks the flow in an artery within the brain—a peripheral region of stunned cells. 2. Ischemic core; Central irreversibly infarcted tissue core. Neurons in the ischemic core are considered beyond rescue. 3. Neurons in the ischemic penumbra are potential targets for therapeutic interventions. Image created with Biorender.

The most considerable progress in the last years was the fast and accurate assessment of cerebral perfusion. Defining the viable tissue through perfusion imaging is necessary to select optimal candidates for this therapy. Nowadays, multiparametric CT and MRI perfusion imaging are the principal modalities to determine the infarct core volume and the penumbra size. However, they have shown low accuracy and poor reliability in quantifying the infarct core and penumbra segmentations due to their low temporal resolution (1 s <), which has been criticized for excluding patients of optimal stroke treatment (De Oliveira, Fiebach, Vagal, Schaefer, & Aviv, 2021).

Theoretically, the excellent signal-to-noise ratio and the spatial and temporal resolution of the MPI scanner, which exceeds current CT and MRI, could significantly improve the quantification of the perfusion parameter map required for clinical decision-making. Some preclinical experiments have proved the high temporal and spatial resolution of up to 46 frames per second, allowing 3D real-time imaging with high sensitivity, free-radiation, and no toxic tracer material needed for magnetic particle vascular imaging (Molwitz et al., 2019; Szwargulski et al., 2020; Zhou et al., 2018). The preclinical MPI scanner could detect exceedingly small infarct volumes in a middle cerebral artery occlusion mouse model; in translating to humans, the expected spatial resolution is in the same range as in typical supratentorial infarct in patients (Szwargulski et al., 2020).

In this work, Magnetic Particle Imaging is combined with Magnetic Particle Navigation (MPIN) to contribute to the study of the potential of MPI for treating ischemic stroke.

1.3.2. Magnetic force on Magnetic Nanoparticles

Magnetic Particle Imaging (MPI) was initially developed as a diagnostic imaging technique, but it has evolved to enable real-time tracking and magnetic manipulation of nanoparticles, particularly in therapeutic applications such as mechanical thrombectomy for acute ischemic stroke. Recent advancements have demonstrated the feasibility of Magnetic Particle Navigation (MPN), which enables the controlled steering of nanoparticles through complex vascular structures using magnetic fields (Griese et al., 2020).

The ability to apply magnetic forces on nanoparticles has significant implications for stroke therapy. Thrombolytic agents attached to magnetic nanoparticles can be directed to the site of the blood clot, overcoming the challenges associated with poor drug penetration in bifurcated or occluded vessels (Fig.8 left). By using MPI to guide these particles, the therapy becomes more localized, increasing the treatment’s efficacy and minimizing potential side effects such as systemic bleeding (Fig.8 right) (Yang et al., 2012). Furthermore, this targeted approach can reduce the overall dosage of thrombolytic drugs, further mitigating risks associated with conventional treatments.

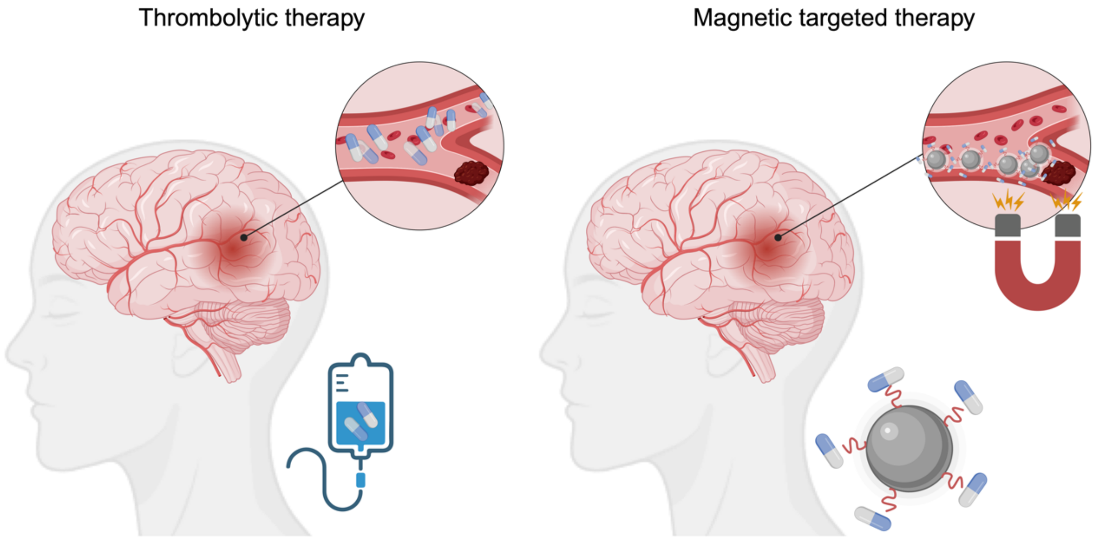

Figure 8. Schematic picture of magnetic targeted therapy in ischemic stroke in a bifurcation blood vessel. Standard thrombolytic therapy (left) describes the situation where the injected medicament flows through the free vessel and does not reach the clot when it is localized in a bifurcation blood vessel. Magnetic targeted therapy (right) in MPI can navigate particles with the effective drug in a contactless fashion onto the blood clot, where it has a local effect and high effectiveness. Image created with Biorender.

Additionally, MPI-based navigation systems have shown the capacity to control the movement of magnetic particles in real-time. This technology is particularly promising for overcoming the blood-brain barrier, offering a non-invasive method for delivering therapeutic agents directly to the brain (X. Zhang, Le, & Yoon, 2017). As a result, MPI holds great potential for transforming the treatment of ischemic stroke, enabling faster and more precise interventions that improve patient outcomes.

The treatment to break up blood clots and prevent new clots from forming is generally named thrombolysis therapy.

1.3.3. The physiology of thrombolysis

There is a natural regulation of coagulation or clot formation and fibrinolysis or dissolution of clots. These interconnected processes are controlled by two major components: plasma proteins such as plasminogen activators or thrombin (fibrinolytics), factor X and fibrin (procoagulants), and cellular blood cells like platelets (procoagulant). Fibrin is the rigid structure surrounding the clot, which blocks flow to a portion of the brain in the case of an ischemic stroke. The term thrombolysis usually relates to the degradation of fibrin; ergo, it is a synonym of fibrinolytic. From a clinical standpoint, the use of thrombolytic drugs as a treatment for ischemic stroke has the purpose of recanalization of the occluded artery and reperfusion of salvageable brain tissue, the so-called ischemic penumbra, and the outcome damage can be mitigated. Consequently, any drug that induces clot breakdown (fibrinolysis) will be referred to as a thrombolytic.

1.3.4. Thrombolytics for ischemic stroke treatment

Some trials continued to investigate first-generation thrombolytics for ischemic stroke treatment. However, these older medications, such as streptokinase and urokinase, were not high fibrin specific and could lead to bleeding risks. Hence, a combination of thrombolytic and anti-platelet therapy was a choice. However, they led to an increased risk of bleeding (Kamarova et al., 2022).

Currently, there are four options available for thrombolytic therapy. First, the classical treatment is based on the administration of anticoagulants and antiplatelet drugs. The former includes some commercial anticoagulants that block steps in the fibrin cascade. Some available products are Warfarin (Coumadin®, Bristol-Myers Squibb PharmaCompany), which prevents the synthesis of vitamin K-dependent coagulation factor, or Heparin, which blocks the factor X activation and thrombin formation in the coagulation cascade. Following classical therapy, antiplatelet drugs are more likely to prevent the thrombosis from happening or getting more significant. One example is Aspirin, which inhibits platelet aggregation. On the other hand, Clopidogrel and Ticlopidine are used to inhibit platelet activation. An invasive treatment would be the surgical intervention to remove the thrombus when the drug treatment has failed or it is contra-indicated. However, critical aspects compromised the development of thrombolytics for ischemic stroke; most patients do not receive thrombolytic therapy because the time window of opportunity for treatment is still narrow (Alexandrov & Grotta, 2002). Any improved aiming wider time window could be practical and crucial for future stroke patients. Recombinant thrombolytic therapy has become a transformation of advanced medicine, ensuring treatable acute emergencies in vascular occlusions.

1.3.5. The evolution of recombinant thrombolytics

The development of the recombinant tissue-Plasminogen Activator (rt-PA) with the molecular biology revolution came with important improved factors. First, recombinant t-PA was human type and did not cause any immunology reactions; consequently, repeat dosing was feasible. Second, intracranial hemorrhage risk was low and it demonstrated efficacy and safety. Finally, the identified pre-clinical time window of 90 minutes resulted in rt-Pa as the first approved therapy for ischemic stroke (Brott et al., 1992; Haley et al., 1992).

Fibrinolytic enzymes are mainly serine proteases acting directly or indirectly for fibrin lysis in thrombus (Kotb, 2014). This group is composed by plasminogen activators such as Streptokinase (SK), Staphylokinase (SAK), Urokinase (u-PA), and tissue-Plasminogen Activator (t-PA) among others. The direct plasminogen activators are all serine proteases that cleave a single arginine-valine aminoacid bond to yield plasmin. On the other hand, indirect activators do not have enzymatic activity, and they form a complex with plasminogen to get plasmin. Plasmin is the proteolytic enzyme that breaks the cross-links between fibrin molecules that supply structural integrity to the thrombus. Then, the dissolution of the clot can proceed (Flemmig & Melzig, 2012).

Concerning the efficacy of the thrombolytic drugs, the age of the clot must be considered. Older clots come with more fibrin crosslinking and are more resistant to thrombolytic. Therefore, the age of the coagulum can reduce the efficacy of thrombolytic drugs, and the fibrinolytic's specificity and half-life will determine its effectiveness (Loren, García Frade, Torrado, & Navarro, 1989). The noticeably short half-life of plasmin as a thrombolytic drug has been tested and suited as a local therapy at the site of the thrombus, occasioned by its rapid neutralization by α2-anti-plasmin (Collen, 1980). Streptokinase is an indirect activator of plasmin, and it was used as a treatment for acute myocardial infarction in the late 50s for the first time, becoming the first generation of thrombolytics (Fletcher, Alkjaersig, Smyrniotis, & Sherry, 1958). Streptokinase is produced from streptococcal bacteria and frequently induces immunologic reactions and hypotension (Khalid, Ahmad, Tong, Lui, & Abidin, 2021). The second and third generations of thrombolytics came during the 1980s due to the development of recombinant technology. Alteplase, or recombinant tissue-Plasminogen Activator (rt-PA), is the most well-studied second-generation thrombolytic due to its 400-fold enhanced fibrinolytic activity and high specificity for fibrin (Collen & Lijnen, 1995). The development of the third generation aimed to increase the half-life and fibrin specificity with slight changes in their chemical structure. Tenecteplase and Reteplase are the most well-known agents because of their longer half-life and their advantage in bolus dosing (Verstraete, 2000). Another third-generation thrombolytic is Amediplase (K2tu-PA), a hybrid plasminogen activator composed of the kringle-2 domain of t-PA and the catalytic protease domain of the single-chain urokinase-Plasminogen Activator. Amediplase has a molar mass of 39.9 kDa and a longer plasma half-life, over 30 min, supported by a single bolus dose. Although it shows a lower binding affinity to fibrin than rt-PA, Amediplase shows better clot penetration (Rijken, Barrett-Bergshoeff, Jie, Criscuoli, & Sakharov, 2004). It is currently in phase III clinical trials in Europe as a single bolus thrombolytic agent in patients with myocardial infarction.

Engineering the particles' surface allows a new dimension of functionalities and expands their potential for targeted drug transport with MPI. With SPION as nanoparticles, one could conjugate various agents targeted to a specific component of the thrombus. With the addition of the imaging feature of MPI, we can determine the localization of the conjugated particles to the target thrombus and the imaging of the reperfusion after the treatment.

1.4. Surface functionalization of magnetic nanoparticles

Magnetic nanoparticles have been formerly investigated for targeted drug delivery and imaging applications in other pathologies, particularly for cancer and vaccine delivery (Al-Deen, Selomulya, Ma, & Coppel, 2014; Arami et al., 2017). However, the potential of magnetic targeted drug delivery for cerebrovascular conditions has not been extensively studied (W. Chen et al., 2021). The formulation of magnetic nanoparticles carrying thrombolytic agents can be improved with the external mechanical stimuli of an external magnetic field to target and loosen the clot. Surface functionalization of MNP has optimized their imaging properties and improved their biocompatibility.

Developing tailored particles by modifying the surface chemistry has enabled efficient targeted drug transport (Comanescu, 2022). The first objective of surface modification is that the functional groups added should increase colloidal stability and prevent aggregation of the particles. One example is steric hindrance surface coatings like polyethylene glycol (PEGylation) chains that prevent particles from aggregating. Polyethylene glycol (PEG) chains repel each other and ensure colloidal stability within a biological environment (Suk, Xu, Kim, Hanes, & Ensign, 2016). Lately, surface functionalization allows the introduction of essential functional groups for the conjugation of therapeutic agents, their controlled release, and enhanced pharmacokinetics.

The functionalization of MNP is divided into *in situ* and *post*-synthesis. *In situ* functionalization means the particles and their surface modification are synthesized stepwise (Roy & Pericàs, 2009). This method reduces the particle size distribution because the coating process prevents further growth of the particles. On the other hand, in the *post*-synthesis method, the particles are first synthesized and then functionalized using different materials in a second step (Čampelj, Makovec, & Drofenik, 2009). Available materials for the surface functionalization of MNP are classified into organic and inorganic compounds. Organic molecules, such as amino, aldehydes, carboxyl, and hydroxyl groups, usually enhance the particles’ stability and prevent their accumulation. These organic composites retain the particles' magnetic properties but also hold good biocompatibility and biodegradability. The presence of organic groups over the surface of MNP provides the link for the conjugation of bio-substances such as DNA, antibodies, proteins, or enzymes (Abedi et al., 2019; Niu, Wang, Zhu, Zhao, & Ma, 2014). On the other hand, inorganic materials such as silica, metals and metal oxides, exhibit antioxidant properties and chemical stability to the particles in solution, and enable the binding of biological molecules or drugs onto the surface (Lyon, Fleming, Stone, Schiffer, & Williams, 2004; Sheng et al., 2016).

Multiple chemical approaches have been used for the conjugation of MNP surfaces. The chemical properties of the ligand to be coupled and the functional groups on the particles' surface prescribe the conjugation strategy. The reactions have been categorized into direct nanoparticle conjugation, linker chemistry, and physical interactions (Hermanson, 2013). In the process of direct reaction strategy, the functional groups found on the nanoparticle surface, such as amino, sulfhydryl, aldehyde, or active hydrogen, are directly bonded to the reactive ligand. Direct bioconjugation is particularly suitable for small molecules, however, it can be challenging because the ligand can lose bioactivity (Weissleder, Kelly, Sun, Shtatland, & Josephson, 2005). Linker chemistry is a novel modification of direct conjugation that was developed to prevent the potential to lose the activity of the ligand. This technique increases the stability of linkages for targeting moieties due to the control over the molecular orientation of bound ligands (Hein, Liu, & Wang, 2008). The most common approaches are the conjugation of SPIONs decorated with amine moieties that bind the sulfhydryl groups of a biomolecule (Derksen & Scherphof, 1985), or the reaction of carboxylic acid groups of the SPION surface with the primary amines from the biomolecules through 1-ethyl-3-(-3-dimethylamino propyl) (ED) Carbodiimide linkers (Kohler, Fryxell, & Zhang, 2004). Finally, physical interactions are classified into electrostatic, hydrophilic/hydrophobic, and affinity interactions. The main advantages of this assembly are the fast and high-efficiency binding capacity and the lack of intermediate modification steps. Electrostatic interaction can be favorable for functionalizing plasmid DNA onto SPIONs (Steitz et al., 2007). Hydrophobic/hydrophilic interactions have been proven efficient for adsorbing hydrophilic/hydrophobic drugs onto SPIONs. However, they are susceptible to changes in environmental conditions such as pH or salinity (Jurgons et al., 2006). Affinity interactions are suited for effective bioconjugation of targeting ligands to SPIONs. SPIONs' surface can be modified with streptavidin or biotin, which explicitly binds biotin or streptavidin respectively. Streptavidin-biotin linkage is one of nature's most robust and stable non-covalent interactions (Levenberg et al., 2023). Figure 9 represents a sketch of SPION functionalization possibilities.

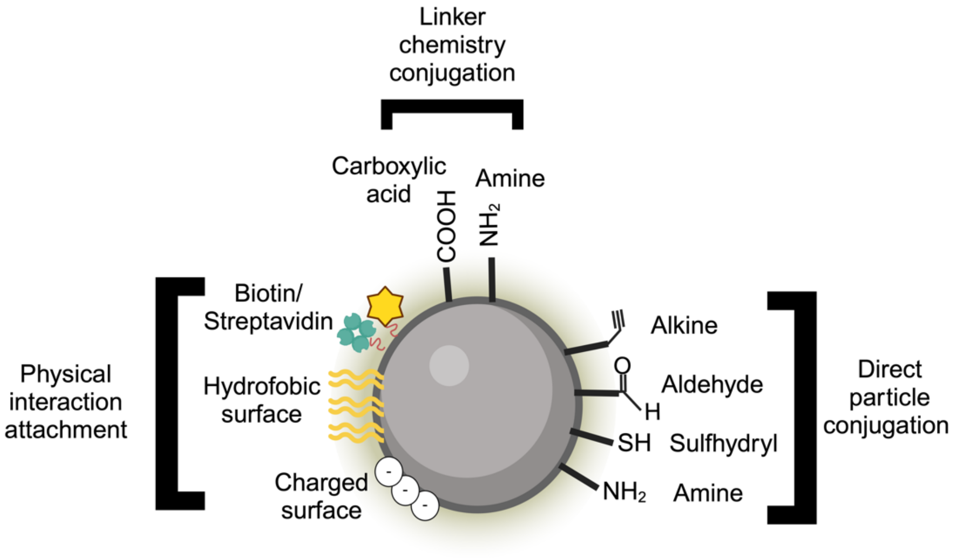

Figure 9. **Available materials for SPIONs functionalization.** They are divided into physical interactions, linker chemistry, and direct particle conjugation, and the conjugation reaction approach is prescribed.

Considering the crucial role of optimizing SPIONs' characteristics for MPI performance and its applications, in this work we also investigate the development of tailored tracers for MPI.

1.5. Developing optimized tracers for MPI

As mentioned in *section 1.2.*, the tracer employed influences the basic principles, the effectiveness of the signal detection, and the imaging quality of MPI. SPIONs are particularly advantageous tracers; they have been approved by the USA Food and Drug Administration (FDA) for clinical use, they are non-radioactive and their signal is stable over time. They are also widely accessible, easy to manage, and cost-effective compared to other commonly used tracers (Wu et al., 2019). Most tracer developments for MPI have traditionally been based on chemically synthesized iron oxide compounds. Recent studies indicate the potential of enhancing the magnetic properties of SPIONs through the synthesis of non-spherical particles, theoretically offering a promising method to improve MPI sensitivity and spatial resolution (Wang et al., 2020; Ziemian et al., 2018).

1.5.1. Magnetosomes

A promising alternative might be biogenic magnetic nanoparticles, so-called magnetosomes, synthesized by magnetotactic bacteria (MTB) (see Fig.10). In the model organism *Magnetospirillum gryphiswaldense*, magnetosomes are membrane-enclosed iron oxide nanoparticles with exceptional magnetic properties that cannot be replicated in the laboratory by chemical synthesis. Magnetosomes consist of a cuboctahedral core of pure magnetite with high crystallinity and high uniformity in size and shape, surrounded by a biological membrane of phospholipids and magnetosome-specific proteins fulfilling essential functions in magnetite biomineralization (Kolinko et al., 2014; Uebe & Schüler, 2016). Magnetosomes are usually organized within chains inside the bacteria that prevent aggregation. They possess high values of coercivity and thermal stable magnetic moment due to their large single magnetic domain. These are ideal requirements for an improved performance in MPI, unlike many chemically synthesized superparamagnetic particles with thermally unstable magnetic moment (E. Alphandéry et al., 2008).

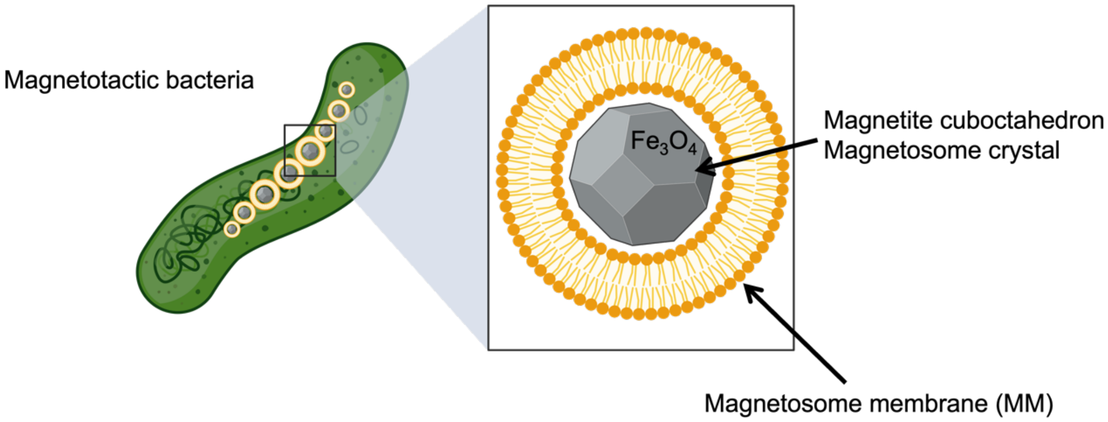

Figure 10. Schematic representation of normal *magnetospirillum* cell with magnetosome chain and zoom-in of the magnetosome structure. Image created with Biorender.

Four steps compromise magnetosome biogenesis; First, the magnetosome membrane is formed from the invagination of the cytoplasmic membrane. Second, magnetosome proteins are sorted into the magnetosome membrane. Third, iron is transported into the magnetosome membrane and mineralized as magnetite crystals. Fourth, the magnetosome chain is assembled. All these four steps from the magnetosome biosynthesis are governed by the magnetotactic bacteria's highly conserved set of >30 genes, organized in five operons, that compromise many genetic determinants. As the strain is accessible to genetic engineering, size-adjusted magnetite crystals can be generated using synthetic biology (Kolinko et al., 2014; Lohße et al., 2011). Thus, deleting single magnetosome genes or whole operons resulted in strains with reduced particle diameters and, consequently, different magnetic properties (Taukulis et al., 2015). Some genes like *mamJ* and *mamR* (*mam*; magnetosome-associated membrane) are essential because they are involved in critical steps of magnetosome biogenesis. By contrast, other genes encode non-essential proteins. They have accessory roles in regulating the biomineralization of crystals after nucleation of the growing magnetite crystal. However, they positively regulate size and shape, like *mamF* and *mmsF* proteins (*mms*; magnetosome membrane specific), and the iron accumulation that includes iron transporters such as *feo*AB and Fe4 (Uebe & Schüler, 2016).

Since the late 1980s magnetosomes have been suggested as promising agents for magnetic imaging techniques (Kirschvink, 1989; Moskowitz, Frankel, Flanders, Blakemore, & Schwartz, 1988; Tsien, 2003) because of their material properties and structural features, such as a high crystallinity and a narrow particle size distribution (Gaussian to logarithmic-normal size distribution (Hergt et al., 2005; Kraupner et al., 2017)); that can only hardly be achieved by chemical synthesis.

Our study first investigated different genetically engineered magnetosome types (supplementary table 1) with increasing core diameter regarding their signal responses in MPS. The most promising candidate was finally chosen for in-depth analysis of its signal response, phantom experiments, and potential future *in vivo* studies in an animal model.

2. Materials and methods

2.1. Materials

Chemicals	Manufacturer
Aqua ad iniectabilia	Braun
Blasticidin	Invivogen
B-mercahtoethanol	Gibco TM
Bovine Serum Albumin (BSA)	Sigma Aldrich/Merck
Carbenicillin	Sigma Aldrich/Merck
Coomassie Brilliant Blue staining	Bio-Rad
Dimethyl sulfoxide (DMSO)	Sigma Aldrich/Merck
DMEM Medium	Gibco TM/ Thermo Fisher Scientific
DNA Gel Loading Dye, 6x	Nex England Biolabs
Fetal Calf Serum (FCS)	Gibco TM/ Thermo Fisher Scientific
Glyceol	Sigma Aldrich/Merck
HEPES 1M	Gibco TM/ Thermo Fisher Scientific
HIS-Select Nickel Affinity agarose	Sigma Aldrich/Merck
LB Agar	BD Difco
LB Broth	BD Difco
L-Glutamine, 200 mM	Gibco TM/ Thermo Fisher Scientific
NuPage TM LDS sample Buffer, 4x	Invitrogen/Thermo Fisher Scientific
NuPage TM Sample Reducing Agent, 10x	Invitrogen/Thermo Fisher Scientific
Paraformaldehyde (PFA)	Sigma Aldrich/Merck
Penicillin/Streptomycin	Gibco TM/ Thermo Fisher Scientific
Phosphate Buffered Saline (PBS)	Gibco TM/ Thermo Fisher Scientific
Polyethylenimine (PEI), MW 25000	Polysciences, Inc.
Roti®Block	Carl Roth
SOC-medium	Sigma Aldrich/Merck
Sodium chloride, 0,9%	Braun
Trypan blue 0.4%	Gibco TM/ Thermo Fisher Scientific
Trypsin 1x	Sigma Aldrich/Merck
Tween-20	Sigma Aldrich/Merck

Consumables	Model/Type	Company
Amicon® Ultra-15 Centrifugal Filters	Ultracel® Regenerated Cellulose 30kDa	Millipore
Cell Culture well-Plates	Various Sizes	Thermo Fisher Scientific
Cell culture flask	T-25, T75	Greiner bio one/ Nunc TM
Cell culture flask	T75-T175	Sarstedt

Cryogenic vials	Nunc Cryotube	Greiner bio one/ Nunc TM
Erlenmeyer Flask	500 ml	PP Corning Inc
Falcon Tubes	15 ml, 50 ml	Greiner
Gloves	Nitratex	Ansell
Microcentrifuge tubes	Various sizes	Eppendorf
Nitrocelullose membrane	Odyssey Nitrocelullose membrane	LI-COR®
Nunc 96 well plates	MaxiSorp	Thermo Fisher Scientific
Pippete tips	Various Sizes	Eppendorf
Petri dishes	Various Sizes	Thermo Fisher Scientific
SDS-Page gels	Bis-Tris 10%, 4-12%	Invitrogen
Serological pippetes	Various Sizes	BD Falcon
Sterile filtration	Seteriflip, Stericup	Millipore
Syringes and needles	Various Sizes	Braun/ BD Biosciences

Eucaryotic Cell culture media	**Composition**
Complete DMEM	DMEM medium 2 mM L-Glutamine 1 mM Sodium Pyruvate 10 mM Hepes 5% FCS
Feeding Medium	20% tryptone in FreeStyle 293 experession Media
FreeStyleTM 293 Expression medium	Thermo Fisher Scientific

Bacteria culture media	**Composition**
LB-Agar	10 g/L Tryptone 5 g/L yeast extract 10 g/L NaCl 15 g/L Agar-agar (pH 7)
LB-Medium	10 g/L Tryptone 5 g/L yeast extract 10 g/L NaCl (pH 7)

SOC-Medium	8.6 mM NaCl 2.5 mM KCl 20 mM MgSO4 20 mM Glucose 2% Tryptone 0.5% yeast extract

DNA standars	**Manufacturer**
GeneRule, 1 kB	Thermo Fisher Scientific

Proptein Standars	**Manufacturer**
PageRuler	Thermo Fisher Scientific

Resitriction enzymes	**Manufacturer**
BamHI	New England Biolabs
EcoRI	New England Biolabs
Nco I	New England Biolabs
NheI	New England Biolabs
Not I	New England Biolabs
Xba I	New England Biolabs

Plasmid	**Specifications**
pCSE2.5_His	Variant of pCSE2.5 vector with a hexahistidine tag flanked by NotI and XbaI restriction sites

Antibody	**Manufacturer**
HRP conjugated Anti 6x His tag® polyclonal	Abcam ab1187
HRP conjugated Streptavidin	Abcam ab7403

KIT	**Manufacturer**
BCA TM Protein Assay kit	Pierce
Bir-A500	Avidity LLC ©
Ni-NTA Buffer kit	Merck-Millipore
Nucleo Spin ® Gel and PCR Clean up	Macherey Nagel
Plasmid Maxi Kit	Qiagen
Plasmid Mini Kit	Qiagen
pNAPEP-1588	Cryopep
Super Signal West Pico Plus	Thermo Fisher Scientific
Prokaryotic Cells	
NEB 5-alpha F'*Iq* Competent *E. coli*	New England Biolabs

Eukaryotic cell lines	
HEK293T, untransfected	Received from Prof. Dr. med. Nolte laboratory group.
HEK293 6E, untrasfected	

Buffer	**Composition**
Agarose gel electrophoresis	
Sample buffer 6x	2.5% Ficoll-400 11mM EDTA 3.3mM Tris-HCl 0.017 % SDS
Tris Acetate EDTA buffer (TAE) 50x	2 M Tris-Acetate 50 mM EDTA
Cell Transfection	
NaCl 300 mM	300 mM NaCl in deionizaed water
PEI (Polyethylenimine)	7.5 mM 25 kDa Linear Polyethylenimine 0.333 mg/ml in deionized water
SDS-PAGE	
MES TM Running Buffer	50 mM MES 50 mM Tris Base 1% SDS 1 mM EDTA (pH 7.3)
Nu PAGE TM LDS Sample Buffer 4x	Lithium dodecyl sulfate (pH 8.4)
Nu PAGE TM Sample Reducing Agent 10x	500mM dithiothreitol (DTT)
Transfer buffer	25 mM tris Base 192 mM glycine 10% methanol pH 8.3
TBST 10x	200 mM Tris base 1.4 M NaCl 1% tween 20 pH 7.4

2.2. Methods

2.2.1. Molecular Biology Methods

Polymerase Chain reaction **(PCR)**

Polymerase chain reaction technique amplifies a specific segment of DNA by thermal cycling. A double-stranded DNA-Template is denatured to single strands at temperatures between 90ºC to 95ºC. For the annealing step, to allow oligonucleotides to anneal to the complementary strands of the targeted DNA sequence, the temperature is decreased to 65ºC – 50ºC and the amplified segment is flanked. During the elongation step, the polymerase incorporates deoxyribonucleotide triphosphates (dNTPs) to the 5' end of the flanked DNA and builds a copy in the 3' direction at a temperature between 69ºC to 72ºC. The annealing and elongation steps are repeated in many cycles, throughout which newly synthesized DNA fragments become a template for further amplification. PCR reactions were used for amplification of DNA fragments. The following reactions were used in this project.

Table 2. PCR reaction with Dream Tag Polymerase.

Reagent	Volumen (µl)	Final concentration
10x TAP buffer (with Mg SO_4)	2.5	1x
dNTPs (2 mM)	2.5	0.2 mM
Forward primer (10 µM)	1	400 nM
Reverse primer (10 µM)	1	400 nM
Dream Tag Polymerase	0.5	0.02 U/µl
DNA (app. 1 ng)	-	
ddH2O	Up to 25 µl	

Table 3. Standard PCR amplification.

Reaction steps	Temperature (ºC)	Time (s)	Cycle
First denaturation	95	180	1
Denaturation	95	15	35
Annealing	60	15	
Elongation	72	15	
On hold	4	-	

Agarose gel electrophoresis of DNA fragments

DNA fragments were separated according to their size by agarose gel electrophoresis. Agarose matrices of 1.5% were prepared in 100 mL Tris Acetate EDTA (TAE) buffer with 10 µl of Roti®-Gel Staing (Carl Roth GmbH + Co KG). Samples were dyed with loading buffer (LDS 6x Thermo Fisher Scientific) for visual tracking during migration and DNA ladder (GeneRule 1kB from Thermo Fischer Scientific) was used for a comparative analysis of the size bands. The migration of the DNA fragments was performed at 120 V for 40 minutes. Using a UV-Transilluminator with Video-image system (BioVision 3000), DNA bands were visualized and photographed for documentation. For purification, a simple UV-Transilluminator (Type T1, Biometra) was used for visualization and excision of the bands.

DNA extraction from agarose gel

PCR products or restricted DNA fragments were excised from agarose gel and purified using the PCR clean-up and gel extraction kit from Macherey Nagel and following the manufacturer's protocol.

DNA enzymatic restriction

Enzymes cleave double-stranded DNA at determined palindromic sequences with the aim of cloning. DNA fragments were restricted using the appropriate enzymes and the corresponding buffers at the optimal temperature for restriction conditions and heat inactivation of enzymes according to the instructions of the manufacturer (New England Biolabs). The restriction reaction was performed in a total volume of 20 µl considering that 1U of endonuclease cleaves 1 µl of DNA. The temperatures for restriction and heat inactivation were set up in a thermocycler.

Transformation of chemically competent bacteria

Chemically competent bacteria E. coli XL-1 blue NEB 5-alpha F'Iq (New England Biolabs) were transformed with a plasmid DNA by heat shock. A 50 µl vial of bacteria stored at -80 ºC was thawed on ice. 5ng of plasmid DNA or ligation product was added to the E. coli XL-1 and incubated on ice for 30 min. Then, the bacteria together with the plasmid DNA were heat shocked by immersion in a

42ºC water bath for 30 seconds followed by 2 min incubation on ice. 450 µl of pre-warmed SOC medium was added and the transformed bacteria suspension was incubated at 37ºC with 200 rpm orbital shaking for 1h. Finally, cultures of transformed cells were seeded onto LB agar plates with the appropriate antibiotics under sterile conditions. Plates were incubated at 37ºC overnight and analyzed for the presence of clones.

Cultivation of bacteria culture for small- or large-scale plasmid DNA production

Bacteria cultures of either 5 ml (small production) or 100 ml (large production) of LB containing the corresponding antibiotic, were inoculated with a single clone picked up from the transformation plate. Cultures were then incubated overnight at 37ºC at 200 rpm orbital shaking. The next morning, cells were harvested by centrifugation at 4500 rpm at 4ºC for 10 min or 30 min for small and large production correspondingly. Supernatants were discarded and the plasmid DNA was extracted from the bacteria pellet using QIAprep® Spin Miniprep or Maxiprep Kits (Qiagen) following the manufacturer’s protocol.

Quantification of DNA

The concentration of double-stranded DNA was estimated by measuring the absorbance of DNA at 260 nm, where DNA displays the peak of light absorption, using the spectrophotometer Nanodrop 2000c from Peqlab Biotechnology. The DNA concentration was calculated using the conversion relationship A_{260} of 1=50 µg/ml of double-stranded DNA. Absorption at 280 nm was measured to estimate contaminations, and the ratio between A_{260} divided by A_{280} between 1.7 and 2.0 was considered as high-quality DNA purity.

Ligation of DNA fragments

Ligation technique was carried out for the generation of recombinant DNA plasmids. Ligation reactions were performed with the T4 DNA Ligase and the T4 DNA Ligase Reaction buffer from New England Biolabs, following the recommendations of the manufacturer. The molar ratio vector backbone to insert was 1:3 in a final volume of 20 µl. The reactions were incubated at room temperature overnight. The next morning, the T4 DNA ligase enzyme was heat-inactivated at 65 ºC for 10 min.

DNA sequencing

For sequencing DNA samples, 50-100 ng/µl of DNA in 17 µl sterile deionized water containing 10 µM sequencing primer were submitted to Eurofins (Ebersberg). The DNA sequences were analyzed with web BLAST for nucleotides (https://www.ncbi.nlm.nih.gov).

Gene synthesis

The desired nucleotide sequence was designed *in silico*, flanked by appropriate restriction sites for sub-cloning into the selected pCSE2.5 expression vector and optimized for expression in human eukaryotic cells using the online tool 'Gene Optimizer TM' by Thermo Fisher Scientific or by Twist Bioscience. These companies provide the designed gene fragments in a lyophilized form.

Cloning of Amediplase expression constructs

For the pCSE2.5 expression vector, the Amediplase gene fragment is flanked by NcoI and NotI restriction sites. In this pCSE2.5 expression vector, the NotI site is followed by the coding sequence for the 6 times histidine (His6x) tag, a stop codon and an XbaI site. The gene fragments and the expression vector were double digested with NcoI and NotI and subsequently connected via the linker in a three-step ligation.

2.2.2. Cell biology methods

Cell culture was performed under sterile conditions in a laminar flow bench (LaminAir HB2449 and HeraSafe 2030i). Media was purchased sterile and prepared solutions were sterilized either by filtration through a 0.22 µM filter using Stericup or Steriflip vacuum filter (Merck) or autoclaved at 121ºC for 20 min.

Cell culture of eukaryotic cells

HEK-293-6E cell line in suspension were cultivated in FreeStyle^{TM} 293 expression medium (Thermo Fisher Scientific) using T75 and T175 culture flasks with filter caps (Sarstedt AG and CO). Cells were cultured in a steam-saturated incubator at 37ºC with 5% CO_2. Sub-cultivation was performed by making a dilution of the cells according to the density, in a fresh media and in a new flask. Harvesting was carried out by centrifugation of the cell suspension at 4500 rpm for 10 min.

Determination of cell numbers using Neubauer Chamber

A 9 µl aliquot of the cell suspension and 1 µl of Trypan Blue 0.4% (Gibco) solution was mixed and added to a Neubauer counting chamber (Laboroptik). For this chamber, the concentration of the cell number per ml is calculated as follows: mean of the cell number per in major quadrants x 10^4 x dilution factor.

Cryopreservation of eukaryotic cells

For cryopreservation, approximately one million cells were resuspended in 1 ml fresh Freestyle 293 expression media and transferred into a cryogenic vial (Nunc Cryotube^{TM}). Cells were gradually frozen by short-term storage at 80ºC in a Mr.Frosty (Nalgene®), followed by long-term storage in liquid nitrogen.

Transient expression of Amediplase protease proteins in HEK293-6E cells

Recombinant proteins cloned into the expression vector pCSE2.5 were produced by transient transfection of HEK293-6E cells in suspension, cultured in FreeStyle 293 expression media (Thermo Fisher Scientific) using suspension cell culture flasks from Sarstedt. The cells were transfected with the DNA using the transfection reagent PEI (Polysciences Inc). For the transfection of cells in a culture volume of 30 ml in a T175 flask, 10 µg of plasmid DNA and 40 µg of PEI was prepared separately in 150 mM NaCl solution with a total volume of 500 µl each. Then, they were mixed and incubated at room temperature for 20 min. The mixture of DNA and PEI was added dropwise to the cells and the cells were cultured at 37ºC with 5% CO_2 in the incubator. The next day, cells were supplemented with 500 µl of feeding medium (20% w/v Tryptone in FreeStyle293 expression media). Five days later, supernatants with secreted proteins were harvested by centrifugation at 4000 rpm for 10 min, filtered by sterileflip-GP from Merck and then stored at 4ºC.

Magnetotactic bacteria strains and cultivation conditions

For the production of size-adjusted magnetosome samples, genetically modified *M. gryphiswaldense* strains Δ*mamR*, Δ*mamF*, Δ*mamF*/*mmsF* (each from (Lohße et al., 2014)), Δ*mamJ* (Scheffel et al., 2006), and Δ*feoAB1* (Heinke et al., 2017) were used. Additionally, we generated a *feoAB12* double mutant by deletion of the *feoAB2* genes within the Δ*feoAB1* strain using a previously published *galK*-based counterselection method (Raschdorf, Plitzko, Schüler, & Müller, 2014). Strains of *M. gryphiswaldense* (wildtype and mutants; see supplementary table 1) were grown in a modified flask standard medium (FSM; 10 mM 4-(2-hydroxyethyl)-1-piperazineethanesulfonic acid (HEPES), 15 mM potassium lactate, 4 mM $NaNO_3$, 0.74 mM KH_2PO_4, 0.6 mM $MgSO_4$, 50 µM Fe(III)-citrate, 3 g/l soy peptone, 0.1 g/l yeast extract, pH 7.0) as previously described (Heyen & Schüler, 2003). Cultivation was performed in 5 L flasks under moderate shaking (120 rpm) at 28°C, applying a headspace-to-liquid ratio of ~1:4 with air in the headspace. Under these conditions, the oxygen concentration in the medium declined with increasing cell density, thereby reaching microoxic conditions and inducing magnetosome biosynthesis (Lang & Schüler, 2008). Cells were harvested in the late exponential growth phase by centrifugation (9000 *g*, 20 min, 4 °C). Afterwards, cell pellets were resuspended in 20 mM HEPES, 5 mM ethylenediaminetetraacetate (EDTA), pH 7.2, and stored at -20 °C until further use.

Magnetosome strain productions were carried out by Dr. Frank Mickoleit at the Universtät Bayreuth.

Magnetosome isolation

For the isolation of intact magnetosomes, a two-step purification procedure was applied consisting of a magnetic separation and a sucrose high-density ultracentrifugation step (Raschdorf et al., 2018; Rosenfeldt et al., 2021). Cell pellets of microoxically grown *M. gryphiswaldense* cultures (wildtype or mutant strains) were resuspended in 20 mM HEPES, 5 mM EDTA (pH 7.2), and disrupted by 3-5 passages through a microfluidizer system (M-110 L, Microfluidics Corp., Westwood, MA, USA) equipped with an H10Z interaction chamber at 124 MPa. The crude extracts were passed through a MACS magnetic-separation column (5 ml; Miltenyi, Bergisch Gladbach, Germany) placed between two neodymium-iron-boron magnets (each 4.0 cm x 2.0 cm x 1.0 cm, 1.3 T). Thereby, non-magnetic cellular compounds passed the column and were instantly eluted whereas the magnetosomes were retained within the column. In order to remove impurities, the column was washed with 50 ml extraction buffer (10 mM HEPES, 1 mM EDTA, pH 7.2), followed by 50 ml high-salt buffer (10 mM HEPES, 1 mM EDTA, 150 mM NaCl, pH 7.2), and again 50 ml extraction buffer. Afterward, the magnets were removed, and the magnetosomes were eluted with double-distilled water (ddH_2O). The magnetosome suspension was then centrifuged through a 60% (w/v) sucrose cushion (in 10 mM HEPES, 1 mM EDTA, pH 7.2) for 2h at 200,000 *g* and 4°C. Because of their high density, the magnetosomes pelleted at the bottom of the tube, whereas residual cellular constituents were retained by the sucrose cushion. Finally, the particles were resuspended in double-distilled water (ddH_2O) and stored in Hungate tubes at 4°C under a nitrogen atmosphere until further use.

Prior to application *in vivo*, the magnetosome suspensions were sterile-filtrated as previously described (Mickoleit, Lanzloth, & Schüler, 2020). Briefly, the suspensions were diluted with ddH_2O to a final concentration of 50 µg Fe/ml, and sterile filtrated using a 0.22 µm PVDF sterile filter (Roth, Karlsruhe, Germany). After filtration, the suspensions were concentrated again to obtain final Fe concentrations of 2 mg/ml. TEM was performed on a JEM-1400Plus transmission electron microscope (JEOL, Tokyo, Japan) operated with an acceleration voltage of 80 kV. Magnetosome sizes were measured from TEM micrographs using the software ImageJ version 1.44p.

Magnetosome strain isolations were carried out by Dr. Frank Mickoleit at the Universtät Bayreuth.

Determination of iron concentrations

Suspensions of magnetosomes isolated from the wild type and mutant strains were normalized to their overall iron concentration. The iron content (mg Fe/ml) was determined by atomic absorption spectroscopy (AAS). Sample volumes of 5-20 µl were mixed with 69% nitric acid (final volume 1ml) and incubated for 3h at 98°C. Afterward, the samples were diluted with ddH_2O to receive a final volume of 3ml. Iron measurements were performed using a contrAA300 high-resolution atomic absorption spectrometer (Analytik Jena, Jena, Germany) equipped with a 300 W xenon short-arc lamp (XBO 301, GLE, Berlin, Germany) as continuum radiation source. The equipment presented a compact high-resolution double monochromator (consisting of a prism pre-monochromator and an echelle grating monochromator) and a charge-coupled device (CCD) array detector with a resolution of about 2 pm per pixel in the far ultraviolet range. An oxidizing air/acetylene flame was used to analyze the samples (wavelength 248.3 nm). The number of pixels of the array detector used for detection was 3 (central pixel 1). Measurements were performed in quintuplicates, each as a mean of three technical replicates (*n*=15).

Determination of the iron concentration of magnetosome strains was carried out by Dr. Frank Mickoleit at the Universtät Bayreuth.

2.2.3. Protein biochemistry methods

Protein production concentration recovery

The collected elution fractions were re-concentrated using Amicon Ultra Centrifugal filter columns (Millipore) with a 30 kDa molecular weight cut-off. The fractions with purified protein were pooled together and transferred to Amicon column. By multiple cycles of centrifugation at maximum speed, the elution buffer was also exchanged for PBS, and the protein was re-concentrated to a final volume of approximately 1 ml.

Quantification of protein

Protein solutions were quantified by means of the Bicinchoninic Acid Assay (BCA) kit (Pierce^{TM}, Thermo Fisher Scientific) following the recommendation of the manufacturer. The principle of BCA is based on the total protein concentration is exhibited by a color change of the sample solution from green to purple in a proportion to protein concentration, that can be measured using colorimetric equipment. The chemical formulation shows that amino acids in the protein sequence such as Cysteine, Tyrosine and Tryptophane reduce Cu^{2+} ions in an alkaline solution. These reduced cations (Cu^{1+}) react with the bicinchoninic acid to form a purple-colored complex that absorbs light at 562 nm. The concentration is determined using a standard curve generated from known amounts of Bovine Serum Albumin (BSA) (Pierce™, Thermo Fisher Scientific). The absorbance was measured using the photometer plate reader Victor 3, 1420 (Perkin Elmer).

Sodium Dodecyl Sulfate polyacrylamide gel electrophoresis (SDS-Page)

SDS-Page is a qualitative method to separate proteins by their molecular weight under the influence of an electric field. The anionic detergent Sodium Dodecyl Sulfate (SDS) is used to denature proteins and to confer a negative net charge, so they will migrate toward the anode under an electric field. All protein separations by SDS-PAGe were performed under reducing conditions, thus the samples were mixed with a buffer containing SDS and 1% reducing agent (LDS sample buffer 4x and Sample Reducing agent 10% respectively, from NuPage™) and incubated at 70ºC for 10 minutes to enable better denaturation. Thereafter, the samples were loaded onto pre-cast 10% NuPage Bis-tris polyacrylamide gels (NuPage™). The protein electrophoresis was performed in Mini Gel Tank or Xcell SureLock chambers (Thermo Fisher Scientific and Invitrogen, respectively) in MES running buffer (Invitrogen) at 150 V, for 45-60 min.

Coomassie Brilliant Blue staining

Protein bands in SDS-Page gels were visualized by Coomassie blue staining. This procedure is based on the electrostatic but non-covalent interaction between the amino and carboxyl groups of proteins, and the Coomassie brilliant blue dye; They bind in a non-specific manner to form a protein-dye complex. The formation of this complex stabilizes the negative charge form of the dye, producing a blue color. The Bio-Safe™ Coomassie stain from Bio-Rad Laboratories was used following the manufacturer's instructions.

Western blotting

To characterize the produced proteins, after running an SDS-PAGE, the proteins were transferred to a nitrocellulose membrane in a wet chamber in a transfer buffer with methanol 10% methanol at 400 mA for 1h. Subsequently, unspecific unions were blocked incubating the membrane with Roti-Block buffer 1x (Carl Roth GmbH) for 1 hour at room temperature. Then, primary antibodies were added and incubated at 4ºC overnight on a shaking platform. Afterward, the membranes were washed with TBST buffer 1x for 5 min 3 times. The membranes were developed with SuperSignal West Pico PLUS chemiluminescent substrate (Thermo Fisher Scientific) and pictured with Azure 400 visible western system (Biozym).

Immobilized metal affinity chromatography (IMAC)

Proteins carrying the His6x-tag were purified by metal affinity chromatography (IMAC) using Ni-NTA resins (Sigma-Aldrich/Merck). The isolation is based on the formation of a covalent bond between Histidine and Ni^{2+} ions built in an NTA (nitrilotriacetic acid) as a chelating agent to immobilize Ni into an agarose matrix. Harvested HEK-293-6E cells supernatants containing the secreted proteins were loaded onto columns of Ni-NTA matrix following the manufacturer's protocol. The HEK-293-6E cell supernatant and the steps during the purification process were size-fractionated by SDS-PAGE in order to analyze the purification process.

Thrombolytic activity of Amediplase

The principle of the assay is the release of a p-nitroanaline (pNA) by the enzymatic hydrolysis by the selective amino acid sequence of proteases. The rate of pNA is quantified by spectrophotometry at 405 nm and is proportional to the enzyme activity. pNAPEP-1588 (Cryopep Hemostasis coagulation), a specific synthetic chromogenic substrate for the measurement of the thrombolytic activity of Amediplase was used. The same amount of protein was incubated in the presence of 10% of pNAPEP-1588 (5 mM) in a buffer containing 10 mM Tris-Base, and 15% Tween 20. The reaction was carried out in a final volume of 200 µl, at 37 ºC for 30 minutes. Then, the reaction was stopped with 100 µl of 10% citric acid buffer and the absorbance was measured at 405 nm using the photometer plate reader victor 3, 1420 (Perkin Elmer).

2.2.4. Magnetic nanoparticles

Perimag® magnetic nanoparticles

With the aim of comparing the magnetosome samples with the commercially available alternative particles, Perimag® particles (Micromod Partikeltechnologie GmbH, Germany) have a hydrodynamic diameter (d_h) of 130 nm with a dextran shell. The magnetic core has a diameter d_C of about 25 nm.

Nanomag®/Synomag®-D particles

With the aim of MPI and navigation through magnetic fields, Micromod GmbH designed customized particles Nanomag®/Synomag®-D. These multicore particles consist of a combination of Nanomag® and Synomag® (Fig.11C) with hydrodynamic diameters in the range of 700 nm and with an iron core between 500 nm and 600 nm. Synomag®-D (Fig.11A) has excellent MPI imaging characteristics. In contrast, nanomag®-D particles (Fig.11B) have a high magnetic mobility performance. Synomag® particles are embedded in the iron oxide multi-cores of Nanomag®, to combine the imaging characteristics of Synomag®-D and the magnetic navigation of Nanomag®-D. For the bioconjugation of the particles with the thrombolytic protein, there were three different approaches.

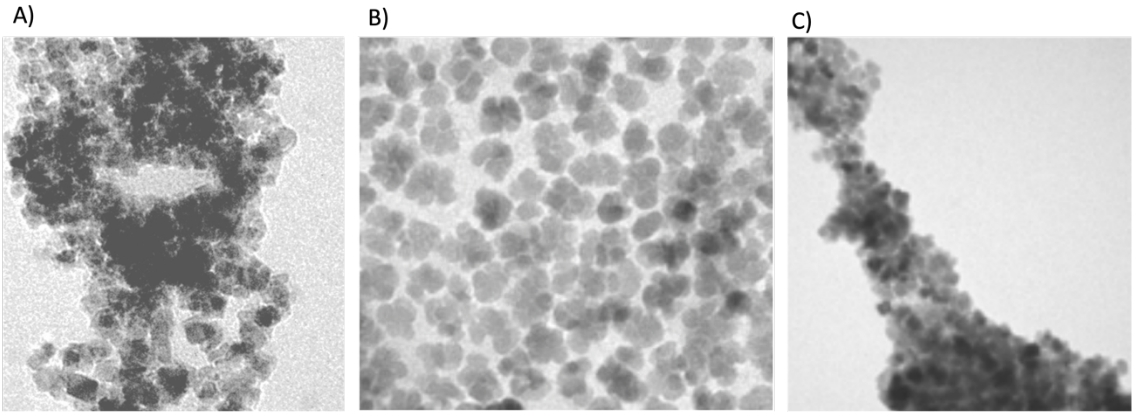

Figure 11. TEM images of Nanomag®-D, Synomag®-D and Nanomag®/Synomag®-D. (a) Nanomag®-D (250 nm section), (b) Synomag®-D (50 nm section) and (c) Nanomag®/Synomag®-D (20 µm section) particles. Pictures were taken from Micromod Partikeltechnologie GmbH website (https://micromod.de) on the 5th of June 2024.

Conjugation of biotinylated-Amediplase with streptavidin-coated Nanomag®/Synomag®-D particles

The motivation for Streptavidin-coated particles was due to the four subunits of streptavidin and the binding to four biotinylated molecules with one of the strongest covalent bonds in nature. Nanomag®-Synomag®-D particles were provided by Micromod GmbH, with covalently bound Streptavidin protein on the surface. First, avi-Amediplase was biotinylated after transient expression and before metal affinity chromatography using Bir-A500, a specific biotin ligation enzyme kit from Avidity LLC©. BirA-Biotin protein ligase activates biotin and binds to biotin-accepting proteins such as avi-tag peptide. Subsequently, biotinylated-Amediplase was isolated by Ni-NTA chromatography as described in protein biochemistry methods. The streptavidin-coated nanoparticles were first washed three times with phosphate-buffered saline solution (PBS) using a MagRack^{TM} 6. Then streptavidin particles were mixed with a known concentration of SBP- or biotinylated-Amediplase using low protein binding tubes and incubated in a roller-mixed rotator at 4ºC for 2 hours. To remove the excess of SBP- or biotinylated-Amediplase the magnetic particles were washed three times with PBS.

Conjugation of Actilyse® and Amediplase through ED-Carbodiimide crosslinker chemistry

An easy and rapid conjugation method for bioconjugation of carboxylate groups on particle surfaces is the carbodiimide chemistry. Nanomag®/Synomag®-D with carboxylic acid groups on the surface. They were activated with 1-ethyl-3-(-3-dimethylamino propyl) (ED) carbodiimide hydrochloride for direct conjugation to primary amines from the proteins via amide bonds as it is shown in Fig.12.

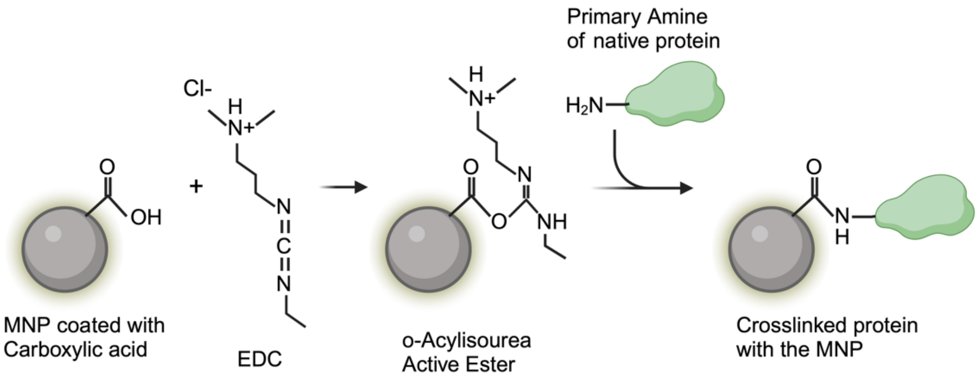

Figure 12. ED-Carbodiimide crosslinking reaction. EDC activates the carboxylic acid groups and an active O-Acylisourea intermediate is produced, which suffers a nucleophilic attack by the primary amino groups of the proteins. A new amide bond is formed where the carboxylic group was originally placed. MNP refers to Nanomag®/Synomag®-D particle. Image created with Biorender.

The ED-Carbodiimide crosslinker reaction was performed by Dr. Cordula Grüttner at Micromod GmbH laboratories.

Modification of amino groups with Traut's reagent and conjugation of Actilyse® and Amediplase with Maleimide click reaction.

An efficient method for the bioconjugation is the thiolated biomolecules binding to maleimide functionalized particles under mild conditions. Traut's reagent reacts with primary amines to introduce sulfhydryl (-SH) groups. Once the Thiol group is added, it can be rapid and chemoselective targeted by the maleimide to generate a thiosuccinimide product, as it is described in the maleimide click reaction in Fig.13.

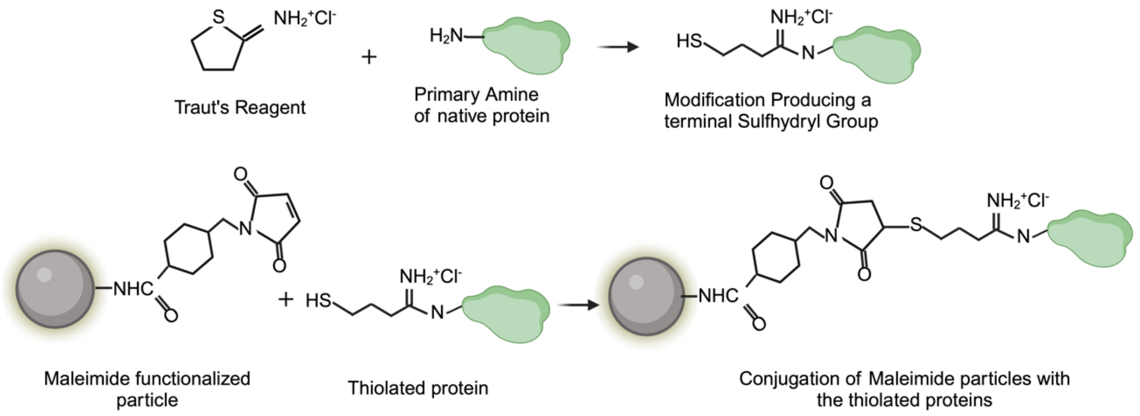

Figure 13. **Traut's reagent and maleimide click reaction.** Traut's reagent (2-Iminothiolane) (up) reacts with primary amines, making amidine compounds with sulfhydryl groups. Thus, the reaction between the free thiol and a maleimide group allows for crosslinking bioconjugation. Image created with Biorender.

The traut-maleimide click reaction was performed by Dr. Cordula Grüttner at Micromod GmbH laboratories.

Thrombolytic activity of conjugated MNP with Amediplase and Actilyse®.

The same amount of conjugated MNP was incubated in the presence of 10% of pNAPEP-1588 (5 mM) in a buffer containing 10 mM Tris-Base, and 15% Tween 20. The reaction was carried out in a final volume of 200 µl, at 37ºC for 30 minutes. Then, the particles were isolated with a MagRackTM 6, and the supernatant was transferred to a 96-well plate. The reaction was stopped with a 100 µl of 10% citric acid buffer and the absorbance was measured at 405 nm using the photometer plate reader victor 3,1420 (Perkin Elmer). The thrombolytic activity of different concentrations of the corresponding conjugated protein was measured in the same conditions to figure out the proportional sample conjugation.

In vitro magnetic targeted thrombolysis of conjugated Nanomag®/Synomag®-D nanoparticles.

Human blood was collected in S-Monovette® 3.2 % citrate tubes. Then, 50 µl of citrated blood was incubated with 50 µl of human thrombin (Hemoclot. CoaChrom diagnostica) in the narrow part of a 2 ml Pasteur glass pipette at 37ºC for 30 min. Clot sizes were 2-3 mm wide to 5-6 mm in length (see Fig.14). For *section 3.1.3,* after clot formation, the efficiency of thrombolysis, defined as the clot lysis time, was determined by measuring the time at which the clot flowed out of the tip of the glass dropper with neodymium N52 magnets below the clots to imitate magnetically targeted thrombolysis (see Fig.14). For *section 3.3.1*, the glass dropper was held up with µMACS™ Separator below the clots to imitate magnetically targeted thrombolysis. The µMACS™ Separator contains powerful magnets that induce a high-gradient magnetic field within where the clot is placed, resulting in an improved experimental setup because it provides a field strong enough to mimic magnetically better-targeted thrombolysis in MPI. The clot lysis time was measured for four conditions. At time zero, 1 ml of PBS was added as a clot stability control, 1 ml of PBS containing known µg of free-Amediplase, 1 ml of the equivalent µg of Amediplase conjugated to the particles, and the same amount of unconjugated particles (in mg). The experiments were recorded with a Go-Pro camera to determine the lysis time, with a maximum of 80 min video for results in *section 3.4*, and 60 min for results in *section 3.7.* The time rounding rule followed was as follows: the threshold is 30 seconds or below will round down the actual minute and 30 seconds and above will round up to the next minute.

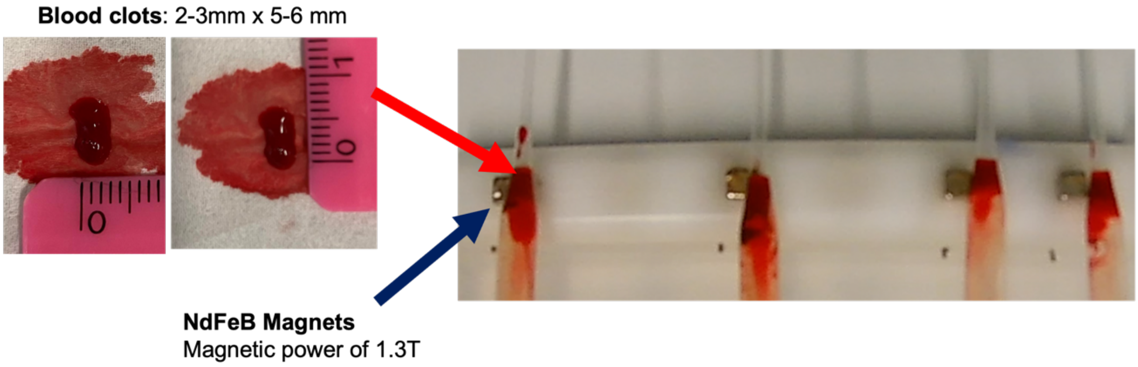

Figure 14. Blood clots and magnets were used for the *in vitro* experimental setup for magnetic targeted thrombolysis. Clot sizes ranged from 2-3 mm wide to 5-6 mm long. Neodymium N52 magnets (NdFeB magnets) are the strongest permanent magnets available commercially, with a magnetic power of 1.3 T.

2.2.5. MPS and MPI parameters.

Magnetic particle spectrometer (MPS) parameters

MPS has no spatial encoding and represents a 0-dimensional MPI scanner. The MPS results presented in this work are measured with a custom-built MPS at a drive-field frequency of f = 26.042 kHz and drive-field amplitudes (H) from 6 to 20 mT/µ0. The signal received from the excitation step is noise-filtered and transformed into Fourier space. The number of odd harmonics, and especially the value of the 3rd harmonic, can be extracted from the Fourier transformation to define the iron concentration and quantity. The spectra of odd harmonics of different particle types and batches of concentration can be compared to determine the signal-to-noise ratio (SNR) quality of the 3rd harmonic. The SNR indicates the lowest dilution of particles that can be achieved while still inducing a measurable signal. To ensure the quantification of the MPI signal for the operability of MPI in medical applications, all MPI particles must follow a positive and strong correlation of the signal concerning the particles' concentration. This means that the increase in particle concentration will correlate linearly with the increase in the MPI signal intensity.

The sample volume was 10 µl with 37.7 mM of iron for the initial experiment and the maximum signal response in time domain was measured at 20 mT/μ_0. Additionally, a dilution series from 1.1 mM to 35.7 mM of iron was pipetted to investigate the signal linearity for the most promising candidate by mapping the 3rd Harmonic.

This part of the project was performed together with Florian Thieben, M.Sc.

Bruker MPI scanner parameters

In contrast to MPS, MPI measures the nonlinear magnetization of superparamagnetic particles into a signal to image the spatial distribution of the magnetic material. All MPI measurements performed in this work are carried out with a preclinical MPI scanner (Bruker Biospin MRI GmbH, Germany). The scanner topology is an FFP setup, with a maximal gradient strength G_z up to 2.5 T/m in the z-direction and -1.25 T/m in the x- and y-directions. The drive filed amplitude can be regulated to a maximum of 14 mT in x-,y-, and z- directions. The excitation frequencies are given by f_X = 2.5/102 MHz, f_Y = 2.5/96 MHz, and f_Z = 2.5/99 MHz.

MPI must be calibrated every time one of the system parameters changes, including using a different tracer or a new particle batch, to ensure particles' reproducibility. The 2D system matrix was measured on a grid size of 25 mm x 25 mm x 13 mm filled up with 4 µL of the most promising candidate with a concentration of 35.7 mM iron. The magnetic-field amplitude was set to 12 mT/μ_0 with a maximum gradient of 2T/m, and the sample was measured an average of 100 times per grid position. To acquire the system matrix, the delta sample is moved to 20 mm × 20 mm × 20 mm central positions in a 40 mm × 40 mm × 20 mm FoV. Finally, the system matrix results were compared to a system matrix acquired with Perimag® as a tracer by signal-to-noise. The quality of the system matrices was assessed using the SNR values of the x-, y- and z-receive channel

Additionally, image reconstruction was performed for the most promising candidate. A 3D static resolution phantom consisting of 5 tubes with a common origin on one side of the phantom was filled up with 14 µL tracer with a concentration of 35.7 mM iron. From the origin, the arms extend at different angles within the XY and the YZ planes. Utilizing the reconstruction framework MPIReco.jl (Knopp et al., 2019), a single frame was reconstructed on an interpolated grid size of 51x51 pixels.

This part of the project was performed together with Florian Thieben, M.Sc.

2.3. Quantitative analysis and statistics

Statistical analyses and visualization were conducted with GraphPad Prism. Statistical significance was assessed by Turkey’s multiple comparison between group test, or Kruskal-Wallis test for multiple comparison. All values are presented as means ± SD.

3. Results

The results section is divided into two parts.

The first part describes the molecular engineering of Amediplase as a thrombolytic agent and the cloning, sequence optimization, and reformatting of recombinant tissue-Plasminogen Activator (rt-PA). Furthermore, its expression in a mammalian expression system was quantitatively and qualitatively analyzed, and the thrombolytic activity of the purified protein was characterized. Next in order in this work, the direct conjugation of Amediplase with streptavidin-coated Nanomag®/Synomag®-D particles was functionally characterized, focusing on the thrombolytic activity of the coated particle *in vitro*. Consequently, new techniques for Amediplase-Nanomag®/Synomag®-D functionalization techniques are described. By this, we could evaluate the efficacy of conjugated particles that decreased the thrombolysis time *in vitro* experiments.

In the second part, we isolated magnetosome particles from wildtype (WT) and seven different *M. gryphiswaldense* deletion strains with core diameters in the size range from 20 to 40 nm. After analyzing the size distribution by transmission electron microscopy (TEM), we used magnetic particle spectroscopy (MPS) to identify particle “candidates” with promising 1D-signal responses compared to the standard MPI tracer Perimag®. Our results show that certain mutant magnetosomes resulted in significantly improved MPS signals. To ensure its quality for 3D MPI, an MPI system matrix was measured and compared to Perimag®. Afterward, an open 3D static resolution phantom was filled up with the selected magnetosome *ΔfeoAB1* and imaged with an MPI scanner. Our data suggest that engineered magnetosomes are promising MPI nanoparticle agents.

3.1. Amediplase protein engineering design

For the *de novo* protein design and synthesis, the amino acid sequence of Amediplase is composed of the 1-3 and 176-275 amino acids of the kringle-2 domain of t-PA, which binds and activates Plasminogen (P00750 reference in www.uniprot.org), and the 159-411 amino acids of the catalytic serine protease domain of scu-PA (single-chain urokinase plasminogen activator, P00749 reference in www.uniprot.org) (see Fig.15).

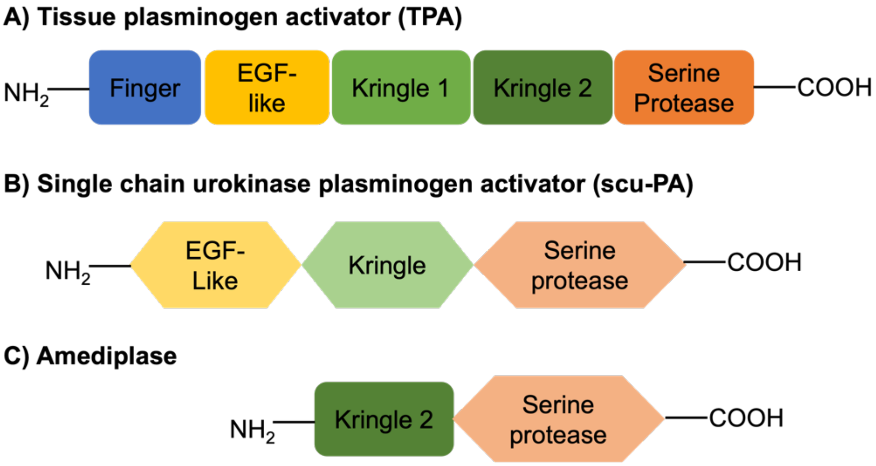

Figure 15. ***2-D domain cartoon depiction* of** A) Tissue plasminogen activator (TPA), B) Single chain urokinase plasminogen activator (scu-PA), and C) Amediplase.

The proteins were expressed with three different tags in the N-terminus to arrange different approaches for coupling the proteases with the magnetic particles. Streptavidin Binding Protein (SBP) tag, a 38 amino acid sequence that in recombinant proteins binds to streptavidin (see Fig.16A). Streptavidin, as a homo-tetramer, has strong non-covalent interaction with biotin (Fig.16B), and finally, avi-tag, a popular fusion 15 amino acid peptide with powerful and versatile properties (Fig.16C). Streptavidin and SBP have direct chemical attraction for their affinity molecule. However, avi-tag does not directly bind to biotin; it involves a targeted enzymatic activation to get biotinylated. Figure 16 shows a Schematic diagram of investigated approaches for bioconjugation Amediplase onto the magnetic nanoparticles.

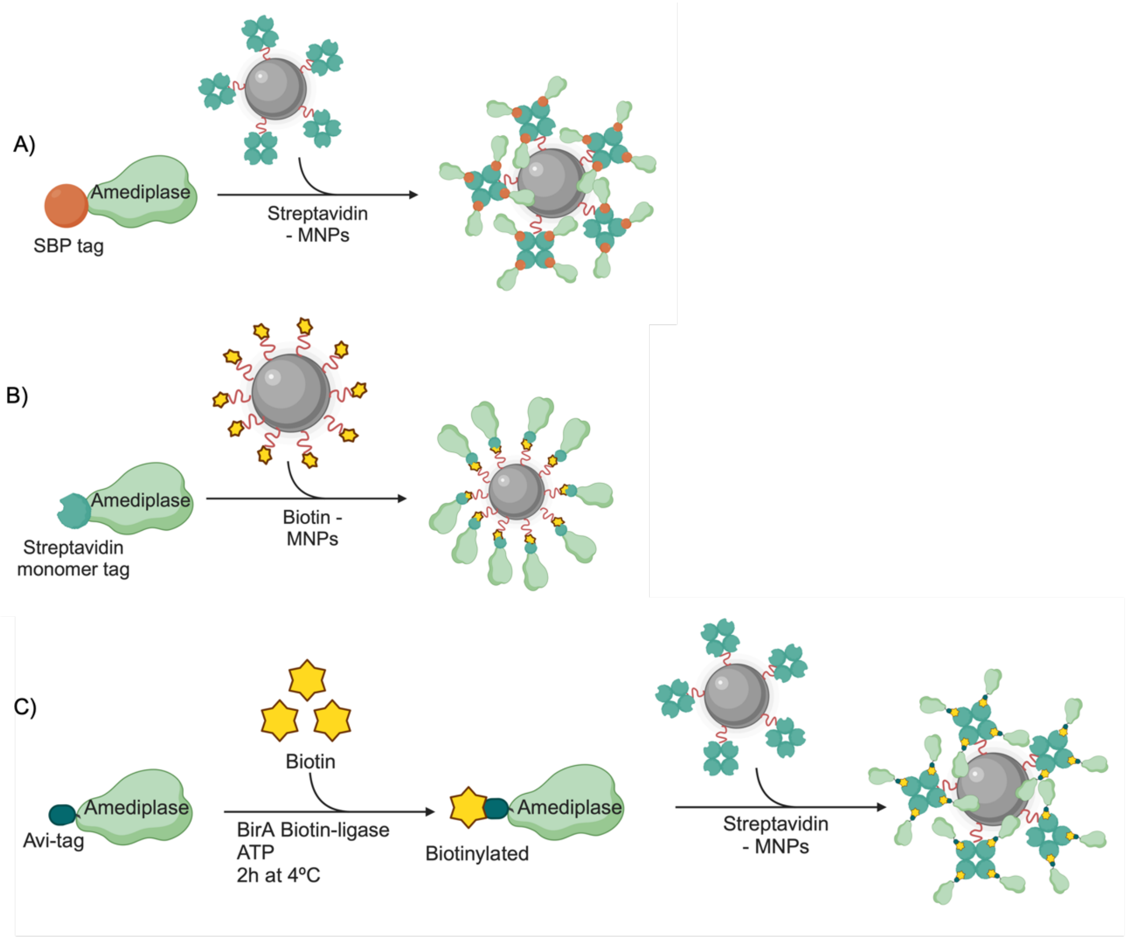

Figure 16. Schematic diagram of investigated approaches for bioconjugation Amediplase onto the magnetic nanoparticles. A) direct conjugation of Streptavidin binding protein (SBP) tagged Amediplase with streptavidin-coated MNP. B) Direct conjugation of streptavidin monomer-modified Amediplase with biotin-coated MNP. C) Biotinilation of avi-tag Amediplase with BirA biotin-ligase and the direct conjugation of biotinylated-Amediplase onto streptavidin MNP. MNP refers to Nanomag®/Synomag®-D particles. Image created with Biorender.

Restriction analysis of final construct pCSE2.5 reflected successful subcloning of Amediplase genes from cloning vector to expression vector. The size of the final expression construct was between 6400 and 6600bp, and digestion of this construct with NotI and XbaI restriction sites resulted in two different fragments of linearized pCSE2.5 vector (around 5000bp) and the Amediplase clones (see Fig.17).

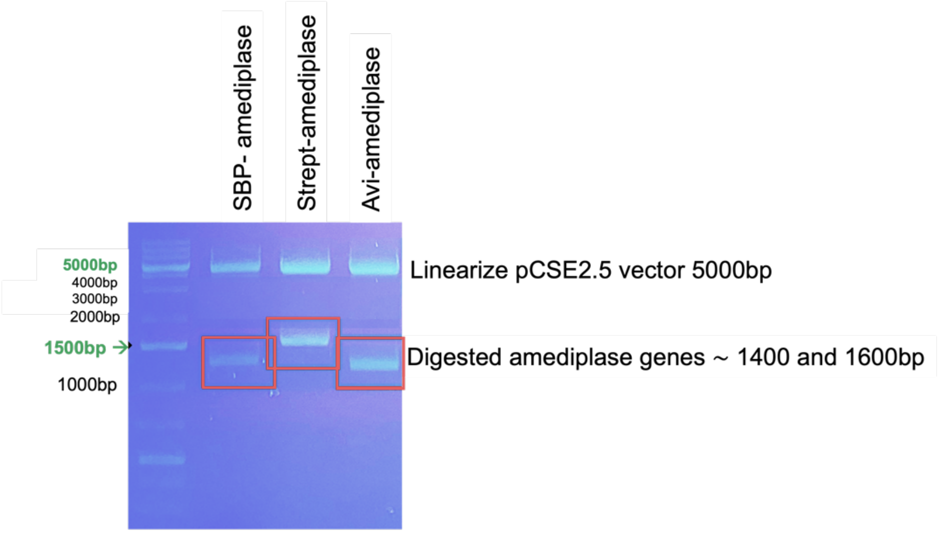

Figure 17. Agarose gel electrophoresis of restriction digestion of Amediplase-pCSE2.5 positive recombinants. Line 1: marker. Lane 2-4; lower bands: SBP, Strept, and Avi Amediplase PCR positive recombinants. Upper bands: linearized pCSE2.5 vector.

3.1.1. Expression, purification, and characterization of engineered Amediplase

The engineered Amediplases designed in *section 3.1*. were produced as secretory proteins in a mammalian expression system. HEK-293-6E cells were transiently transfected with SBP, streptavidin, and avi-tagged Amediplase expression constructs. After five days, the recombinant proteins from the cell supernatant were purified via Nickel Nitrilotriacetic acid (Ni-NTA) affinity chromatography. In the case of the proteins with avi-tag, they must be biotinylated with a BirA-500 kit before purification. Production and purification were monitored by SDS-PAGE analysis of aliquots of the cell's supernatant, column flows through, column wash, and elution steps. Eluted proteins were highly concentrated (1 mg/ml), and the buffer was exchanged with phosphate-buffered saline (PBS) via centrifugation filters with a cut-off of 30 kDa. Production yields were typically between 3-4 mg per 90 ml of transfected HEK-293-6E cells. SDS-PAGE analysis of production and purified proteins confirmed the high purity of the engineered proteins. Thus, in SDS page analysis (Fig.18B), expression of SBP-Amediplase and avi-Amediplase was observed successfully compared their molecular weight to the pre-stained protein molecular marker. Streptavidin-tagged Amediplase was unable to produced due to the intracellular and the

Freestyle 293TM expression medium biotin content (0.5 µg per 10^8 cells and 100 µg of biotin per liter respectively).

The proteins produced were detected and analyzed by western blot with the 6-histidine-tag antibody (Fig.18C). Protein expression of SBP-Amediplase and avi-Amediplase was characterized by a single and strong intensity band, corresponding to the right molecular weight on the western blot result, 53 and 49 kDa correspondingly. Moreover, with such a sensitive technique we could confirm the absence of Streptavidin-tagged Amediplase with the negative (white) band at 55kDa. The binding capacity of SBP and biotinylated-Amediplase for streptavidin was determined by western blot using streptavidin peroxidase antibody. The bond of SBP and biotinylated-Amediplase was positive for streptavidin as it is shown on the western blot result (Fig.18C). Negative control, avi-Amediplase, was added to confirm its complete biotinilation.

Tissue plasminogen activators are serine proteases, which activate plasminogen by cleaving a single arginine-valine bond of the plasminogen molecule. The protease activity of 4.5 µg of each protein was examined with the specific synthetic chromogenic substrate for the measurement of the tissue plasminogen activators and other serine protease activity: pNAPEP-1588. Proteolytic enzymes such as Amediplase, hydrolyze the tripeptide bond of pNAPEP-1588. The process is usually highly specific due to the p-nitroanaline (pNA) peptide bond adjacent to Arg and Val amino acids is exclusively cleaved and the pNA is released into the solution. The protease activity of Amediplase is thus determined by the rate at which p-nitroanaline is released. The color change can be followed spectrophotometrically at 450 nm. A simple, specific and reproducible method for the determination of thrombolytic activity for SBP-Amediplase and avi-Amediplase is shown in Fig.18D. In addition, it is confirmed that the protease activity, with absorption at 450 nm close to 2 units, comes from the recombinant proteins, when we compared it to the negative absorption of the supernatant of untransfected cells.

Thus, successful expression and production of full length of recombinant SBP-Amediplase and avi-Amediplase as thrombolytic proteins using HEK-293-6E cells system is asserted.

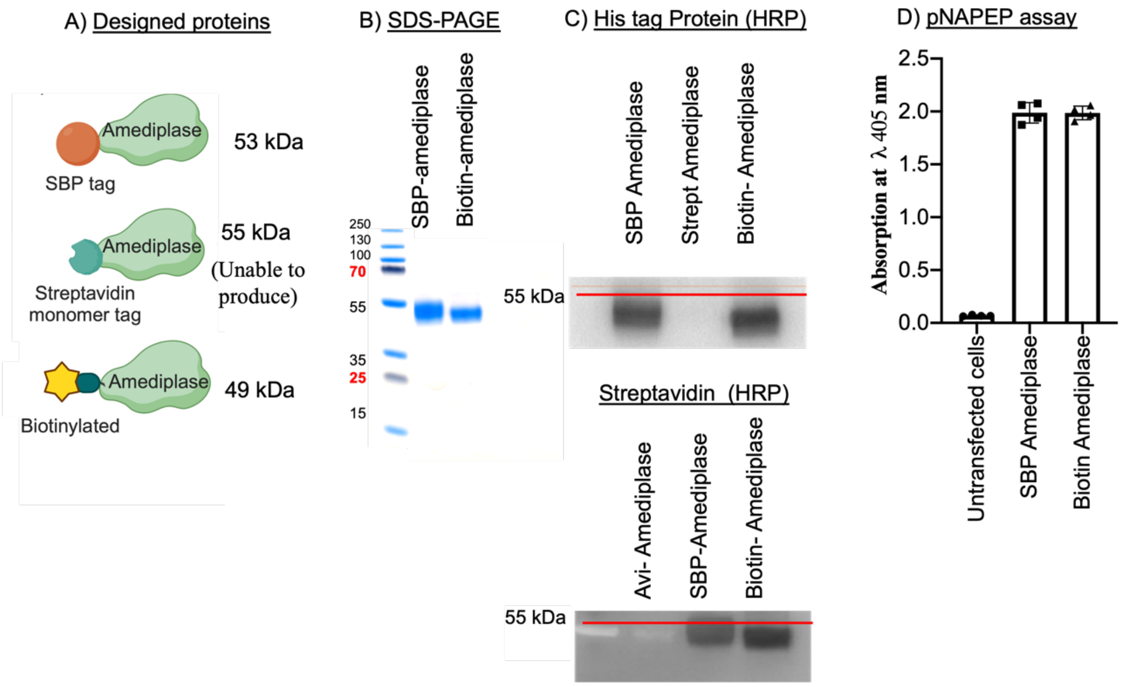

Figure 18. **Expression, purification, and chemical characterization of engineered Amediplase.** A) Schematic information of the 3 different tags added onto Amediplase and their mass in kDa. B) SDS-PAGE analysis of purified engineered Amediplase. Coomassie-stained SDS-PAGE gel loaded with 6µg/well of affinity-purified protein. SBP-Amediplase (lane 1) and avi-Amediplase (lane 2). C) Western blot of purified proteins with His-tag protein antibody (HRP) and Streptavidin HRP antibody. D) Bar diagrams illustrating the thrombolytic activity of produced proteins compared to the supernatant of untransfected cells were measured with the chromogenic substrate pNAPEP-1588 (Cryopep Hemostasis coagulation) and the absorbance was measured at 405 nm. Data are average measurements ± SD (n=4).

3.1.2. Conjugation of SBP-Amediplase and biotin-Amediplase with Nanomag®/Synomag®-D streptavidin-coated nanoparticles

Iron oxide nanoparticles Nanomag®/synomag®-D coated with Streptavidin on the surface with a concentration of 15 mg of particles per ml were used for the bioconjugation reaction. The method of conjugation was based on the approach described earlier in Fig.16. The binding of streptavidin-coated nanoparticles to SBP- and biotinylated-Amediplase was monitored by measuring the concentration of protein before and after the conjugation; the difference of concentrations would be equal to the conjugated protein on the particles. However, the outcomes obtained between the protein concentrations before and after the conjugation using 3 different techniques: BCA, microBCA and Nanodrop2000, were not reliable because of the high differences within the 3 technique results.

Due to the measurement inaccuracies of these methods, to accurately detect the concentration of immobilized SBP and Biotin-Amediplase on the streptavidin-coated particle, we decided to measure the functional activity of conjugated nanoparticles with the pNAPEP-1588 chromogenic substrate, specific for plasminogen activators used in *section 3.1.1*. The bar graph in Fig.19 shows the relative activity of coupled SBP- and Biotin-Amediplase on streptavidin-coated particles, compared to a given signal from a known quantity from 1 to 7.5 µg of Amediplase. The results suggest that conjugated particles preserved the enzymatic activity of Amediplase. 40 µl of immobilized biotin-Amediplase on the particles had the same thrombolytic activity as 2.5 µg of Amediplase. As a result, the binding capacity of streptavidin-coated Nanomag®/Synomag®-D particles is up to 4 µg of biotinylated-Amediplase per 1 mg of particles. Conjugated SBP-Amediplase presented a relative thrombolytic activity of 1 µg of Amediplase, resulted in 1.7 µg of SBP-Amediplase per 1 mg of particles.

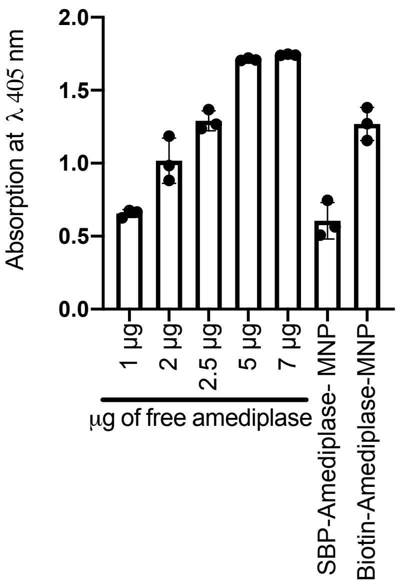

Figure 19. Biotinylated-Amediplase conjugated to streptavidin-coated Nanomag®/Synomag®-D particles showed higher thrombolytic activity compared to functionalized SBP-Amediplase. Bar diagrams illustrating the protease activity of SBP and biotin-Amediplase functionalized onto the MNP were measured with the chromogenic substrate pNAPEP-1588 (Cryopep Hemostasis coagulation) and the absorbance was measured at 405 nm. Results show average measurements ± SD (n=3). MNP refers to streptavidin-coated Nanomag®/Synomag®-D particles.

3.1.3. *In vitro* magnetic targeted thrombolysis of biotin-Amediplase conjugated to streptavidin-coated Nanomag®/Synomag®-D nanoparticles

The *in vitro* thrombolysis of clots in the absence of flow was investigated for unconjugated streptavidin-coated Nanomag®/Synomag®-D, free-Amediplase, and biotin-Amediplase conjugated to the particles, due to its higher concentration on the particles compared to SBP-Amediplase. At time zero we added: 1 ml of PBS as a clot stability control, 1 ml of PBS containing 8 µg free-Amediplase, 1 ml with 8µg of biotin-Amediplase conjugated to the particles, and the equivalent same amount of unconjugated particles: 2 mg.

In our study, we observed that the conjugated particles preserved the enzymatic activity of Amediplase and allowed for thrombolysis (Fig.20). The clot lysis capacity of 8µg of biotin-Amediplase conjugated to the nanoparticles showed a significantly reduced clot lysis time with an average of 33 min ± 29 min (n=5), and therefore, higher thrombolysis compared to the other conditions; 72 min ± 13 min (n=7) for the clot stability control (PBS), 70 min ± 19 min (n=8) for 1 ml of PBS containing 8 µg free-Amediplase and 62 min ± 28 min (n=8) for 1 ml with 2 mg of unconjugated particles. However, in some of the situations the blood clot lysis efficiency of the conjugated particles was equivalent to the non-conjugated particles group (lysis times between 10 and 33 min), suggesting that the physical force generated by the particles under the magnetic steering was enough to cause an angioplasty-like effect. In most of the cases, there was no thrombolytic activity for the free-Amediplase condition (lysis time of 80 min), which is a critical demonstration of the effectiveness of the strategy. In conclusion, a higher binding capacity of the particles was required in order to accelerate the thrombolytic activity of the conjugated particles. In addition, the high Amediplase binding capacity would decrease the actual amount of 2 mg of particles and the possible magnetic force of the particles on the clot, and it would demonstrate the efficacy of the Amediplase.

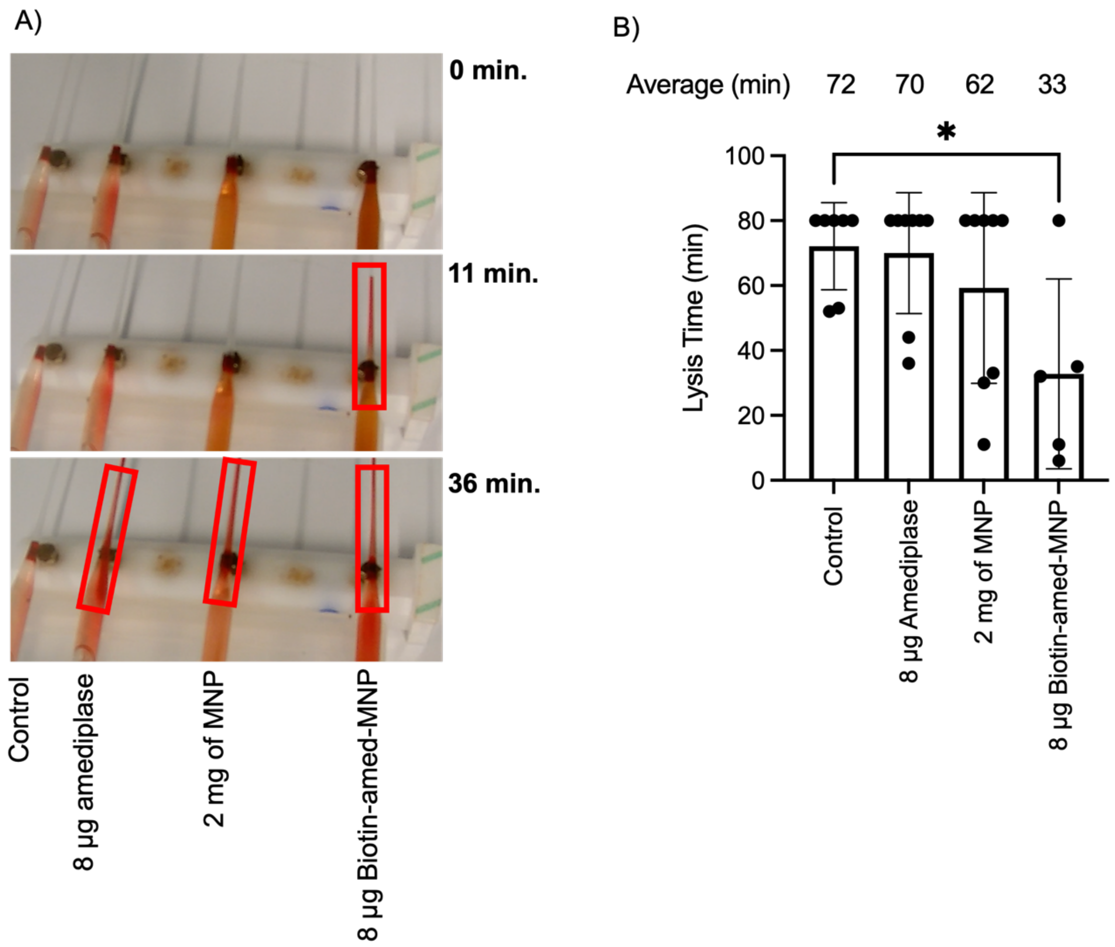

Figure 20: ***In vitro* results for thrombolysis of 8 µg biotin-Amediplase conjugated particles showed a reduction of lysis time to 50%.** A) Video shots of the experimental setup situation at the time marked on the right. Glass capillaries with the blood clot dissolved are marked in red. B) Bar diagrams illustrating the results for the *in vitro* thrombolysis for PBS (control) (n=7), 8 µg of free-Amediplase (n=8), 2 mg of MNP (n=8) and 8 µg of biotin-Amediplase bound to MNP (n=5). Data are averages ± SD. Tukey's multiple comparisons between groups test, p-value>0.05. One asterisk (*) identifies adjusted P values between 0.05 and 0.01 MNP refers to streptavidin-coated Nanomag®/Synomag®-D particles.

3.2. Thrombolytic activity of coated Amediplase and Actilyse® Nanomag®/Synomag®-D via maleimide click reaction

To achieve higher binding capacity of the particles, conjugating thiolated biomolecules to maleimide functionalized particles under mild conditions is an efficient method to immobilize and preserve protein functionalities. We decided to have the possibility to bioconjugate the World Health Organization approved

Actilyse® (alteplase) for thrombolysis and compare it to the Amediplase produced in our laboratory. Actilyse® is the commercial name of rt-PA and the only pharmacological treatment currently approved during the acute phase of ischemic stroke. The maleimide-thiol conjugation of Amediplase and Actilyse® reaction on crosslinked dextran particles was carried out at Micromod Partikeltechnologie GmbH laboratories by Dr. Cordula Grüttner's group. Once again, the relative thrombolytic activity of the conjugated particles was measured with the chromogenic substrate pNAPEP-1588 as it was performed before. Amediplase showed a higher binding capacity, 9 and 5 µg of Amediplase per mg of particles (Fig.21 batch 12322 and 12122), compared to Actilyse®, 3 and 5.5 µg of Actilyse® per mg of particles (Fig.22 batch 12222 and 12422). However, the total amount of protein bound to the particles was not significantly higher than the previously streptavidin-coated particles results (4µg of biotin-Amediplase per mg of particles). In conclusion, conjugating Amediplase and Actilyse® to dextran crosslinked particles via maleimide-thiol reaction resulted in low thrombolytic functionalization in both cases.

3.3. Thrombolytic activity of coated Amediplase and Actilyse® Nanomag®/Synomag®-D via ED-Carbodiimide crosslinker chemistry

One of the most popular alternative approaches for higher particles' binding is the functionalization of primary amine functional groups with lysine side chains that involve the use of a cross-linking agent, the ED-Carbodiimide. It provides the coupling of magnetic nanoparticles coated with carboxylic groups on their surface. The carbodiimide crosslinker reaction was carried out at Micromod Partikeltechnologie GmbH, by Dr. Cordula Grüttner's group. The comparison of the relative thrombolytic activity by the chromogenic substrate assay of Amediplase and Actilyse® conjugated to dextran-coated Nanomag®/Synomag®-D via ED-Carbodiimide crosslinker chemistry is shown in Fig.21 for Amediplase (batch 19222) and Fig.22 for Actilyse® (batch 12022). The EDC crosslinker chemistry conjugation strategy resulted in higher binding than streptavidin-coated conjugated particles for Amediplase (batch 11922). The loading activity of bound

Amediplase increased from 4 µg to 40 µg per mg, ten times more conjugation rate onto the particles. On the other hand, Actilyse® binding (batch 12022) was still 4 µg per mg of particles. The commercial Actilyse® contains two physiological forms of rt-PA, the single chain (sc-tPA) and the two chains rt-PA (tc-tPA). The route from the single chain to the two-chain tPA form involves the hydrolysis of the kringle-2 and the protease domain in the peptide bond linking the Arg275 and the Ile276. However, both parts of the protein remain connected by the disulfide bridge between Cys299 and Cys300, shaping a heavy and a light tPA chain. Nonetheless, both sc-tPA and tc-tPA, in the presence of fibrin, resulted in the same catalytic activity (Thelwell & Longstaff, 2007) , and the difference of primary amines available between rT-PA and Amediplase for ED-Carbodiimide crosslink chemistry is not significant. Therefore, we suspected that the low binding capacity and protease activity of conjugated Actilyse® was due to steric hindrance because rt-Pa is bigger than Amediplase, resulting in a low conjugation efficiency.

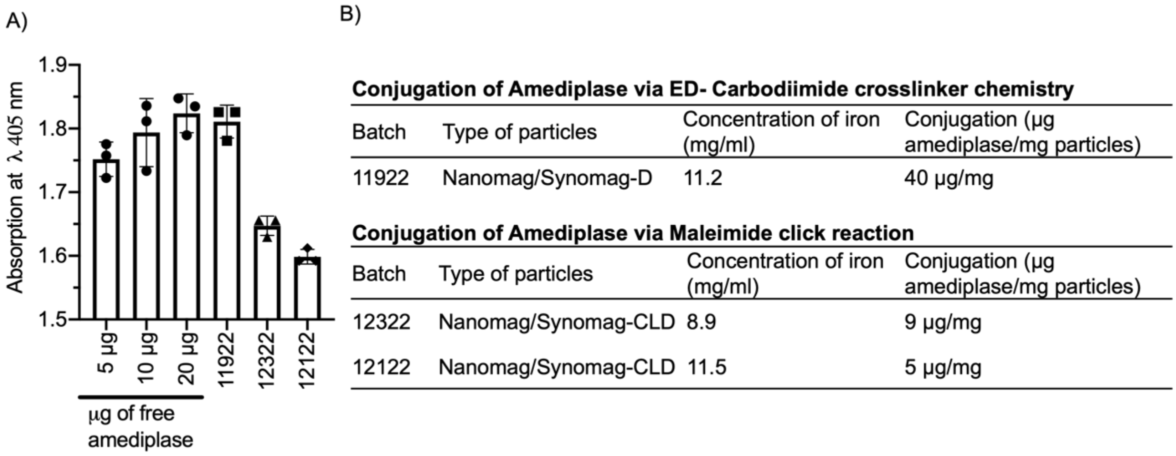

Conjugation of Amediplase via ED- Carbodiimide crosslinker chemistry

Batch	Type of particles	Concentration of iron (mg/ml)	Conjugation (µg amediplase/mg particles)
11922	Nanomag/Synomag-D	11.2	40 µg/mg

Conjugation of Amediplase via Maleimide click reaction

Batch	Type of particles	Concentration of iron (mg/ml)	Conjugation (µg amediplase/mg particles)
12322	Nanomag/Synomag-CLD	8.9	9 µg/mg
12122	Nanomag/Synomag-CLD	11.5	5 µg/mg

Figure 21. **Conjugation yields of Amediplase with Nanomag®/Synomag®-D via ED-Carbodiimide crosslinker chemistry and maleimide click reaction**. (A) Bar diagrams illustrating the thrombolytic activity of conjugated particles compared to different concentrations of Amediplase. Data are averages ± SD (n=3). (B) Table of final concentration.

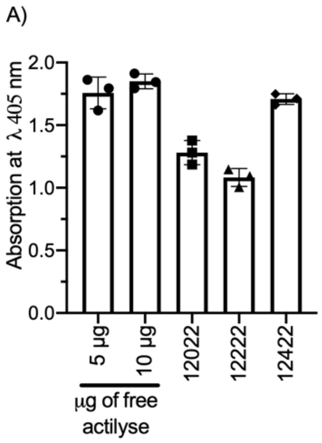

B)

Conjugation of Actilyse®(r-TPA) via ED- Carbodiimide crosslinker chemistry

Batch	Type of particles	Concentration of iron (mg/ml)	Conjugation (µg Actilyse®/mg particles)
12022	Nanomag/Synomag-D	11.2	4µg/mg

Conjugation of Actilyse®(r-TPA) via Maleimide click reaction

Batch	Type of particles	Concentration of iron (mg/ml)	Conjugation (µg Actilyse®/mg particles)
12222	Nanomag/Synomag-CLD	11.5	3 µg/mg
12422	Nanomag/Synomag-CLD	8.9	5.5µg/mg

Figure 22. **Conjugation yields of Actilyse® with Nanomag®/Synomag®-D via ED-carbodiimide crosslinker chemistry and maleimide click reaction.** (A) Bar diagrams illustrate the thrombolytic activity of conjugated particles compared to different acetylene concentrations. Data are averages ± SD (n = 3). (B) Table of final concentration.

3.3.1. *In vitro* magnetically targeted thrombolysis of Amediplase conjugated to Nanomag®/Synomag®-D via ED-Carbodiimide crosslinked reaction

Static *in vitro* thrombolysis in a vertical position was determined for four conditions by measuring the clot lysis time at which the clot flowed out of the tip of the glass dropper. To imitate magnetically targeted thrombolysis, this time the pipettes were held up with µMACS ™ Separator below the clots (Fig.23A). The µMACS Separator contains powerful magnets that induce a high-gradient magnetic field bordering the area where the clot is placed. This developed an improved experimental setup with strong enough magnetic fields to mimic magnetically better-targeted thrombolysis in MPI. Once more, at time zero we added: 1 ml of PBS as a control for clot stability, 1 ml of PBS containing 60 µg free Amediplase, 1 ml of the equivalent µg of Amediplase conjugated to the particles, and the same amount of unconjugated particles (1.5 mg).

In our study we observed that the conjugated particles via ED-Carbodiimide crosslink reaction preserved the enzymatic activity of Amediplase and allowed for thrombolysis. Most of the particles were likely influenced by the magnetic field of the µMACS ™ separator and concentrated at the clot site, which resulted in a higher concentration of Amediplase at the clot location. The clot lysis capacity of 60 µg Amediplase conjugated nanoparticles showed a significantly reduced clot lysis time of 8 min ± 6 min (n=5) and therefore, a higher thrombolysis effect compared to the other conditions (see Fig.23B). However, the reduction to 1.5 mg of unconjugated particles to deliver the exact Amediplase dosage did not lead to a reduced force exerted from the MNP on the clot, compared to the previous results in *section 3.1.3*. This time the clot lysis time for the unconjugated particles was 26 min ± 10 min (n=5). The reason of this result could be the higher magnetic fields provided by the µMACS ™ Separator in comparison to the previous setup in *section 3.1.3*. With free 60µg of Amediplase, there is a thrombolytic activity of 30 min ± 18 min (n=5), a high significant difference in clot lysis time compared to the 60 µg of Amediplase conjugated to the particles, and a demonstration of thrombolytic effectiveness for this condition. The clot stability control (PBS) presented the slowest lysis time of 51 min ± 12 min (n=5). In conclusion, this high binding capacity of the particles by the ED-Carbodiimide crosslinked reaction showed a significantly accelerated thrombolytic activity for the conjugated group. Interestingly, unconjugated particles and free Amediplase groups showed reduced clot lysis time compared to the previous results in *section 3.1.3.*

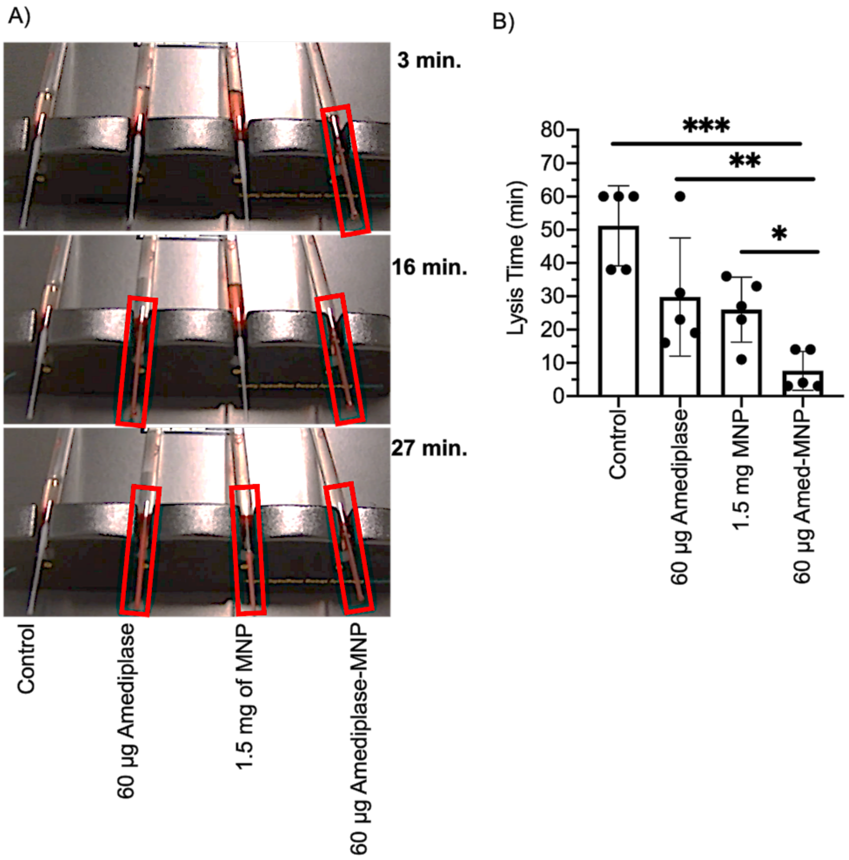

Figure 23. 60 ug of Amediplase conjugated to Nanomag®/Synomag®-D via EDC chemistry reduced the thrombolysis time to 75%. A) Video shots of the experimental setup situation at the time marked on the right. Glass capillaries with the blood clot dissolved are marked in red. B) Bar diagrams illustrating the results for the *in vitro* thrombolysis for PBS (control), 60 µg of free-Amediplase, 1,5 mg of MNP, and 60 µg of Amediplase bound to MNP. Data are averages ± SD (n=5). Kruskal-Wallis test for Multiple comparison. α=0.1. One asterisk (*) identifies adjusted P values between 0.1 and 0.05, two asterisks (**) identify adjusted P values between 0.05 and 0.01, and three asterisks identify adjusted P values <0.01. MNP refers to Nanomag®/Synomag®-D particles.

3.3.2. *In vitro* thrombolysis with a 3D stenosis simulation phantom in MPI

As this work provides an outlook into the current possibilities to utilize magnetic targeted therapy in MPI, the principle of using magnetic particles and MPIN needs to be further developed. As a first step, the artificial 100% stenosis has already been tested in Griese et al., (2020), and the experimental setup is already being modified. The stenosis has to be replaced with a natural blood clot in an artificial bifurcation phantom (Fig.24D). Then, the effect of functionalized particles must be demonstrated within a bifurcation flow experiment on actual blood clots (Fig.24C-E). The possibility of mimicking realistic conditions will be investigated due to the difference between the frequency of the heart (about 60 Hz) and the peristaltic pump used that produces a constant volume current (Fig.24B). Moreover, the body temperature of 37ºC must be kept within the system (Fig.24B) to have an efficient thrombolytic activity of the conjugated particles. All these parameters were being set up together with Fynn Förger M.Sc. To this end, moving the particles towards the blood clot is challenging because the total blockage leads to high resistance, and the particles are pulled out of the stenosis back into the flowing current due to negative pressure generated by the flowing water. Some of the latest results are presented in Fig.24.

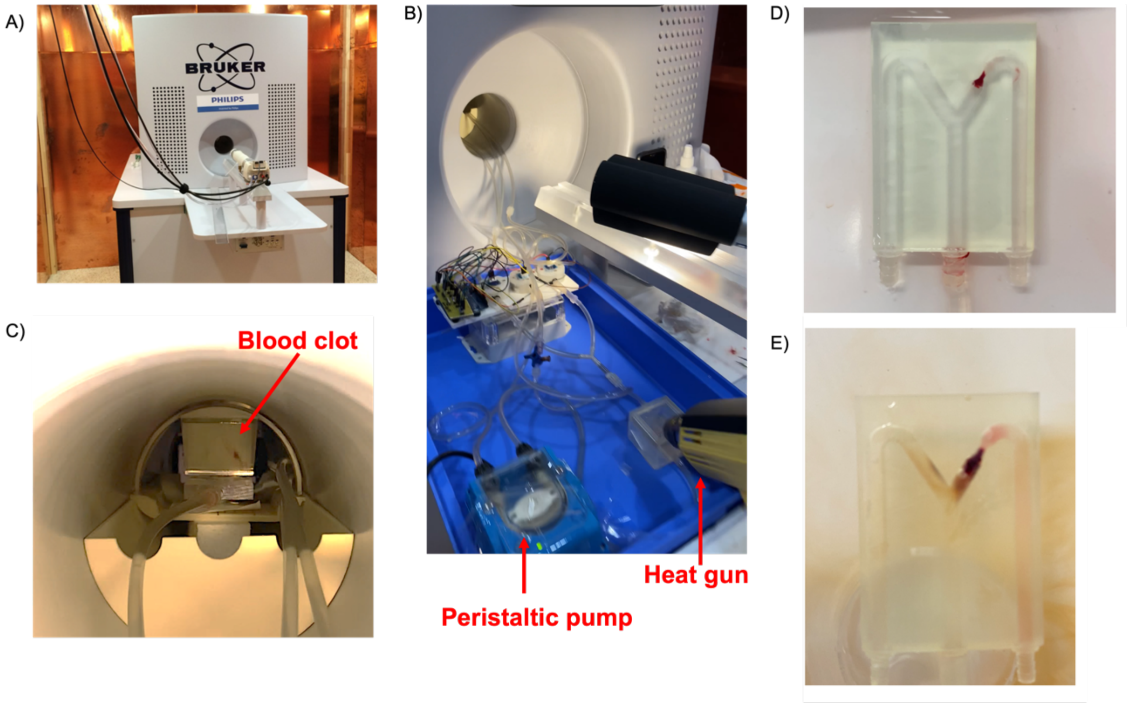

Figure 24. *In vitro* MPIN experiment setup pictures. A) A Bruker scanner is inside the room with copper shielding. B) A bifurcation flow experiment was set up with a peristaltic pump and a heat gun. C) A bifurcation phantom visible inside the mirror was placed inside the MPI and bore with a blood clot in one of the right branches. D) Blood clot in the right branch of the 3D stenosis phantom. E) Blood clot and particle accumulation on the clot side after an *in vitro* MPIN experiment.

To fully harness the potential of iron oxide nanoparticles in MPI, it is essential to identify the optimal tracer with specific magnetic and physical properties. Magnetosomes, the biominerals produced by magnetotactic bacteria, are membrane-enclosed iron oxide nanoparticles composed of monocrystalline magnetite (Fe_3O_4). These particles exhibit large size and high uniformity in both shape and size, making them ideal candidates for MPI. In this study, we isolated particles from 7 different *M. gryphiswaldense* deletion strains, varying in average particle size, by analyzing their physical and magnetic properties in comparison to Perimag®.

3.4. Structure characterization of magnetosome strains

In Fig.25, TEM analysis of magnetosome crystallite size is designated as a mean core diameter. Depending on the strain, magnetosomes with core sizes ranging from 21 and 40 nm were produced and represented in a violin plot. As a general rule, all magnetosome types show a broad size distribution resulting in polydispersity due to the presence of immature magnetosomes. However, it is interesting to note a weak tendency towards lower standard deviations for samples with small core diameters. In that instance, Δ*feoAB1*, Δ*feoAB12*, Δ*Fe*4, and Δ*mmsF/mamF* mutant strains showed significantly smaller mean core diameters than the WT. Their particle size obtained from TEM agrees well with the domain size range between 21 and 28 nm for superparamagnetic particles. The smallest mean size is observed for mutant Δ*feoAB12* at 21.4 nm, and simultaneously, the lowest size distribution. In contrast, Δ*mam*R, Δ*mam*J, and Δ*mam*F magnetosome mutant strains presented bigger sizes and within the ferrimagnetic size range, from 30 to 36 nm.

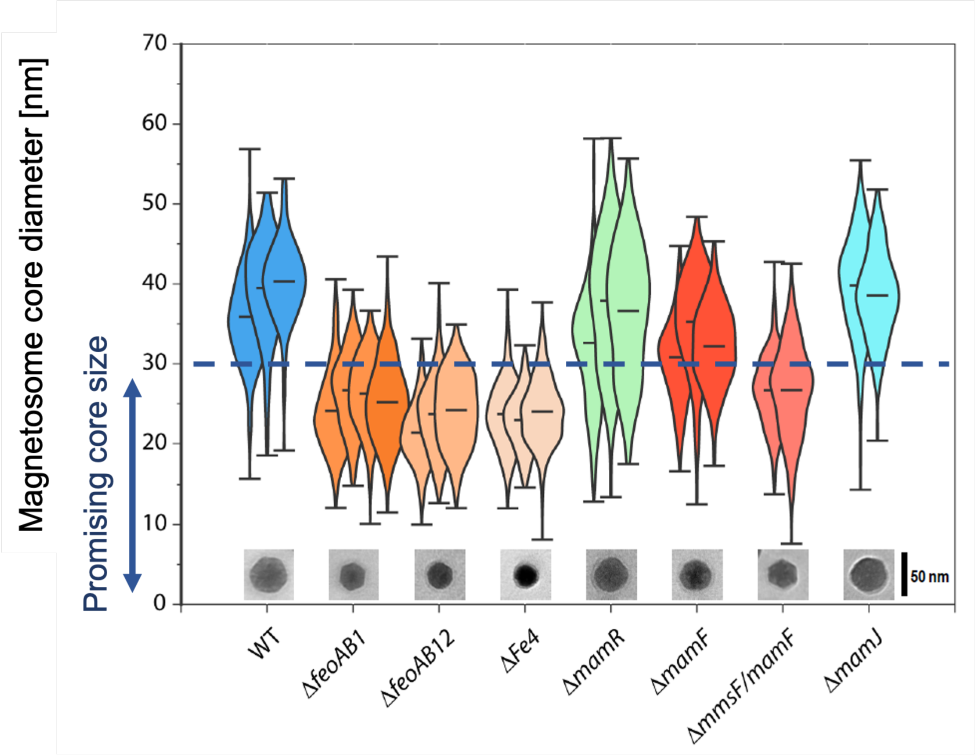

Figure 25. Violin plot of the core size distribution of magnetosomes isolated from different *M. gryphiswaldense* strains as indicated. TEM analyzed each particle suspension, and ImageJ software was used to determine the core diameters ($n \geq 350$). The insets show TEM micrographs of a representative magnetosome particle isolated from the respective strain.

Cell morphology of the different magnetosome strains and wild type is investigated using TEM images. In Fig.26, TEM images revealed matured magnetosomes of the ferrimagnetic size range, with a typical cuboctahedral structure. Nevertheless, it is difficult to determine the 3 dimensions lattice of each crystal without thickness measurements. Magnetosomes with a core diameter larger than 30 nm are probably magnetically blocked at room temperature and a tendency to form chains, rings or aggregates was additionally observed due to magnetic interactions. Overall, TEM images for the defined small mutant samples show a slight difference in the magnetosome-like morphology and are relatively well dispersed, which could suggest superparamagnetic behavior.

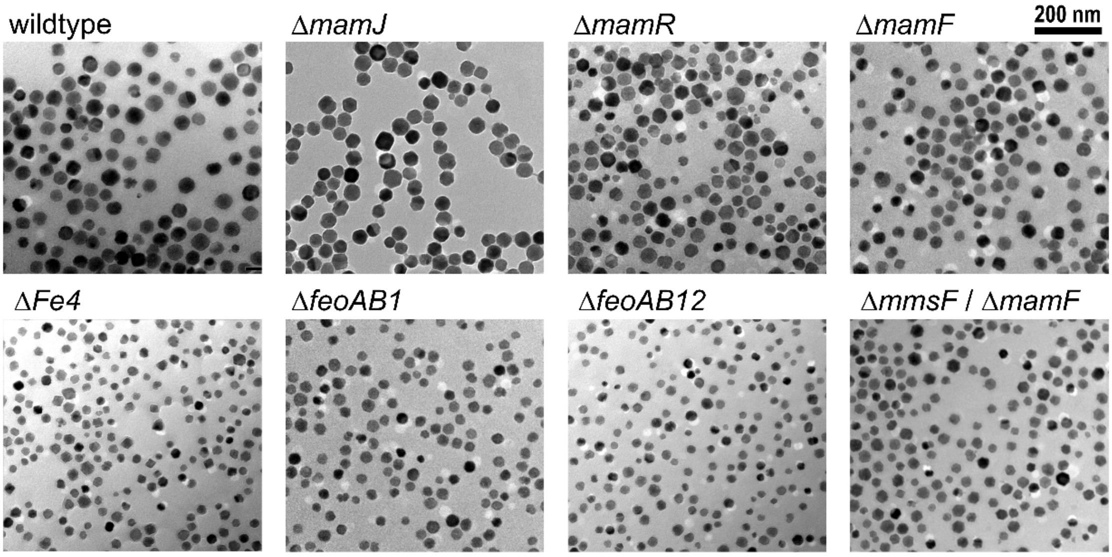

Figure 26. Transmission electron microscopy (TEM) micrographs of cell magnetosome morphologies observed with the generated deletion mutants used for this study. Particles were isolated from the respective strains and sterile filtrated to remove bacterial contamination. The resulting suspensions were free of impurities and contained well-dispersed particles. Scale bar 200 nm.

3.5. MPS and MPI efficacy of magnetosome strains

The magnetosome strains are characterized using our custom MPS system (Thieben et al., 2023), where samples with 10 µl containing 2 mgFe/ml are excited with a 20 mT/µ0 drive field at 26.042 kHz. For reference, a 10µl-sample of preclinical MPI tracer Perimag® (Micromod Partikeltechnologie, Rostock, Germany) (~19 nm core diameter) containing the same iron concentration is used. The MPS data of all magnetosome strains and Perimag® is evaluated in the time domain, and the results are additionally categorized into 'promising' and 'non-promising' candidates according to their performance (see Fig.27A and 27B, respectively). The MPS signal response for both groups is symmetric; however, as the particle size increases, as in the case of Δ*mam*R, Δ*mam*J, Δ*mam*F, and Δ*mms*F/*mam*F, the loop starts to open up (Fig.27B), indicating the onset of coercivity with increasing particle size. Moreover, the MPS signal response provides a delayed maximum or more than one local maximum; this may be viewed as evidence for the presence of two types of particles and their aggregates in the sample, displaying a non-promising signal response. Δ*mamF* provides the strongest signal, more than 2 Am^2. However, this high magnetic moment for large core sizes only holds for one-dimensional excitation with high drive-field amplitude, but with non-promising behavior.

On the contrary, promising magnetosomes show an MPS signal response with a single amplitude and similar relaxation behavior as Perimag®, which indicates the superparamagnetic and single-domain magnetite nanoparticles. All mutant magnetosome samples exceed the amplitude of the reference Perimag®; however, wild-type magnetosomes with larger diameters exhibit the lowest signal of the investigated samples. Here, mutants Δ*feoAB12* and ΔFe4 exhibit stronger amplitudes, and from all studied strains, Δ*feoAB*1 shows the best MPS signal response with 2,99 times stronger signal amplitude than Perimag®.

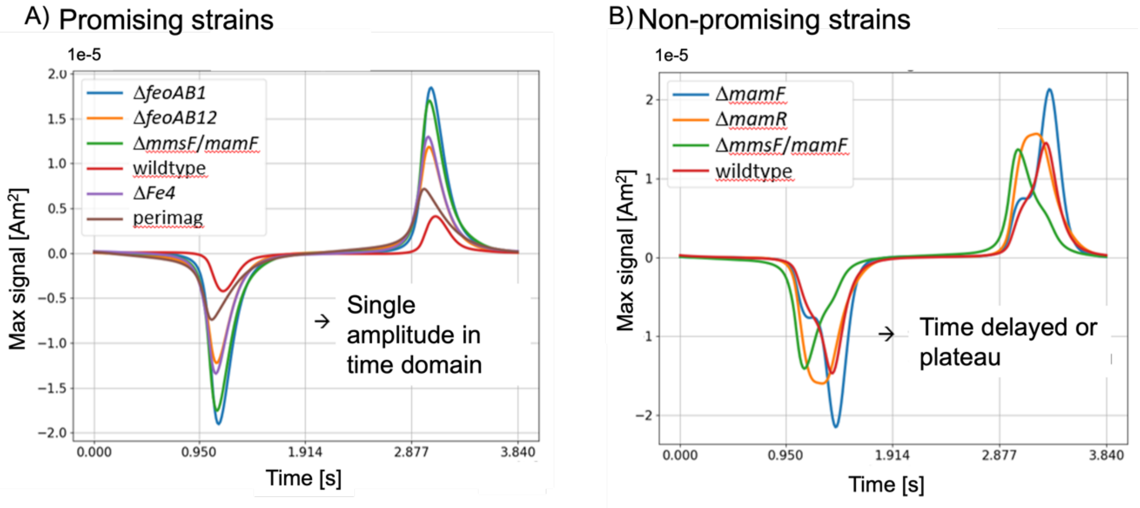

Figure 27. Δ*feoAB1* shows the finest magnetic moment compared to all the magnetosome strains. (A) Signal spectrum of the magnetic moment for promising magnetosomes and Perimag®. (B) Signal spectrum of the magnetic moment for non-promising magnetosomes. tMPS measurements (f_0 = 26.042 kHz, H_{max} = 20 mT/μ_0) are expressed in time domain signals.

3.6. Magnetization measurements of selected Δ*feoAB1* magnetosome strain

To demonstrate the particle stability and the signal dependence on the quantity of particles, in Fig.28A we measured the signal spectrum containing higher odd harmonics for a wide range of Δ*feoAB1* dilutions (from 1.1 to 35.7 mM of iron).

Several odd harmonics can be observed, and the spectrum shows linearity and parallel concentration-response curves; the MPS linear dependence is increased accordingly to a higher concentration of Δ*feoAB*1 because the amplitude of the harmonics is strongly dependent on the number of particles. The plateau at higher concentrations and the weaker dynamic responses between the magnetic moment of the high harmonics are due to MNP interactions. Therefore, the particles lose their freedom to rotate and consequently, lower harmonic amplitudes are expected indicating a saturation effect. The harmonic amplitudes for different driving-field amplitudes are shown in Fig.28B. Between these drive-field amplitudes, the dependence of higher harmonic magnitude on magnetic field strength shows linearity and the harmonics exhibit a similar pattern. The magnetization curve shows non-saturation at field strengths of 20 mT, referring to significant magnetic moments that provide high MPS amplitudes, a prerequisite for a good resolution for MPI.

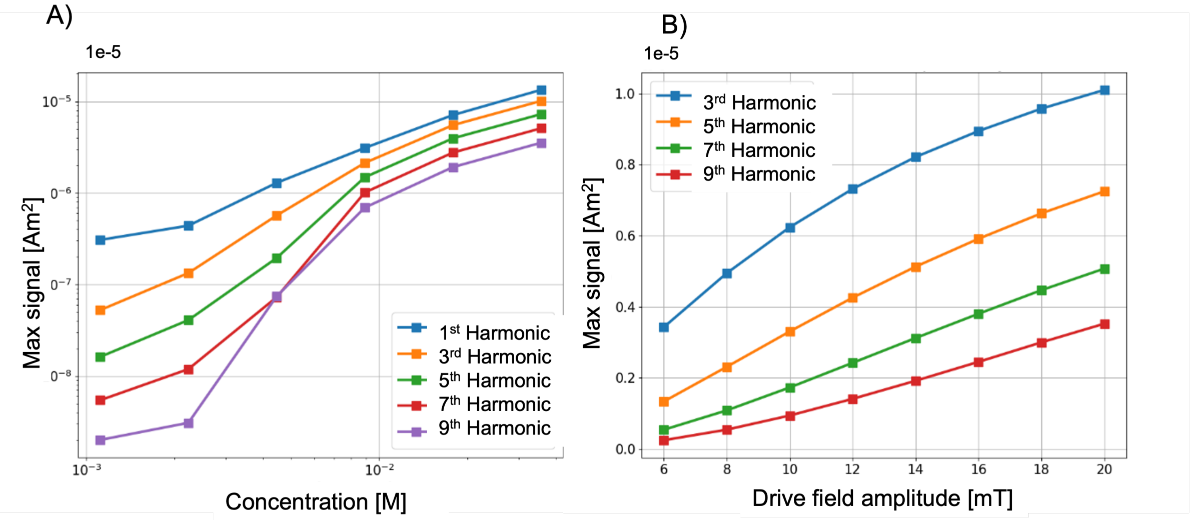

Figure 28. The magnetic response of all higher harmonics of Δ*feoAB1* shows linearity with different concentrations versus drive field amplitude. (A). Signal spectrum of higher odd harmonics for a concentration range (from 1.1 to 35.7 mM of iron of Δ*feoAB*1)**.** This experiment explores the effect of varying the Δ*feo*AB1 quantities in the assay with dilutions from 1.1 to 35.7 mM iron and their response profile (magnetic moment in Am^2) for the detection of linearity. (B). Field-dependent measurements from the third harmonic to the ninth are plotted versus drive field amplitude from 6 to 20 mT in a dilution series from 1.1 mM to 35.7 mM. A calibrated magnetic particle spectrometer (MPS) performs reference measurements f0 = 26.042 kHz, Hmax = 20 mT/µ0).

3.6.1. MPI system matrix and SNR analysis of *ΔfeoAB1* magnetosome strain

To date, a system matrix (SM) represents the mapping of the spatial concentration and the induced voltage signal that disassembles the deviation of the magnetic fields and the particle signal at each spatial position within the scanner. In the present work, the structure of the 2D system matrix is explored with 12 mT/µ0, a maximum gradient strength of 2 T/m, and 100 average in terms of MPI imaging. In Fig.29, the SNR profiles of the X (29A), Y (29B), and Z (29C) directions provide a quantitative comparison of the system matrices of *ΔfeoAB1* compared to Perimag®, with a concentration of 2 mg/ml over all frequencies (Hz). The behavior is similar for all three receive coils and provides higher SNR than Perimag® by a factor from 1.3 in the x-direction, to 2.1 in the y-direction. Therefore, we determined the full potential of *ΔfeoAB*1 resolution with increasing frequency for MPI image reconstruction compared to Perimag®.

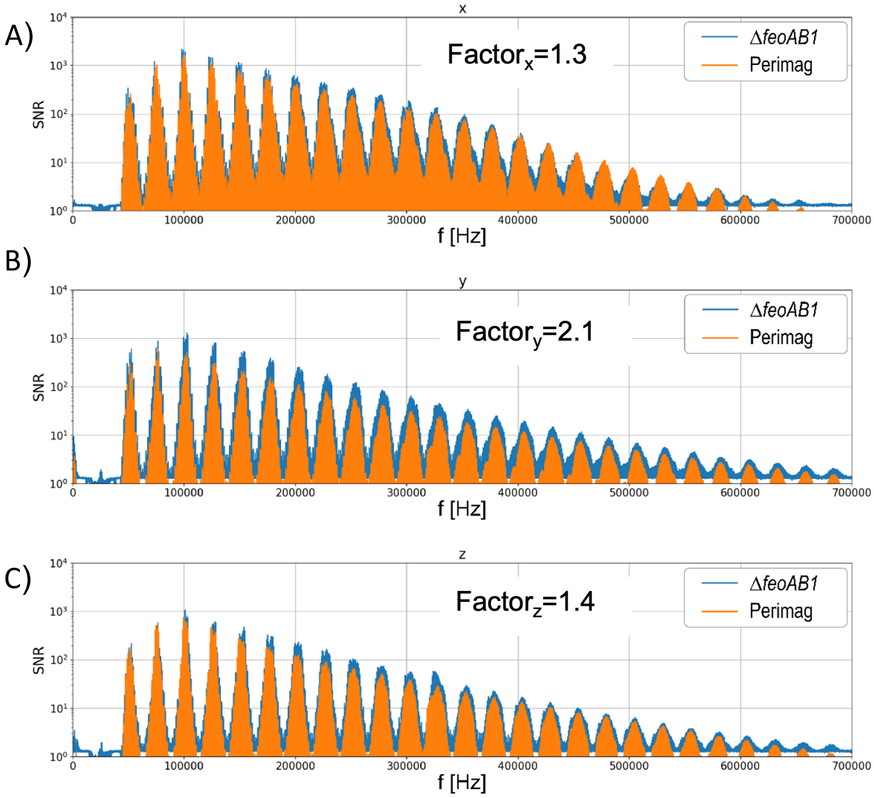

Figure 29. *ΔfeoAB1* shows higher SNR compared to Perimag® in the X-, Y-, and Z directions. The variance structure of the SNR for *ΔfeoAB1* with a concentration of 2 mg/ml, 12 mT/µ0, a maximum gradient strength of 2 T/m, and 100 average is visualized individually for each receive coil in the X (A), Y (B), and Z (C) directions with respect to the frequency (Hz).

3.6.2. Evaluation of *ΔfeoAB1* magnetosome with the "Open 3D Static Resolution Phantom" on MPI

To demonstrate that *ΔfeoAB1* findings from the MPS and system matrix resulted in a good MPI tracer, we performed an open 3D static resolution phantom measurement of 2mg *ΔfeoAB1*/ml with a 12 mT/μ_0, a maximum gradient strength of 2 T/m and 100 averages. The reconstructed images, as the profile phantom, are shown in Fig.30. The resolution phantom is formed by five tubes that share a common origin but extend at different angles in the x-,y- and z- directions. By selecting different planes, the resolution can be assessed with the distance between the tubes. The signal intensity between all planes can be observed in the profile of the three directions (Fig.30C). The distance between arms can be resolved in the xy- and zy-planes. The identification of the upper and the right arm cannot be clearly determined in the xz-plane. The lower resolution in the xz-plane can be explained by the lower SNR profile found in the previous results for the x- and z-direction compared to the y-direction. Nonetheless, at a *ΔfeoAB1* concentration of 2 mg/ml, the resolution in the x-, y-, and z- directions remained below 5 mm.

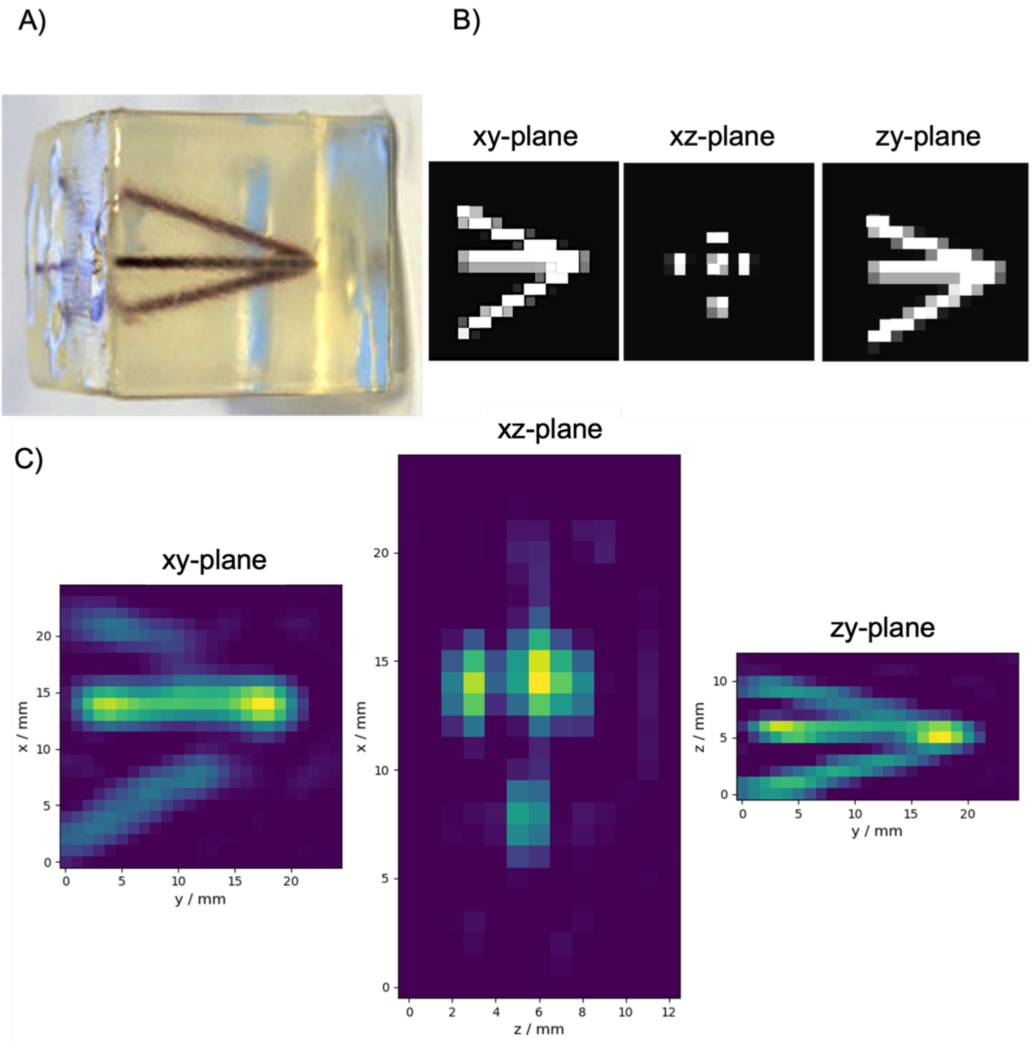

Figure 30. Picture and scheme of 3D static resolution phantom and imaging reconstruction results for ∆*feoAB1* magnetosomes. A) Photograph of the 3D Static resolution phantom (https://github.com/MagneticParticleImaging/OpenMPIData.jl). It is composed of 5 tubes that have a common origin on one side of the phantom. From there, the tubes extended at an angle of 10 and 15 degrees in the YZ plane and 20 and 30 degrees in the XY plane. B) CAD model of the phantom as a reference. C) Image reconstruction results of the 3D phantom. The five tubes were filled with ∆*feoAB1* with a 2 mg/ml concentration. The reconstruction images show the five tubes.

4. Discussion

4.1. Engineered Nanomag®/Synomag®-D nanoparticles with thrombolytic Amediplase for magnetic targeted drug delivery in ischemic stroke

Stroke remains a leading cause of mortality and long-term disability globally, with approximately 15 million cases annually, 50% of which result in death, according to the Global Burden of Disease (GBD) 2019 estimates (GBD 2019 Stroke Collaborators, 2021). Given that, every minute during a stroke results in the loss of 1.9 million neurons (Saver, 2006), the timing of diagnosis and intervention is critical. Magnetic Particle Imaging (MPI) offers a promising avenue for improving both diagnosis and therapeutic outcomes for cerebrovascular diseases, especially through targeted drug delivery. The current study demonstrates the potential of conjugating superparamagnetic Nanomag®/Synomag®-D nanoparticles with recombinant plasminogen Amediplase for stroke therapy. The ED-Carbodiimide-mediated conjugation of Amediplase with these nanoparticles significantly reduced clot lysis time by 75% in an *in vitro* clot lysis model. This reduction could correspond to the preservation of up to 60 million neurons, 414 billion synapses, and 360 km of axonal fibers, offering a major improvement in clinical outcomes (Saver, 2006). Moreover, the drug delivery system would enable lower therapeutic dosages, reducing side effects while enhancing drug concentrations at the target site, and accelerating blood flow restoration. Hence, this confirms the exciting potential of MPI not only for ischemic stroke diagnosis but also as a targeted therapeutic approach.

The idea of exploring targeted thrombolysis efficiency using drug-loaded magnetic nanoscale particles can be tracked back to the late 1970s. Widder et al. employed magnetically responsive microspheres to deliver anti-tumor drugs (Widder, Senyei, & Ranney, 1979; Widder, Senyel, & Scarpelli, 1978). Although magnetic targeting has been successful in several studies, only a few clinical trials have been conducted, with the evidence of promising targeted therapy in cancer and beyond. A clinical trial on 32 patients with hepatocellular carcinoma was performed by Koda et al., (2002). This study supplemented doxorubicin hydrochloride to a magnetic particle carrier and delivered by sub-selective hepatic artery catheterization. The particle drug complex was targeted to the tumor site using an external magnetic field (500 mT) and examined with MRI. Of the 32 studied patients, tumors were successfully targeted in 30. A study by Y. Inada et al. found that the urokinase-coupled magnetic modifier could target the fibrin gel by applying magnetic force and achieving local fibrinolysis in a petri dish (Inada et al., 1987).

A careful evaluation to ensure the correct dosage and distribution of coated particles is crucial. We must consider that the standard dose of thrombolytic drugs varies depending on the medication used and the condition being treated. In the case of Alteplase, the standard dose for ischemic stroke is 0.9 mg per kilogram of body weight, up to a maximum dose of 90 mg administered intravenously over one hour (Wardlaw, Zoppo, Yamaguchi, & Berge, 2003). Different types of recombinant thrombolytic enzymes have been studied to demonstrate the potential of using conjugated magnetic nanoparticles for improved thrombolysis. A study from 2010 immobilized two thrombolytic enzymes, Nattokinase (NK) and Lumbrokinase (LK), onto magnetic nanoparticles and resulted in much higher thrombolytic activity than pure enzymes (Ren, Wang, Wu, Shang, & Wang, 2010). An exciting study validated the conjugation of tPA and streptokinase with silica-coated MNP, which resulted in a 38% reduction in magnetic targeted clot lysis time compared to those without magnetic guidance (Tadayon, Jamshidi, & Esmaeili, 2015). In a previous study using effective rt-PA conjugated to magnetic nanocarriers under identical conditions to our experiments, 62 µg of effective rt-PA, required 11 minutes to restore the flow (Yang et al., 2012). In contrast, in the current study, the average reperfusion time was shortened by around 5 minutes (n=5) with Amediplase. This accelerated thrombolysis may be conferred to the more effective Amediplase on the particles and its better clot penetration. In all cases, surface functionalized particles need to meet standards for clinical translation with rigorous testing and approval processes.

This novel nanoparticle and nanoconjugate technology for therapeutics and targeting are emerging for cerebrovascular diseases. Surface functionalized MNP promotes personalized medicine approaches that enhance the outcomes of diseases such as brain cancer (Hao, Chen, & Wu, 2021). A strong interaction between the surface particles and the biomolecule is required to control the local therapy and prevent the release of these molecules during the navigation of the particles. The immobilization of proteins to the nanoparticle surfaces through a covalent binding offers higher stability due to their inflexible conformation. Multiple diverse types of nanoparticles conjugated with thrombolytic agents have been developed, such as silica-coated nanoparticles (SiO2-MNP) (J.-P. Chen, Yang, Ma, Tu, & Lu, 2012), polymeric nano-constructs (tPA-DPNs) (Colasuonno et al., 2018), and gold nanoparticles (tPA/AuNP) (Tang et al., 2015). Modifying the chemical groups onto the surface particle through organic linkers provides many opportunities to immobilize biomolecules. In this study, Nanomag®/Synomag®-D nanoparticles were selected because of their superior functionalization potential. The immobilization strategy with EDC has extensive use in the functionalization of biomolecules due to its robustness and minimal need for chemical modifications. This approach ensured the stability of the thrombolytic protein during circulation and maximized its efficacy at the clot site. Given the immobilization strategy via the surface-exposed amine group of the thrombolytic proteins, a homogenous distribution of the immobilized proteins on the nanoparticles' surface would be expected. However, the differences in Actilyse® and Amediplase conjugation rates raise questions about the site-specific accessibility of the immobilized proteins and their steric hindrance. We suggest that Actilyse® (70 kDa) hinders other Actilyse's accessibility, which may be reduced due to a steric effect because its coupling requires more surface area than Amediplase (49 kDa). Furthermore, the pertinent protein-protein interactions that affect the orientation and integrity of these proteases could play a role. Many other choices exist for coating magnetic particles to diversify the surface properties (Grüttner, Rudershausen, & Teller, 2001; Mateo et al., 2003; Tural, Tural, Ertaş, Yalınkılıç, & Demir, 2013).

In addition to any chemistry surface modifications, the nature of the particles' coating must be considered to improve biocompatibility and biodistribution, as well as for additional functionalization and applications. Uncoated SPIONs have low solubility and high agglomeration rates under physiological conditions, leading to harmful biodistribution. The size, charge, and coating favor the blood circulation time, stabilization, and dispersion of the particles, providing better conditions for functionalization. Thus, the potentially toxic components can be limited from being released within the body (Berry & Curtis, 2003). For example, due to their longer half-life and commercial availability, dextran-coated magnetic nanoparticles have been studied for biomedical applications in cancer treatment and MRI (Chertok et al., 2008; Hong et al., 2008). Moreover, the particle size is a crucial factor for the interaction and the biodistribution of the particles within the body (Shubayev, Pisanic, & Jin, 2009). Small particles less than 10 nm in hydrodynamic diameter are eliminated through renal clearance. The spleen, liver, and lungs capture particles more significant than 100 nm in size (Feng et al., 2018). Multiple articles have confirmed primarily *in vitro* low toxicity or cytotoxicity associated with different surface-coated SPIONs (Jeng & Swanson, 2006; Karlsson, Gustafsson, Cronholm, & Möller, 2009; Kim et al., 2006), until high exposure levels, 100 µg of particles per ml (Ankamwar et al., 2010). However, these studies about their low toxicity in humankind are very conditioned. SPIONs are intravenously administered, and the iron dosage concentration constitutes 1.25% of the total body iron stores (Elias & Tsourkas, 2009). Nevertheless, SPIONs are magnetically targeted to specific parts of the body/organ to accomplish the diagnosis or the therapeutic applications, where they accumulate in high concentrations. As a result, the excessive free iron exposed with the extra SPIONs storage in the targeted tissue can have toxic implications and homeostatic imbalance with cytotoxic responses (Ankamwar et al., 2010; Veranth, Kaser, Veranth, Koch, & Yost, 2007). Indeed, the exposure of SPIONs with the absence of cytotoxicity can still induce DNA, proteins, and lipids peroxidation by the generation of reactive oxygen species (ROS). The reaction of the free ferrous ions with the mitochondrial hydrogen peroxide may lead to carcinogenesis (Stevens, Jones, Micozzi, & Taylor, 1988; Valko et al., 2007). The gap in the toxicity evaluation studies is a major concern to establish safety limits for the practical and clinical use of MPN. Consequently, an extensive number of *in vitro* and *in vivo* studies must be conducted to achieve effective results.

Effective treatment of ischemic stroke requires the delivery of the conjugated SPIONs to the brain. Therefore, they must cross the blood-brain barrier (BBB) in significant therapeutic amounts. The responsiveness of MNP to an external magnetic field increases their capacity to deliver the particles in the CNS crossing the intact BBB with no apparent toxicity in a mouse model (Kong et al., 2012). It has been shown that MPI is a relevant diagnostic tool for ischemic stroke (Ludewig et al., 2017), and we expect that MPI will offer the potential to improve stroke treatment with the systemic administration of drug-coated particles and their guidance to the target point. Translating these preclinical studies to clinical practice requires rigorous safety assessments, optimization of targeting strategies, and scalable production techniques.

4.2. Characterization of genetically engineered magnetosomes as tailored MPI

Chemical synthesis of magnetic nanoparticles addresses many challenges in practical applications due to the complex reaction process in controlling the magnetite structure, particle size, and distribution (Ziemian et al., 2018). It has been shown that the different synthesis paths of magnetic nanoparticles significantly enhanced their magnetic moment and MPI signal resolution (Eberbeck, Wiekhorst, Wagner, & Trahms, 2011; Kratz et al., 2018). In the current work, we extend the synthesis of superparamagnetic magnetosomes as highly promising for producing tailored MPI tracers with biomineralized iron nanoparticles from magnetotactic bacteria.

Magnetosomes are mineralized under strict genetic control resulted in precise magnetic crystal structure and size. However, magnetosomes require prior adjustments to better fulfill their biomedical applications. The common modification strategies include the genetic manipulation with pre-designed functional expression, which enables the control of the magnetosome biosynthesis to meet personalized requirements. We have reported the production of these eight magnetosome variants with different sizes and shapes (Thieben et al., 2023). The magnetite synthesis initiation was not affected by the absence of the Fe4, *feoAB1*, *feoAB12*, *mamR*, *mamJ*, *mmsF* and *mmsf/mamF* genes. Nevertheless, the crystal growth was stalled indicating that they are most likely required for crystal maturation. Consequently, during the synthesis and isolation process, polydisperse particles were found due to the lack of maturation development. Regardless of these results, the magnetosome mutants still qualify for MPI critical parameters, including the size and shape of the magnetite core (Bauer et al., 2015; Rosenfeldt et al., 2021; Tomitaka et al., 2015). It has been shown that the deletion of *mamR*, *mamJ*, and *mam*F genes can display a critical role in the magnetite size, producing superparamagnetic particles with mean single core sizes from 30 to 38 nm (Scheffel et al., 2008). The genome of M. *gryphiswaldense* also encodes for the *feoAB* operon, which is part of the *feo*-system. It is composed of the *feoA* and *feoB* proteins with an accessory role in the ferrous iron transport during the magnetite formation. It has been confirmed that Δ*feoAB* mutant cells develop smaller number of magnetosomes and smaller size, between 20-30 nm, compared to the wild-type M*. gryphiswaldense* (Rong et al., 2008). Additionally, we produced a Δ*feoAB12* double mutant by deleting the *feoAB2* gene from the Δ*feoAB1* strain by using a *galK*-base counterselection method (Raschdorf et al., 2014). ΔFe4 has a mutation in the iron uptake genes, which has previously been shown to magnetite core size around 28 nm (Kumari et al., 2014).

Using MPS as a reliable tool to identify promising magnetosome types, our eight magnetosome variants presented high magnetization signal response in time domain. Moreover, all magnetosome results overcame the signal response of Perimag®, pointing to a significantly high effective magnetic moment of the magnetosome strains. This a fundamental characteristic for sensitivity and spatial MPI resolution, strongly influenced by the magnetic properties of the tracer (J. Weizenecker, Borgert, & Gleich, 2007). In this study, Δ*feoAB1* magnetosome strain was identified as the perfect candidate for MPI tracer. The Δ*feoAB1* time-domain amplitude is a factor of 2.99 higher compared to Perimag®, correlated with a perfect core size of 28 nm (Dhavalikar & Rinaldi, 2014). Heinke et al., (2017) also investigated the structure and the magnetic properties of magnetosomes extracted from *Magnetospirillum gryphiswaldense* and various mutants as promising candidates for MPI tracers. They resulted in a better MPS performance than Resovit, another gold standard MPI tracer, except for one mutant due to its large particle size. Further, our results imply a significant improvement in higher spatial resolution with the identification of more harmonics, as shown by Rahmer et al., (2009). Here, we demonstrate that Δ*feoAB1* magnetosome quality is drastically improved in image reconstruction approaches compared to Perimag®. The 3D system matrix results demonstrated the MPI exposure of Δ*feoAB1* mutants with good temporal and spatial resolution. The reconstructed images of Δ*feoAB1* magnetosomes showed efficient spatial resolution for the x- and y- directions. However, the lower resolution in the xz-plane can be interpreted by the lower gradient in the z-direction. The introduction of a second-drive field coil with field generation in the z-direction would be a key improvement (Graeser et al., 2019). Nevertheless, this work constitutes a significant advancement in the local characterization of genetically engineered magnetosomes by using MPS.

Compared to chemically synthesized nanoparticles, magnetosomes are naturally coated with the magnetosome membrane. The magnetosome's membrane surface is negatively charged, preventing particle aggregation and avoiding direct contact between the magnetic core and the organism. Alternatively, this lipid bilayer structure contains proteins that stabilize the magnetic mineral, being unnecessary to cover them with dextran or PEG molecules. Moreover, magnetosome's membrane has the potential for the conjugation with specific targeting molecules due to the abundant amine groups on their surface. Chemical modification strategies can EDC-crosslink the amine groups with carboxyl groups, as it has been developed in our previous study for the conjugation of Amediplase to MNP. For example, Sun et al., (2008) EDC-immobilized the anti-tumor Adriamycin onto a magnetosome membrane satisfactorily. Thus, the potential of conjugating magnetosomes for MPI imaging and targeted therapy could be enhanced. To illustrate, Pi et al. (2017) developed an immuno-magnetosome by binding an AFB_1 polyclonal antibody onto the natural magnetosome. The study resulted in a 28-fold capability on AFB_1 toxins collection compared to AFB_1 antibody functionalized conventional Fe_3O_4 magnetic nanoparticles in vegetable oil.

The remarkable potential of magnetosomes in biomedical applications demands a rigorous evaluation of their safety. Nevertheless, there has been a notable absence of detailed studies examining their toxicity. Mickoleit et al., (2021) Demonstrated the biocompatibility of isolated magnetosomes with slight cell proliferation with magnetosome incubation in different cancer cell lines and primary cells with invariable viability. Since magnetosomes are derived from bacteria, the endotoxin concentration at the magnetosome membrane might be higher than tolerated for human applications. Thus, the possibility of magnetosomes-based in clinical studies requires more biocompatibility and toxicity evaluations. Nonetheless, magnetosomes have exhibited significant potential for application in MRI. Several multifunctional contrast agents based on magnetosomes have been formulated for the real-time assessment of tumor therapies. Y. Zhang et al., (2019) performed targeted MRI using magnetosomes as contrast agents to target tumors that overexpress human epidermal growth factor receptor 2 (HER2). The magnetic response of magnetosomes and their application to hyperthermia treatments has been discussed continually due to their magnetic properties and the possibility of chemically modifying their surface properties to address lower toxicity in clinical applications (E. Alphandéry et al., 2011; Edouard Alphandéry, Guyot, & Chebbi, 2012; Le Fèvre et al., 2017; Plan Sangnier et al., 2018; Timko et al., 2009).

Despite the extensive research on magnetosome biomineralization, isolation methods and the composition of the membrane, their biomedical applications are still in their early developmental phase. The limited investigation of their functional designs could be the main reason. Furthermore, the stringent nutritional and environmental conditions for magnetosome artificial cultivation result in a real challenge for large-scale production. Magnetotactic bacteria are widely distributed in nature, however the production of magnetosomes on a large scale has become a considerable impediment. Today, the cultivation and the large-scale production of magnetotactic bacteria with better performance are critical points in magnetosome research. Since Blakemore et al. first proposed the large-scale culture method of *Magneto-spirillum Magnetotacticum* MS-1 in 1979, Heyen & Schüler reported the production of 6.1 mg/l per day by culturing *Magnetospirillum Gryphiwaldense* at 25 mbar pO2 in 2003. The technical requirements and economic factors for magnetosome production from magnetotactic bacteria have been studied within the following contexts. Chemical synthesized magnetite costs in a single-stage fed-batch and a semicontinuous process about 10,372 USD per kilogram. However, magnetosome production from magnetotactic bacteria, depending on the production process variation, has a selling price ranging between 21 and 120 USD per gram (Correa, Presciliano, & Abreu, 2021). These costs are consistently below commercial synthetic nanoparticle production expenses, making magnetosomes an attractive alternative for cheaper and greener magnetic nanoparticle manufacturing.

The ongoing evolution of molecular manipulation technologies has sparked considerable attention towards the molecular modification of magnetosomes. Although broader studies of different magnetic nanoparticles would aid the finding of the perfect MPI tracer, our results support an easy and quick method of assessing the efficiency of new materials such as magnetosomes, for magnetic particle imaging. Such innovations are anticipated to significantly contribute to the evolution of precision medicine in the future.

4.3. Perspectives

MPI is an emerging imaging modality that offers real-time, high-contrast visualization of superparamagnetic iron oxide nanoparticles without ionizing radiation. The introduction of a mobile MPI scanner into stroke care has the potential to revolutionize the management pathway from the prehospital setting through targeted therapy. In the prehospital phase, a compact and rapidly deployable MPI system could detect cerebral vascular occlusions in ambulances or mobile stroke units, thereby facilitating early diagnosis and guiding immediate transport decisions. Upon hospital arrival, a bedside MPI scanner would enable continuous monitoring of thrombus burden and tissue perfusion without relocating the patient, minimizing time delays and preventing potential complications associated with patient transfers. Furthermore, the direct tracking capabilities of MPI could be exploited to steer functionalized nanoparticles conjugated with recombinant tissue plasminogen activator (rt-PA) to the site of occlusion. This targeted delivery might enhance thrombolytic efficacy while limiting systemic exposure to rt-PA, thereby reducing the risk of hemorrhagic complications. By combining sensitive, point-of-care imaging with magnetic steering of therapeutic nanoparticles, mobile MPI scanners could streamline acute stroke management, improve thrombus resolution, and potentially reduce secondary injury. These benefits collectively highlight the transformative potential of mobile MPI in accelerating diagnosis, optimizing targeted drug delivery, and enabling individualized bedside treatment for stroke patients.

The seeking of optimal tracers for MPI undergoes the development and synthesis of superparamagnetic nanostructures by eukaryote cells; the assimilation of magnetic nanoparticle synthesis into mammalian cells creates a cytocompatible alternative to the exogenous administration of MNP. An alternative approach to magnetize mammalian cells would involve *de novo* synthesis of intracellular superparamagnetic nanostructures by introducing a magnetosome genetic material. For example, the *mms6 gene* promotes the formation of isomorphic superparamagnetic magnetite nanocrystals and helps in the maturation of its morphology. The transfection of recombinant *mms6* gene from *Magnetospirillum magneticum* AMB-1 into mesenchymal stem cells facilitated their ability to bio-assimilate the synthesis of intracytoplasmic magnetic nanoparticles (Elfick et al., 2017). Other groups investigated that the *magA* gene fragment alone was sufficient to produce magnetic nanoparticle tracers for MRI in HEK-293T cells (Zurkiya, Chan, & Hu, 2008). Based on these publications, we investigated the *de novo* synthesis of magnetic nanostructures by the stable transfection of *mms6* and *magA* genes in HEK-293T cells with PEI without success. Our results suggested that *mms6* and *magA* were toxic to the HEK-293T cells, leading them to death. Another approach was cloning *mms6* and *magA* genes into lentiviral vectors LeGo-iC2 and LeGo-iG2, kindly provided by Dr. rer. nat Kristoffer Riecken (supplementary Fig.1 and 2, respectively). This method is based on established methods of lentiviral vector production and titration from Dr. rer. nat. Kristoffer Riecken and Prof. Dr.rer.nat. Dipl.-med Boris Fehse (Weber, 2007). *Mms6* and *magA* viral production, titration, and transduction onto HEK-293T cells were successfully performed together with Dr. rer. nat Kristoffer Riecken (supplementary information Fig.3 and Fig.4, respectively).

One more access was the genetic control of the iron uptake and storage in mammalian cells facilitating their magnetic actuation. To achieve this goal, HEK-293-6E cells were genetically manipulated to increase intracellular iron content and organize the excess of iron in a non-toxic but highly magnetic form. The ferrous iron transporter ZIP14 was evaluated together with the heavy chain ferritin (hFT) for the induction of magnetic biomineralization based on Massner (2018). ZIP14, and hFT were successfully transiently co-overexpressed onto HEK-293-6E with PEI (supplementary information Fig.5). To trigger magnetic biomineralization, we investigated different iron sources without success.

Cellular therapies are emerging as effective treatments. MRI has been generally used for *in vivo* cell tracking; however, MPI can address many of the limitations of MRI. MPI would be non-invasive, non-ionizing, and overly sensitive to detect a quantitative magnetic cell number. Improvements in MPI tracer and cellular sensitivity are expected to improve uptake strategies that may help detect flow cell numbers. Cell tracking with MPI will provide an understanding of many diseases and cellular therapies to guide therapeutic optimizations. These results may provide exciting avenues for further investigation.

5. Abstract

Magnetic Particle Imaging (MPI), introduced in 2005, is a novel, radiation-free imaging modality with high sensitivity and the ability to provide quantitative tracer signals without interference from tissues or bones. MPI's unique features, including its capability for magnetic navigation and functional imaging, make it a promising tool for various medical applications.

This thesis explores the potential of MPI in accelerating and improving the diagnosis and treatment of ischemic stroke, by immobilizing magnetic nanoparticles with thrombolytic agents, enabling precise delivery to the infarct core. Further, the research investigates the development of tailored MPI tracers to enhance imaging potential. The production and characterization of recombinant thrombolytic proteins, SBP-Amediplase and avi-Amediplase, using the HEK-293-6E cell expression system was successfully achieved. Amediplase and Actilyse® were effectively conjugated to magnetic nanoparticles via ED-Carbodiimide crosslinking, resulting in significantly enhanced binding capacity and thrombolytic activity. *In vitro* studies showed that Amediplase-conjugated nanoparticles exhibited 75% accelerated clot lysis under a magnetic field, indicating the potential of magnetically targeted thrombolysis in MPI. Seven genetically engineered variants of magnetosomes, biogenic nanoparticles synthesized by magnetotactic bacteria, with different morphological and magnetic properties, were evaluated as promising MPI tracers. The results categorize magnetosomes into promising and non-promising candidates based on their magnetic particle spectrometer (MPS) signal responses. ∆*feo*AB1, ∆*feo*AB12, and ∆Fe4, exhibit high signal amplitudes. Notably, ∆*feo*AB1 shows the strongest signal, with a 2.99-fold increase over Perimag®, and the stability and concentration-dependent signal, with significant magnetic moments, essential for MPI high-resolution. Additionally, the study explores the 3D system matrix for MPI imaging, which resulted in a higher signal-noise-to-ratio of ∆*feo*AB1 compared to Perimag®, indicating its superior potential for MPI image reconstruction. In conclusion, this research demonstrates the feasibility and effectiveness of MPI for targeted stroke therapy and highlights the importance of developing specialized tracers and thrombolytic agents for enhanced imaging and treatment outcomes.

6. Zusammenfassung

Magnetpartikel-Bildgebung (MPI), eingeführt im Jahr 2005, ist eine neuartige, strahlungsfreie Bildgebungsmethode mit hoher Empfindlichkeit und der Fähigkeit, quantitative Tracersignale ohne Interferenzen durch Gewebe oder Knochen zu liefern. Die einzigartigen Eigenschaften von MPI, einschließlich der Fähigkeit zur magnetischen Navigation und funktionellen Bildgebung, machen es zu einem vielversprechenden Werkzeug für verschiedene medizinische Anwendungen.

Diese Dissertation untersucht das Potenzial der MPI, die Diagnose und Behandlung ischämischer Schlaganfälle zu beschleunigen und zu verbessern. Dies erfolgt durch die Immobilisierung von mit Thrombolytika konjugierten magnetischen Nanopartikeln, wodurch eine präzise Abgabe an den Infarktkern ermöglicht wird.

Weiterhin wird in der vorliegenden Arbeit die Entwicklung maßgeschneiderter MPI-Tracer untersucht, um das Bildgebungspotenzial zu verbessern. Die Produktion und Charakterisierung der rekombinanten thrombolytischen Proteine SBP-Amediplase und Avi-Amediplase wurde unter Verwendung des HEK-293-6E-Zell-Expressionssystems erfolgreich durchgeführt. Amediplase und Actilyse® wurden über ED-Carbodiimid-Kupplung effektiv an magnetische Nanopartikel konjugiert, was zu einer signifikant verbesserten Bindungskapazität und thrombolytischen Aktivität führte. In-vitro- Studien zeigten, dass Amediplase-konjugierte Nanopartikel unter einem Magnetfeld eine um 75 % beschleunigte Gerinnselauflösung aufwiesen, was auf das Potenzial der magnetisch gezielten Thrombolyse der MPI hinweist. Sieben gentechnisch veränderte Varianten von Magnetosomen - biogenen Nanopartikeln, die von magnetotaktischen Bakterien synthetisiert werden - wurden als vielversprechende MPI-Tracer mit unterschiedlichen morphologischen und magnetischen Eigenschaften evaluiert. Die Ergebnisse kategorisierten Magnetosomen in vielversprechende und weniger vielversprechende Kandidaten, basierend auf ihren Signalantworten im Magnetpartikelspektrometer (MPS). Δ*feo*AB1, Δ*feo*AB12 und ΔFe4 zeigten hohe Signalamplituden. Es ist besonders hervorzuheben, dass Δ*feo*AB1 das stärkste Signal mit einer 2,99-fachen Erhöhung gegenüber Perimag® zeigte. Dieses konzentrationsabhängige Signal von Δ*feo*AB1 war stabil mit signifikanten magnetischen Momenten, die für eine hochauflösende MPI erforderlich sind. Darüber hinaus untersuchte die Studie die 3D-Systemmatrix für die MPI-Bildgebung, die zu einem höheren Signal-Rausch-Verhältnis von Δ*feo*AB1 im Vergleich zu Perimag® führte, und damit größeres Potenzial für die MPI-Bildrekonstruktion hat. Zusammenfassend zeigt diese Arbeit die Umsetzbarkeit und Wirksamkeit von MPI für die gezielte Schlaganfalltherapie und unterstreicht die Bedeutung der Entwicklung spezialisierter Tracer und Thrombolytika für verbesserte Bildgebungs- und Behandlungsergebnisse.

7. Abbreviations

A	Ampere
Arg	Arginine
BBB	Blood brain barrier
BCA	Bicinchoninic Acid Assay
CT	Computed tomography
Cys	Cysteine
DNA	Desoxyribonucleic acid
EDC	1-ethyl-3-(-3-dimethyilaminopropyl) carbodiimide hydrochloride
FFL	Field free Line
FFP	Field free Point
fMRI	Functional Magnetic resonance imaging
FoV	Field of view
HEK	Human embryonic kidney
His	Histidine
HRP	Horseradish peroxidase
Hz	Herzs
Ile	Isoleucine
kDa	Kilodalton
MACS	Magnetic activated cell sorting
m	meter
mam	magnetosome associated membrane
MIT	Magnetic imaging techniques
mms	magnetosome membrane specific
MNP	Magnetic Nanoparticles
MPI	Magnetic particle imaging
MPIN	Magnetic particle imaging and navigation
MPN	Magnetic particle navigation
MPS	magnetic particle spectrometer
MRI	Magnetic resonance imaging
MTB	Magnetotactic bacteria
NdFeB	Neodymium N52 magnets
Ni-NTA	Nickel Nitrilotriacetic acid
PBS	Phosphate-buffered saline
PCR	Polymerase chain reaction
PEG	Polyethylenglycol
PEI	Polyethyleneimine
PET	Positron Emission Tomography
pNAPEP	p-nitroaniline prolyl endopeptidase
rt-PA	recombinant tissue plasminogen activator
scu-PA	single-chain urokinase plasminogen activator
SBP	Streptavidin binding protein

SDS-PAGE	Sodium dodecyl sulphate polyacrylamide gel electrophoresis
SF	System Function
SM	System matrix
SNR	Signal noise to ratio
SPECT	Single Photon emission computed tomography
SPIONs	Super paramagnetic iron oxide nanoparticles
T	Tesla
TC	Curie Temperature
TEM	Transmission electron microscopy
U	Unit
US	Ultrasound
USD	United states dollars
WT	Wild type

8. Supplementary information

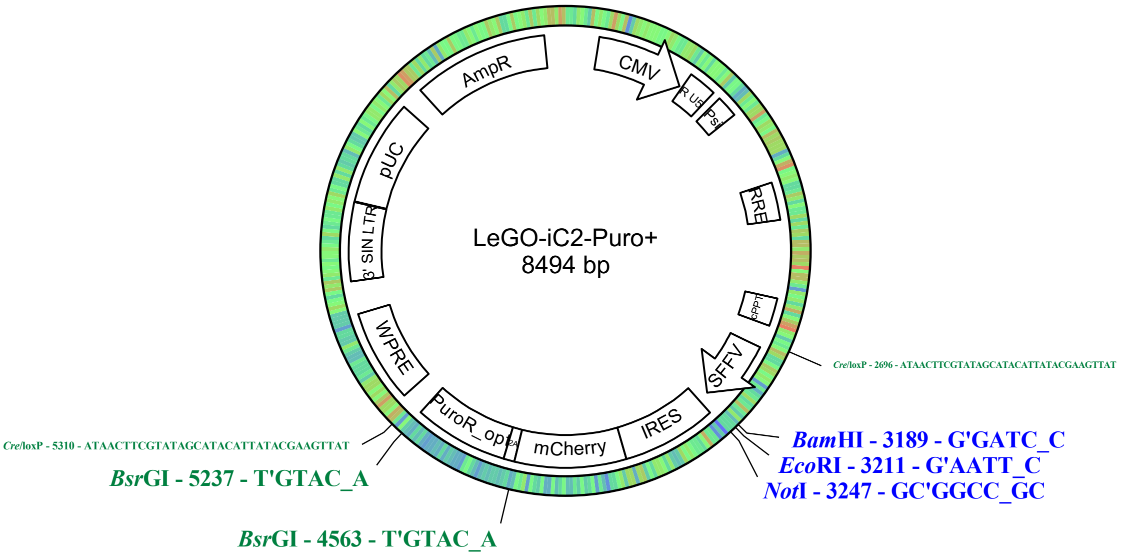

Supplementary Figure 1. Lentiviral Gene Ontology Vector, LeGO-iC2-Puro+. Kristoffer Riecken, Boris Fehse.

http://www.LentiGO-Vectors.de

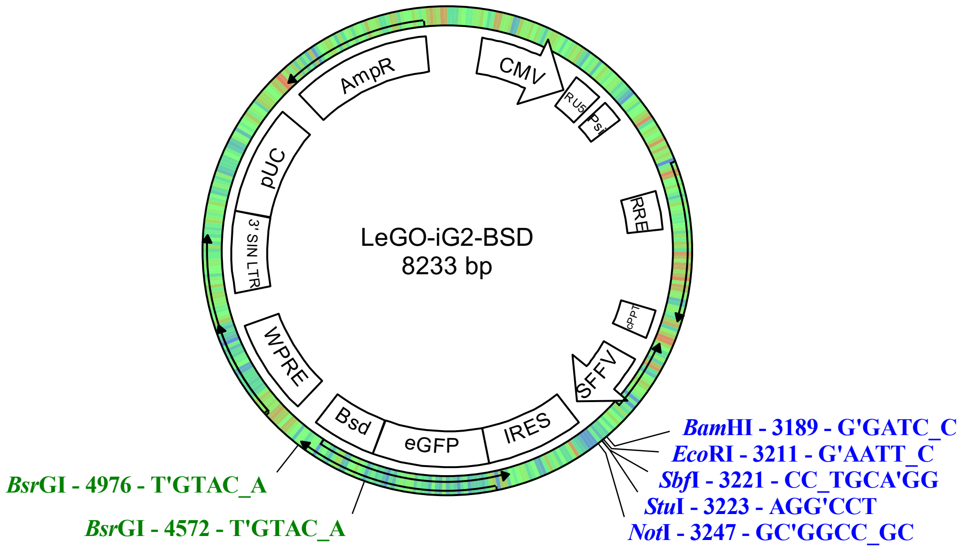

Supplementary Figure 2. Lentiviral Gene Ontology Vector, LeGO-iG2/BSD. Weber K, Mock U, Petrowitz B, Bartsch U, Fehse B. Lentiviral gene ontology (LeGO) vectors equipped with novel drug-selectable fluorescent proteins: new building blocks for cell marking and multi-gene analysis. Gene Ther. 2010 Apr; 17(4):511-20.

http://www.LentiGO-Vectors.de

1. LeGo iC2 mms6
2. LeGo iG2 mms6
3. LeGo iC2 magA
4. LeGo iG2 magA
5. LeGo iC2
6. LeGo iG2

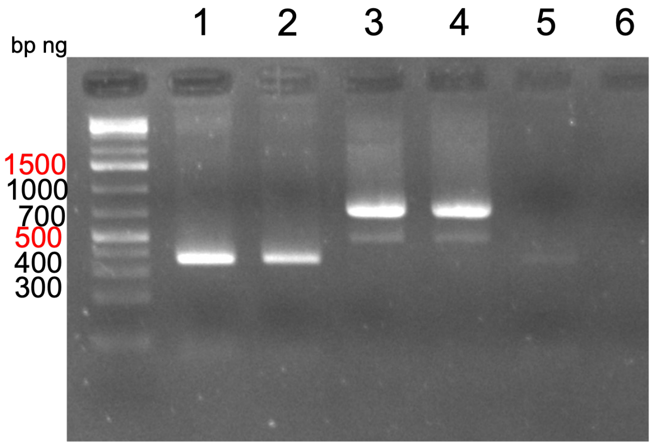

Supplementary figure 3. Genomic analysis of Lentiviral transduction of 1. LeGo iC2 mms6. 2. LeGo iG2 mms6. 3. LeGo iC2 magA. 4. LeGo iG2 magA. 5. LeGo iC2. 6. LeGo iG2 onto HEK-293-T cells.

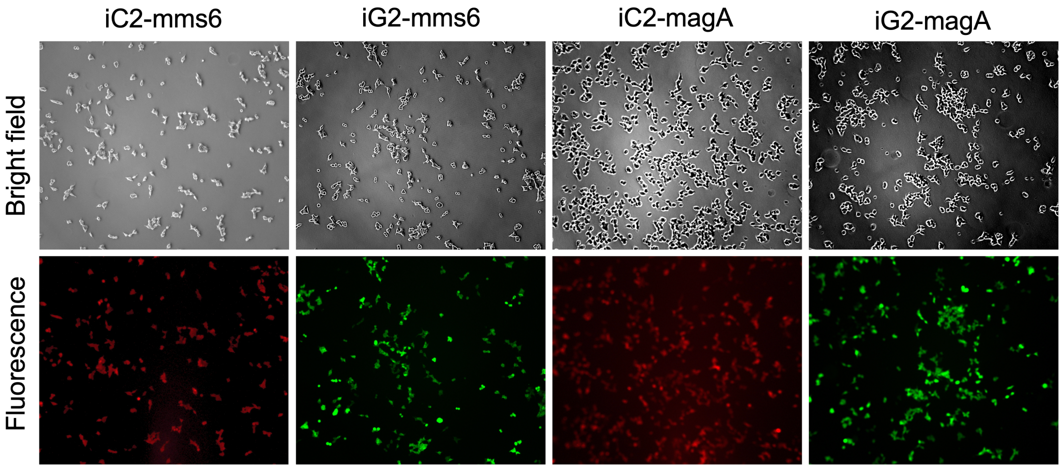

Supplementary figure 4. RGB marking of cultured HEK-293-T cells with lentiviral iC2 and iG2 and mms6 and magA magnetosome genes. RGB marking of HEK-293 T cells transduced with iC2-mms6, iG2-mms6, iC2-magA, and iG2-magA. Fluorescence is shown in red (mCherry) and green (Venus). All images were taken from live cells in a Revolve Echo inverted microscope by stitching images with a 10x objective.

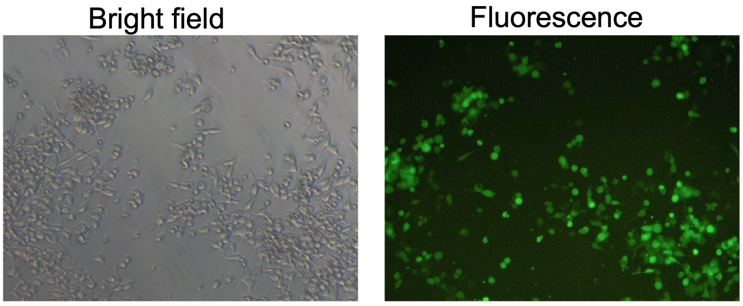

Supplementary figure 5. RGB marking of cultured cells with co-transfected ZIP14 and hFT onto HEK-293-6E cells. All images were taken from live cells in a Revolve Echo inverted microscope by stitching pictures with a 10x objective.

Supplementary table 1. Magnetosome strains were used for this project.

Strain	**Deletion phenotype**	**Source or reference**
M. gryphiswaldense MSR-1 R3/S1	Wild type	Schultheiss and Schüler 2003
ΔFe4	Reduced magnetite biomineralization	Kumari et al. 2014
Δ*feoAB1*	Reduced magnetite biomineralization	Heinke et al. 2017
Δ*feoAB12*	Reduced magnetite biomineralization	Present study
Δ*mamF*	Slightly smaller crystals	Lohße et al. 2014
Δ*mmsF*Δ*mamF*	Small amorphous crystals	Lohße et al. 2014
Δ*mamJ*	Magnetosome crystal aggregates	Scheffel et al. 2006
Δ*mamR*	Reduced size and number of magnetosomes	Lohße et al. 2014

Supplementary table 2. PCR primers used for Reverse Transcription- PCR (RT-PCR).

Gene name	Primer sequence (5'-3')
mms6	Forward GCCACCATGGGAGAAATGGA
	Reverse GGCGCTCTCGATATCTCTGG
magA	Forward GATCCCAGTGTGGTGGTACG
	Reverse CACCAAGCCAGGGTAGACAG

9. References

A multicenter, phase I/II trial of hepatic intra-arterial delivery of doxorubicin hydrochloride adsorbed to magnetic targeted carriers in patients with hepatocellular carcinoma. (2002). *European Journal of Cancer*, *38*, S18.

Abedi, M., Abolmaali, S. S., Abedanzadeh, M., Borandeh, S., Samani, S. M., & Tamaddon, A. M. (2019). Citric acid functionalized silane coupling versus post-grafting strategy for dual pH and saline responsive delivery of cisplatin by Fe3O4/carboxyl functionalized mesoporous SiO2 hybrid nanoparticles: A-synthesis, physicochemical and biological characterization. *Materials Science and Engineering: C*, *104*, 109922.

Al-Deen, F. N., Selomulya, C., Ma, C., & Coppel, R. L. (2014). Superparamagnetic nanoparticle delivery of DNA vaccine. *Methods in Molecular Biology (Clifton, N.J.)*, *1143*, 181–194.

Alexandrov, A. V., & Grotta, J. C. (2002). Arterial reocclusion in stroke patients treated with intravenous tissue plasminogen activator. *Neurology*, *59*, 862–867.

Alfaraj, D. N., Al Dahlawi, A. M., AlObaid, M. M., Aldukhayyil, T. R., & Al Rumaih, D. A. (2022). Metastatic Lung Adenocarcinoma: Unusual Presentation with Focal Neurological Deficit. *The American Journal of Case Reports*, *23*, e936342-1-e936342-5.

Alphandéry, E., Faure, S., Raison, L., Duguet, E., Howse, P. A., & Bazylinski, D. A. (2011). Heat Production by Bacterial Magnetosomes Exposed to an Oscillating Magnetic Field. *The Journal of Physical Chemistry C*, *115*, 18–22.

Alphandéry, E., Ngo, A. T., Lefèvre, C., Lisiecki, I., Wu, L. F., & Pileni, M. P. (2008). Difference between the Magnetic Properties of the Magnetotactic Bacteria and Those of the Extracted Magnetosomes: Influence of the Distance between the Chains of Magnetosomes. *The Journal of Physical Chemistry C*, *112*, 12304–12309.

Alphandéry, Edouard, Guyot, F., & Chebbi, I. (2012). Preparation of chains of magnetosomes, isolated from Magnetospirillum magneticum strain AMB-1 magnetotactic bacteria, yielding efficient treatment of tumors using magnetic hyperthermia. *International Journal of Pharmaceutics*, *434*, 444–452.

Ankamwar, B., Lai, T. C., Huang, J. H., Liu, R. S., Hsiao, M., Chen, C. H., & Hwu, Y. K. (2010). Biocompatibility of Fe(3)O(4) nanoparticles evaluated by in vitro cytotoxicity assays using normal, glia and breast cancer cells. *Nanotechnology*, *21*, 75102.

Arami, H., Teeman, E., Troksa, A., Bradshaw, H., Saatchi, K., Tomitaka, A., … Krishnan, K. M. (2017). Tomographic magnetic particle imaging of cancer targeted nanoparticles. *Nanoscale*, *9*, 18723–18730.

Bauer, L. M., Situ, S. F., Griswold, M. A., & Samia, A. C. S. (2015). Magnetic Particle Imaging Tracers: State-of-the-Art and Future Directions. *The Journal of Physical Chemistry Letters*, *6*, 2509–2517.

Berry, C. C., & Curtis, A. S. G. (2003). Functionalisation of magnetic nanoparticles for applications in biomedicine. *Journal of Physics D: Applied Physics*, *36*, R198.

Beyer, T., Bailey, D. L., Birk, U. J., Buvat, I., Catana, C., Cheng, Z., … Moser, E. (2021). Medical Physics and Imaging–A Timely Perspective. *Frontiers in Physics*, *9*. Retrieved from https://www.frontiersin.org/articles/10.3389/fphy.2021.634693

Biederer, S., Knopp, T., Sattel, T. F., Lüdtke-Buzug, K., Gleich, B., Weizenecker, J., … Buzug, T. M. (2009). Magnetization response spectroscopy of superparamagnetic nanoparticles for magnetic particle imaging. *Journal of Physics D: Applied Physics*, *42*, 205007.

Blakemore, R. P., Maratea, D., & Wolfe, R. S. (1979). Isolation and pure culture of a freshwater magnetic spirillum in chemically defined medium. *Journal of Bacteriology*, *140*, 720–729.

Brott, T. G., Haley, E. C., Levy, D. E., Barsan, W., Broderick, J., Sheppard, G. L., … Reed, R. (1992). Urgent therapy for stroke. Part I. Pilot study of tissue plasminogen activator administered within 90 minutes. *Stroke*, *23*, 632–640.

Buck, A. K., Halter, G., Schirrmeister, H., Kotzerke, J., Wurziger, I., Glatting, G., … Hetzel, M. (2003). Imaging proliferation in lung tumors with PET: 18F-FLT versus 18F-FDG. *Journal of Nuclear Medicine: Official Publication, Society of Nuclear Medicine*, *44*, 1426–1431.

Čampelj, S., Makovec, D., & Drofenik, M. (2009). Functionalization of magnetic nanoparticles with 3-aminopropyl silane. *Journal of Magnetism and Magnetic Materials*, *321*, 1346–1350.

Chen, J.-P., Yang, P.-C., Ma, Y.-H., Tu, S.-J., & Lu, Y.-J. (2012). Targeted delivery of tissue plasminogen activator by binding to silica-coated magnetic nanoparticle. *International Journal of Nanomedicine*, *7*, 5137–5149.

Chen, W., Jiang, L., Hu, Y., Fang, G., Yang, B., Li, J., … Hussain, Z. (2021). Nanomedicines, an emerging therapeutic regimen for treatment of ischemic cerebral stroke: A review. *Journal of Controlled Release: Official Journal of the Controlled Release Society*, *340*, 342–360.

Chertok, B., Moffat, B. A., David, A. E., Yu, F., Bergemann, C., Ross, B. D., & Yang, V. C. (2008). Iron oxide nanoparticles as a drug delivery vehicle for MRI monitored magnetic targeting of brain tumors. *Biomaterials*, *29*, 487–496.

Choyke, P. L., Kressel, H. Y., Axel, L., Gefter, W., Thickman, D., Arger, P. H., & Meranze, S. G. (1985). Vascular occlusions detected by magnetic resonance imaging. *Magnetic Resonance in Medicine*, *2*, 540–554.

Ciernik, I. F., Dizendorf, E., Baumert, B. G., Reiner, B., Burger, C., Davis, J. B., … Von Schulthess, G. K. (2003). Radiation treatment planning with an integrated positron emission and computer tomography (PET/CT): A feasibility study. *International Journal of Radiation Oncology, Biology, Physics*, *57*, 853–863.

Colasuonno, M., Palange, A. L., Aid, R., Ferreira, M., Mollica, H., Palomba, R., … Decuzzi, P. (2018). Erythrocyte-Inspired Discoidal Polymeric Nanoconstructs Carrying Tissue Plasminogen Activator for the Enhanced Lysis of Blood Clots. *ACS Nano*, *12*, 12224–12237.

Collen, D. (1980). On the regulation and control of fibrinolysis. Edward Kowalski Memorial Lecture. *Thrombosis and Haemostasis*, *43*, 77–89.

Collen, D., & Lijnen, H. R. (1995). Molecular basis of fibrinolysis, as relevant for thrombolytic therapy. *Thrombosis and Haemostasis*, *74*, 167–171.

Comanescu, C. (2022). Magnetic Nanoparticles: Current Advances in Nanomedicine, Drug Delivery and MRI. *Chemistry*, *4*, 872–930.

Correa, T., Presciliano, R., & Abreu, F. (2021). Why Does Not Nanotechnology Go Green? Bioprocess Simulation and Economics for Bacterial-Origin Magnetite Nanoparticles. *Frontiers in Microbiology*, *12*. Retrieved from https://www.frontiersin.org/journals/microbiology/articles/10.3389/fmicb.2021.718232

Crișan, G., Moldovean-Cioroianu, N. S., Timaru, D.-G., Andrieș, G., Căinap, C., & Chiș, V. (2022). Radiopharmaceuticals for PET and SPECT Imaging: A Literature Review over the Last Decade. *International Journal of Molecular Sciences*, *23*, 5023.

Dalla Palma, L. (2006). Tomorrow's radiologist: What future? *La Radiologia Medica*, *111*, 621–633.

Dar, M. I., & Shivashankar, S. A. (2013). Single crystalline magnetite, maghemite, and hematite nanoparticles with rich coercivity. *RSC Advances*, *4*, 4105–4113.

De Oliveira, E. P., Fiebach, J. B., Vagal, A., Schaefer, P. W., & Aviv, R. I. (2021). Controversies in Imaging of Patients With Acute Ischemic Stroke: *AJR* Expert Panel Narrative Review. *American Journal of Roentgenology*, *217*, 1027–1037.

Derksen, J. T. P., & Scherphof, G. L. (1985). An improved method for the covalent coupling of proteins to liposomes. *Biochimica et Biophysica Acta (BBA) - Biomembranes*, *814*, 151–155.

Dhavalikar, R., & Rinaldi, C. (2014). On the effect of finite magnetic relaxation on the magnetic particle imaging performance of magnetic nanoparticles. *Journal of Applied Physics*, *115*, 074308.

Doi Kunio, K. (2006). Diagnostic imaging over the last 50 years: Research and development in medical imaging science and technology. *Physics in Medicine and Biology*, *51*, R5-27.

Eberbeck, D., Wiekhorst, F., Wagner, S., & Trahms, L. (2011). How the size distribution of magnetic nanoparticles determines their magnetic particle imaging performance. *Applied Physics Letters*, *98*, 182502.

Elfick, A., Rischitor, G., Mouras, R., Azfer, A., Lungaro, L., Uhlarz, M., … Salter, D. M. (2017). Biosynthesis of magnetic nanoparticles by human mesenchymal stem cells following transfection with the magnetotactic bacterial gene mms6. *Scientific Reports*, *7*, 39755.

Elias, A., & Tsourkas, A. (2009). Imaging circulating cells and lymphoid tissues with iron oxide nanoparticles. *Hematology. American Society of Hematology. Education Program*, 720–726.

EMC. (12/13). *The Digital Universe Driving Data Growth in Healthcare*.

European Society of Radiology 2009. (2010). The future role of radiology in healthcare. *Insights into Imaging*, *1*, 2–11.

Feng, Q., Liu, Y., Huang, J., Chen, K., Huang, J., & Xiao, K. (2018). Uptake, distribution, clearance, and toxicity of iron oxide nanoparticles with different sizes and coatings. *Scientific Reports*, *8*, 2082.

Ferguson, R. M., Minard, K. R., & Krishnan, K. M. (2009). Optimization of nanoparticle core size for magnetic particle imaging. *Journal of Magnetism and Magnetic Materials*, *321*, 1548–1551.

Filippi, M., Rocca, M. A., De Stefano, N., Enzinger, C., Fisher, E., Horsfield, M. A., … Comi, G. (2011). Magnetic Resonance Techniques in Multiple Sclerosis: The Present and the Future. *Archives of Neurology*, *68*, 1514–1520.

Filler, A. (2009). The History, Development and Impact of Computed Imaging in Neurological Diagnosis and Neurosurgery: CT, MRI, and DTI. *Nature Precedings*, 1–1.

Flemmig, M., & Melzig, M. F. (2012). Serine-proteases as plasminogen activators in terms of fibrinolysis. *Journal of Pharmacy and Pharmacology*, *64*, 1025–1039.

Fletcher, A. P., Alkjaersig, N., Smyrniotis, F. E., & Sherry, S. (1958). The treatment of patients suffering from early myocardial infarction with massive and prolonged streptokinase therapy. *Transactions of the Association of American Physicians*, *71*, 287–296.

GBD 2019 Stroke Collaborators. (2021). Global, regional, and national burden of stroke and its risk factors, 1990-2019: A systematic analysis for the Global Burden of Disease Study 2019. *The Lancet. Neurology*, *20*, 795–820.

Giustini, A. J., Petryk, A. A., Cassim, S. M., Tate, J. A., Baker, I., & Hoopes, P. J. (2010). Magnetic nanoparticle hyperthermia in cancer treatment. *Nano LIFE*, *01*, 17–32.

Gleich, B., & Weizenecker, J. (2005). Tomographic imaging using the nonlinear response of magnetic particles. *Nature*, *435*, 1214–1217.

Glover, G. H. (2011). Overview of Functional Magnetic Resonance Imaging. *Neurosurgery Clinics of North America*, *22*, 133–139.

Graeser, M., Thieben, F., Szwargulski, P., Werner, F., Gdaniec, N., Boberg, M., … Knopp, T. (2019). Human-sized magnetic particle imaging for brain applications. *Nature Communications*, *10*, 1936.

Griese, F., Knopp, T., Gruettner, C., Thieben, F., Müller, K., Loges, S., … Gdaniec, N. (2020). Simultaneous Magnetic Particle Imaging and Navigation of large superparamagnetic nanoparticles in bifurcation flow experiments. *Journal of Magnetism and Magnetic Materials*, *498*, 166206.

Grøan, M., Ospel, J., Ajmi, S., Sandset, E. C., Kurz, M. W., Skjelland, M., & Advani, R. (2021). Time-Based Decision Making for Reperfusion in Acute Ischemic Stroke. *Frontiers in Neurology*, *12*, 728012.

Grüttner, C., Rudershausen, S., & Teller, J. (2001). Improved properties of magnetic particles by combination of different polymer materials as particle matrix. *Journal of Magnetism and Magnetic Materials*, *225*, 1–7.

Gunderman, R. B. (2005). The medical community's changing vision of the patient: The importance of radiology. *Radiology*, *234*, 339–342.

Hahn, M. A., Singh, A. K., Sharma, P., Brown, S. C., & Moudgil, B. M. (2011). Nanoparticles as contrast agents for in-vivo bioimaging: Current status and future perspectives. *Analytical and Bioanalytical Chemistry*, *399*, 3–27.

Haley, E. C., Levy, D. E., Brott, T. G., Sheppard, G. L., Wong, M. C., Kongable, G. L., … Marler, J. R. (1992). Urgent therapy for stroke. Part II. Pilot study of tissue plasminogen activator administered 91-180 minutes from onset. *Stroke*, *23*, 641–645.

Hao, H., Chen, Y., & Wu, M. (2021). Biomimetic nanomedicine toward personalized disease theranostics. *Nano Research*, *14*, 2491–2511.

Hein, C. D., Liu, X.-M., & Wang, D. (2008). Click Chemistry, A Powerful Tool for Pharmaceutical Sciences. *Pharmaceutical Research*, *25*, 2216–2230.

Heinke, D., Kraupner, A., Eberbeck, D., Schmidt, D., Radon, P., Uebe, R., … Briel, A. (2017). MPS and MRI efficacy of magnetosomes from wild-type and mutant bacterial strains. *International Journal on Magnetic Particle Imaging IJMPI*, *3*. Retrieved from https://www.journal.iwmpi.org/index.php/iwmpi/article/view/41

Hergt, R., Hiergeist, R., Zeisberger, M., Schüler, D., Heyen, U., Hilger, I., & Kaiser, W. A. (2005). Magnetic properties of bacterial magnetosomes as potential diagnostic and therapeutic tools. *Journal of Magnetism and Magnetic Materials*, *293*, 80–86.

Hermanson, G. T. (2013). *Bioconjugate Techniques*. Academic Press.

Heyen, U., & Schüler, D. (2003). Growth and magnetosome formation by microaerophilic Magnetospirillum strains in an oxygen-controlled fermentor. *Applied Microbiology and Biotechnology*, *61*, 536–544.

Hodson, N. J., Husband, J. E., & Macdonald, J. S. (1979). The role of computed tomography in the staging of bladder cancer. *Clinical Radiology*, *30*, 389–395.

Hong, R. Y., Feng, B., Chen, L. L., Liu, G. H., Li, H. Z., Zheng, Y., & Wei, D. G. (2008). Synthesis, characterization and MRI application of dextran-coated Fe3O4 magnetic nanoparticles. *Biochemical Engineering Journal*, *42*, 290–300.

Hussain, S., Mubeen, I., Ullah, N., Shah, S. S. U. D., Khan, B. A., Zahoor, M., … Sultan, M. A. (2022). Modern Diagnostic Imaging Technique Applications and Risk Factors in the Medical Field: A Review. *BioMed Research International*, *2022*, 5164970.

Inada, Y., Ohwada, K., Yoshimoto, T., Kojima, S., Takahashi, K., Kodera, Y., … Saito, Y. (1987). Fibrinolysis by urokinase endowed with magnetic property. *Biochemical and Biophysical Research Communications*, *148*, 392–396.

Jeng, H. A., & Swanson, J. (2006). Toxicity of metal oxide nanoparticles in mammalian cells. *Journal of Environmental Science and Health. Part A, Toxic/Hazardous Substances & Environmental Engineering*, *41*, 2699–2711.

Joseph, S., & Singh, E. (2023). Nuclear Medicine PET/CT Breast Cancer Assessment, Protocols, And Interpretation. In *StatPearls*. Treasure Island (FL): StatPearls Publishing.

Jurgons, R., Seliger, C., Hilpert, A., Trahms, L., Odenbach, S., & Alexiou, C. (2006). Drug loaded magnetic nanoparticles for cancer therapy. *Journal of Physics: Condensed Matter*, *18*, S2893.

Kalia, V., Leung, D. G., Sneag, D. B., Del Grande, F., & Carrino, J. A. (2017). Advanced MRI Techniques for Muscle Imaging. *Seminars in Musculoskeletal Radiology*, *21*, 459–469.

Kamarova, M., Baig, S., Patel, H., Monks, K., Wasay, M., Ali, A., … Bell, S. M. (2022). Antiplatelet Use in Ischemic Stroke. *The Annals of Pharmacotherapy*, *56*, 1159–1173.

Karlsson, H. L., Gustafsson, J., Cronholm, P., & Möller, L. (2009). Size-dependent toxicity of metal oxide particles—A comparison between nano- and micrometer size. *Toxicology Letters*, *188*, 112–118.

Kasban, H., El-Bendary, M. A. M., & Salama, D. H. (2015). *A Comparative Study of Medical Imaging Techniques*.

Khalid, K., Ahmad, R. E., Tong, A. Y. H., Lui, S. Y., & Abidin, I. Z. Z. (2021). Pathophysiology of streptokinase-induced hypotension in acute myocardial infarction: A systematic review of clinical evidence. *Archives of Medical Sciences. Atherosclerotic Diseases*, *6*, e85–e94.

Kherlopian, A. R., Song, T., Duan, Q., Neimark, M. A., Po, M. J., Gohagan, J. K., & Laine, A. F. (2008). A review of imaging techniques for systems biology. *BMC Systems Biology*, *2*, 74.

Kim, J. S., Yoon, T.-J., Yu, K. N., Kim, B. G., Park, S. J., Kim, H. W., … Cho, M. H. (2006). Toxicity and tissue distribution of magnetic nanoparticles in mice. *Toxicological Sciences: An Official Journal of the Society of Toxicology*, *89*, 338–347.

Kirschvink, J. L. (1989). Magnetite biomineralization and geomagnetic sensitivity in higher animals: An update and recommendations for future study. *Bioelectromagnetics*, *10*, 239–259.

Knopp, T., Szwargulski, P., Griese, F., Grosser, M., Boberg, M., & Möddel, M. (2019). MPIReco.jl: Julia Package for Image Reconstruction in MPI. *International Journal on Magnetic Particle Imaging IJMPI*, *5*.

Kohler, N., Fryxell, G. E., & Zhang, M. (2004). A Bifunctional Poly(ethylene glycol) Silane Immobilized on Metallic Oxide-Based Nanoparticles for Conjugation with Cell Targeting Agents. *Journal of the American Chemical Society*, *126*, 7206–7211.

Kolinko, I., Lohße, A., Borg, S., Raschdorf, O., Jogler, C., Tu, Q., … Schüler, D. (2014). Biosynthesis of magnetic nanostructures in a foreign organism by transfer of bacterial magnetosome gene clusters. *Nature Nanotechnology*, *9*, 193–197.

Kong, S. D., Lee, J., Ramachandran, S., Eliceiri, B. P., Shubayev, V. I., Lal, R., & Jin, S. (2012). Magnetic targeting of nanoparticles across the intact blood–brain barrier. *Journal of Controlled Release : Official Journal of the Controlled Release Society*, *164*, 49–57.

Kotb, E. (2014). The biotechnological potential of fibrinolytic enzymes in the dissolution of endogenous blood thrombi. *Biotechnology Progress*, *30*, 656–672.

Kratz, H., Taupitz, M., Ariza de Schellenberger, A., Kosch, O., Eberbeck, D., Wagner, S., … Schnorr, J. (2018). Novel magnetic multicore nanoparticles designed for MPI and other biomedical applications: From synthesis to first in vivo studies. *PLOS ONE*, *13*, 1–22.

Kraupner, A., Eberbeck, D., Heinke, D., Uebe, R., Schüler, D., & Briel, A. (2017). Bacterial magnetosomes – nature's powerful contribution to MPI tracer research. *Nanoscale*, *9*, 5788–5793.

Kumari, M., Widdrat, M., Tompa, É., Uebe, R., Schüler, D., Pósfai, M., … Hirt, A. M. (2014). Distinguishing magnetic particle size of iron oxide nanoparticles with first-order reversal curves. *Journal of Applied Physics*, *116*, 124304.

Lang, C., & Schüler, D. (2008). Expression of green fluorescent protein fused to magnetosome proteins in microaerophilic magnetotactic bacteria. *Applied and Environmental Microbiology*, *74*, 4944–4953.

Le Fèvre, R., Durand-Dubief, M., Chebbi, I., Mandawala, C., Lagroix, F., Valet, J.-P., … Alphandéry, E. (2017). Enhanced antitumor efficacy of biocompatible magnetosomes for the magnetic hyperthermia treatment of glioblastoma. *Theranostics*, *7*, 4618–4631.

LeRoux, P. D., Berger, M. S., Elliott, J. P., & Tamimi, H. K. (1991). Cerebral metastases from ovarian carcinoma. *Cancer*, *67*, 2194–2199.

Levenberg, D. R., Varon, E., Indech, G., Ben Uliel, T., Geri, L., Sharoni, A., & Shefi, O. (2023). A streptavidin–biotin system combined with magnetic actuators for remote neuronal guidance. *Journal of Biological Engineering*, *17*, 40.

Levine, E., Lee, K. R., Neff, J. R., Maklad, N. F., Robinson, R. G., & Preston, D. F. (1979). Comparison of Computed Tomography and Other Imaging Modalities in the Evaluation of Musculoskeletal Tumors1. *Radiology*.

Levy, D., Giustetto, R., & Hoser, A. (2012). Structure of magnetite (Fe3O4) above the Curie temperature: A cation ordering study. *Physics and Chemistry of Minerals*, *39*, 169–176.

Liu, F., Zhao, B., Krug, L. M., Ishill, N. M., Lim, R. C., Guo, P., … Schwartz, L. H. (2010). Assessment of therapy responses and prediction of survival in malignant pleural mesothelioma through computer-aided volumetric measurement on computed tomography scans. *Journal of Thoracic Oncology: Official Publication of the International Association for the Study of Lung Cancer*, *5*, 879–884.

Lohße, A., Borg, S., Raschdorf, O., Kolinko, I., Tompa, É., Pósfai, M., … Schüler, D. (2014). Genetic Dissection of the mamAB and mms6 Operons Reveals a Gene Set Essential for Magnetosome Biogenesis in Magnetospirillum gryphiswaldense. *Journal of Bacteriology*, *196*, 2658–2669.

Lohße, A., Ullrich, S., Katzmann, E., Borg, S., Wanner, G., Richter, M., … Schüler, D. (2011). Functional Analysis of the Magnetosome Island in Magnetospirillum gryphiswaldense: The mamAB Operon Is Sufficient for Magnetite Biomineralization. *PLOS ONE*, *6*, e25561.

Loren, M., García Frade, L. J., Torrado, M. C., & Navarro, J. L. (1989). Thrombus age and tissue plasminogen activator mediated thrombolysis in rats. *Thrombosis Research*, *56*, 67–75.

Löwa, N., Radon, P., Kosch, O., & Wiekhorst, F. (2016). Concentration Dependent MPI Tracer Performance. *International Journal on Magnetic Particle Imaging IJMPI*, *2*. Retrieved from https://www.journal.iwmpi.org/index.php/iwmpi/article/view/26

Ludewig, P., Gdaniec, N., Sedlacik, J., Forkert, N. D., Szwargulski, P., Graeser, M., … Magnus, T. (2017). Magnetic Particle Imaging for Real-Time Perfusion Imaging in Acute Stroke. *ACS Nano*, *11*, 10480–10488.

Lyon, J. L., Fleming, D. A., Stone, M. B., Schiffer, P., & Williams, M. E. (2004). Synthesis of Fe Oxide Core/Au Shell Nanoparticles by Iterative Hydroxylamine Seeding. *Nano Letters*, *4*, 719–723.

Massner, C. (2018). *Genetically controlled iron uptake and storage in mammalian cells for magnetic resonance imaging and magnetic actuation* (Technische Universität München). Technische Universität München.

Massoud, T. F., & Gambhir, S. S. (2003). Molecular imaging in living subjects: Seeing fundamental biological processes in a new light. *Genes & Development*, *17*, 545–580.

Mateo, C., Torres, R., Fernández-Lorente, G., Ortiz, C., Fuentes, M., Hidalgo, A., … Fernández-Lafuente, R. (2003). Epoxy-amino groups: A new tool for improved immobilization of proteins by the epoxy method. *Biomacromolecules*, *4*, 772–777.

Medical imaging in personalised medicine: A white paper of the research committee of the European Society of Radiology (ESR). (2015). *Insights into Imaging*, *6*, 141–155.

Mickoleit, F., Jörke, C., Geimer, S., S. Maier, D., P. Müller, J., Demut, J., … H. Clement, J. (2021). Biocompatibility, uptake and subcellular localization of bacterial magnetosomes in mammalian cells. *Nanoscale Advances*, *3*, 3799–3815.

Mickoleit, F., Lanzloth, C., & Schüler, D. (2020). A Versatile Toolkit for Controllable and Highly Selective Multifunctionalization of Bacterial Magnetic Nanoparticles. *Small*, *16*, 1906922.

Möddel, M., Meins, C., Dieckhoff, J., & Knopp, T. (2018). Viscosity quantification using multi-contrast magnetic particle imaging. *New Journal of Physics*, *20*, 083001.

Molwitz, I., Ittrich, H., Knopp, T., Mummert, T., Salamon, J., Jung, C., … Kaul, M. G. (2019). First magnetic particle imaging angiography in human-sized organs by employing a multimodal ex vivo pig kidney perfusion system. *Physiological Measurement*, *40*, 105002.

Moran, C. M., & Thomson, A. J. W. (2020). Preclinical Ultrasound Imaging—A Review of Techniques and Imaging Applications. *Frontiers in Physics*, *8*. Retrieved from https://www.frontiersin.org/articles/10.3389/fphy.2020.00124

Mosayebi, J., Kiyasatfar, M., & Laurent, S. (2017). Synthesis, Functionalization, and Design of Magnetic Nanoparticles for Theranostic Applications. *Advanced Healthcare Materials*, *6*, 1700306.

Moskowitz, B. M., Frankel, R. B., Flanders, P. J., Blakemore, R. P., & Schwartz, B. B. (1988). Magnetic properties of magnetotactic bacteria. *Journal of Magnetism and Magnetic Materials*, *73*, 273–288.

Mukhatov, A., Le, T.-A., Pham, T. T., & Do, T. D. (2023). A comprehensive review on magnetic imaging techniques for biomedical applications. *Nano Select*, *4*, 213–230.

Nascimento, D., Suchard, G., Hatem, M., & de Abreu, A. (2014). The role of magnetic resonance imaging in the evaluation of bone tumours and tumour-like lesions. *Insights into Imaging*, *5*, 419–440.

Niu, J., Wang, F., Zhu, X., Zhao, J., & Ma, J. (2014). One-pot synthesis of l -dopa-functionalized water-dispersible magnetite nano-palladium catalyst and its application in the Suzuki and Heck reactions in water: A novel and highly active catalyst. *RSC Advances*, *4*, 37761–37766.

Padma, M. V., Said, S., Jacobs, M., Hwang, D. R., Dunigan, K., Satter, M., … Mantil, J. C. (2003). Prediction of pathology and survival by FDG PET in gliomas. *Journal of Neuro-Oncology*, *64*, 227–237.

Phelps, M. E. (2000). Positron emission tomography provides molecular imaging of biological processes. *Proceedings of the National Academy of Sciences*, *97*, 9226–9233.

Pi, F., Sun, J., Liu, W., Sun, X., & Zhang, Y. (2017). Elimination of aflatoxin B1 in vegetable oil based on immuno-magnetosomes probes from a novel magnetotactic bacterium. *Food Control*, *80*, 319–326.

Plan Sangnier, A., Preveral, S., Curcio, A., K. A. Silva, A., Lefèvre, C. T., Pignol, D., … Wilhelm, C. (2018). Targeted thermal therapy with genetically engineered magnetite magnetosomes@RGD: Photothermia is far more efficient than magnetic hyperthermia. *Journal of Controlled Release*, *279*, 271–281.

Rahmer, J., Weizenecker, J., Gleich, B., & Borgert, J. (2009). Signal encoding in magnetic particle imaging: Properties of the system function. *BMC Medical Imaging*, *9*, 4.

Rahmer, J., Wirtz, D., Bontus, C., Borgert, J., & Gleich, B. (2017). Interactive Magnetic Catheter Steering With 3-D Real-Time Feedback Using Multi-Color Magnetic Particle Imaging. *IEEE Transactions on Medical Imaging*, *36*, 1449–1456.

Rangarajan, K., Das, C. J., Kumar, A., & Gupta, A. K. (2014). MRI in central nervous system infections: A simplified patterned approach. *World Journal of Radiology*, *6*, 716–725.

Raschdorf, O., Bonn, F., Zeytuni, N., Zarivach, R., Becher, D., & Schüler, D. (2018). A quantitative assessment of the membrane-integral sub-proteome of a bacterial magnetic organelle. *Journal of Proteomics*, *172*, 89–99.

Raschdorf, O., Plitzko, J. M., Schüler, D., & Müller, F. D. (2014). A Tailored galK Counterselection System for Efficient Markerless Gene Deletion and Chromosomal Tagging in Magnetospirillum gryphiswaldense. *Applied and Environmental Microbiology*, *80*, 4323–4330.

Ren, L., Wang, X., Wu, H., Shang, B., & Wang, J. (2010). Conjugation of nattokinase and lumbrukinase with magnetic nanoparticles for the assay of their thrombolytic activities. *Journal of Molecular Catalysis B: Enzymatic*, *62*, 190–196.

Rijken, D. C., Barrett-Bergshoeff, M. M., Jie, A. F. H., Criscuoli, M., & Sakharov, D. V. (2004). Clot penetration and fibrin binding of amediplase, a chimeric plasminogen activator (K2tu-PA). *Thrombosis and Haemostasis*, *91*, 52–60.

Rong, C., Huang, Y., Zhang, W., Jiang, W., Li, Y., & Li, J. (2008). Ferrous iron transport protein B gene (*feoB1*) plays an accessory role in magnetosome formation in *Magnetospirillum gryphiswaldense* strain MSR-1. *Research in Microbiology*, *159*, 530–536.

Rosenfeldt, S., Mickoleit, F., Jörke, C., Clement, J. H., Markert, S., Jérôme, V., … Schenk, A. S. (2021). Towards standardized purification of bacterial magnetic nanoparticles for future in vivo applications. *Acta Biomaterialia*, *120*, 293–303.

Roy, S., & Pericàs, M. A. (2009). Functionalized nanoparticles as catalysts for enantioselective processes. *Organic & Biomolecular Chemistry*, *7*, 2669–2677.

Salamon, J., Dieckhoff, J., Kaul, M. G., Jung, C., Adam, G., Möddel, M., … Ittrich, H. (2020). Visualization of spatial and temporal temperature distributions with magnetic particle imaging for liver tumor ablation therapy. *Scientific Reports*, *10*, 7480.

Saritas, E. U., Goodwill, P. W., Croft, L. R., Konkle, J. J., Lu, K., Zheng, B., & Conolly, S. M. (2013). Magnetic Particle Imaging (MPI) for NMR and MRI Researchers. *Journal of Magnetic Resonance (San Diego, Calif. : 1997)*, *229*, 116–126.

Saver, J. L. (2006). Time is brain—Quantified. *Stroke*, *37*, 263–266.

Scheffel, A., Gärdes, A., Grünberg, K., Wanner, G., & Schüler, D. (2008). The major magnetosome proteins MamGFDC are not essential for magnetite biomineralization in Magnetospirillum gryphiswaldense but regulate the size of magnetosome crystals. *Journal of Bacteriology*, *190*, 377–386.

Scheffel, A., Gruska, M., Faivre, D., Linaroudis, A., Plitzko, J. M., & Schüler, D. (2006). An acidic protein aligns magnetosomes along a filamentous structure in magnetotactic bacteria. *Nature*, *440*, 110–114.

Sheng, W., Wei, W., Li, J., Qi, X., Zuo, G., Chen, Q., … Dong, W. (2016). Amine-functionalized magnetic mesoporous silica nanoparticles for DNA separation. *Applied Surface Science*, *387*, 1116–1124.

Shrestha, B., Wang, L., Brey, E. M., Uribe, G. R., & Tang, L. (2021). Smart Nanoparticles for Chemo-Based Combinational Therapy. *Pharmaceutics*, *13*, 853.

Shubayev, V. I., Pisanic, T. R., & Jin, S. (2009). Magnetic nanoparticles for theragnostics. *Advanced Drug Delivery Reviews*, *61*, 467–477.

Sinnecker, T., Kuchling, J., Dusek, P., Dörr, J., Niendorf, T., Paul, F., & Wuerfel, J. (2015). Ultrahigh field MRI in clinical neuroimmunology: A potential contribution to improved diagnostics and personalised disease management. *EPMA Journal*, *6*, 16.

Steitz, B., Hofmann, H., Kamau, S. W., Hassa, P. O., Hottiger, M. O., von Rechenberg, B., … Petri-Fink, A. (2007). Characterization of PEI-coated superparamagnetic iron oxide nanoparticles for transfection: Size distribution, colloidal properties and DNA interaction. *Journal of Magnetism and Magnetic Materials*, *311*, 300–305.

Stevens, R. G., Jones, D. Y., Micozzi, M. S., & Taylor, P. R. (1988). Body iron stores and the risk of cancer. *The New England Journal of Medicine*, *319*, 1047–1052.

Suk, J. S., Xu, Q., Kim, N., Hanes, J., & Ensign, L. M. (2016). PEGylation as a strategy for improving nanoparticle-based drug and gene delivery. *Advanced Drug Delivery Reviews*, *99*, 28–51.

Sun, J.-B., Duan, J.-H., Dai, S.-L., Ren, J., Guo, L., Jiang, W., & Li, Y. (2008). Preparation and anti-tumor efficiency evaluation of doxorubicin-loaded bacterial magnetosomes: Magnetic nanoparticles as drug carriers isolated from Magnetospirillum gryphiswaldense. *Biotechnology and Bioengineering*, *101*, 1313–1320.

Szwargulski, P, Ludewig, P., Graeser, M., Möddel, M., Krishnan, K. M., Ittrich, H., … Knopp, T. (2018). Dynamic Multi-Colored Magnetic Particle Imaging of a Healthy Mouse using multiple Tracers. *World Molecular Imaging Congress (WMIC) 2018*.

Szwargulski, Patryk, Wilmes, M., Javidi, E., Thieben, F., Graeser, M., Koch, M., … Ludewig, P. (2020). Monitoring Intracranial Cerebral Hemorrhage Using Multicontrast Real-Time Magnetic Particle Imaging. *ACS Nano*, *14*, 13913–13923.

Tadayon, A., Jamshidi, R., & Esmaeili, A. (2015). Delivery of tissue plasminogen activator and streptokinase magnetic nanoparticles to target vascular diseases. *International Journal of Pharmaceutics*, *495*, 428–438.

Tanaka, Y., Nakagomi, N., Doe, N., Nakano-Doi, A., Sawano, T., Takagi, T., … Nakagomi, T. (2020). Early Reperfusion Following Ischemic Stroke Provides Beneficial Effects, Even After Lethal Ischemia with Mature Neural Cell Death. *Cells*, *9*, 1374.

Tang, Z., Li, D., Wang, X., Gong, H., Luan, Y., Liu, Z., … Chen, H. (2015). A t-PA/nanoparticle conjugate with fully retained enzymatic activity and prolonged circulation time. *Journal of Materials Chemistry B*, *3*, 977–982.

Taukulis, R., Widdrat, M., Kumari, M., Heinke, D., Rumpler, M., Tompa, É., … Faivre, D. (2015). *Magnetic iron oxide nanoparticles as MRI contrast agents—A comprehensive physical and theoretical study*. *51*, 721–748.

Tay, Z. W., Chandrasekharan, P., Chiu-Lam, A., Hensley, D. W., Dhavalikar, R., Zhou, X. Y., … Conolly, S. M. (2018). Magnetic Particle Imaging-Guided Heating in Vivo Using Gradient Fields for Arbitrary Localization of Magnetic Hyperthermia Therapy. *ACS Nano*, *12*, 3699–3713.

Teja, A. S., & Koh, P.-Y. (2009). Synthesis, properties, and applications of magnetic iron oxide nanoparticles. *Progress in Crystal Growth and Characterization of Materials*, *55*, 22–45.

Thelwell, C., & Longstaff, C. (2007). The regulation by fibrinogen and fibrin of tissue plasminogen activator kinetics and inhibition by plasminogen activator inhibitor 1. *Journal of Thrombosis and Haemostasis: JTH*, *5*, 804–811.

Thieben, F., Mickoleit, F., Tessaro, S., Ludewig, P., Schüler, D., Garbayo, J. R., … Knopp, T. (2023). Development of Optimized Magnetic Particle Imaging Tracers Utilizing Genetically Engineered Magnetosomes. *International Journal on Magnetic Particle Imaging IJMPI*, *9*.

Timko, M., Dzarova, A., Kovac, J., Skumiel, A., Józefczak, A., Hornowski, T., … Tomasovicova, N. (2009). Magnetic properties and heating effect in bacterial magnetic nanoparticles. *Journal of Magnetism and Magnetic Materials*, *321*, 1521–1524.

Tomitaka, A., Ferguson, R. M., Khandhar, A. P., Kemp, S. J., Ota, S., Nakamura, K., … Krishnan, K. M. (2015). Variation of Magnetic Particle Imaging Tracer Performance With Amplitude and Frequency of the Applied Magnetic Field. *IEEE Transactions on Magnetics*, *51*, 6100504.

Tsien, R. Y. (2003). Imagining imaging's future. *Nature Reviews. Molecular Cell Biology*, *Suppl*, SS16-21.

Tural, B., Tural, S., Ertaş, E., Yalınkılıç, İ., & Demir, A. S. (2013). Purification and covalent immobilization of benzaldehyde lyase with heterofunctional chelate-epoxy modified magnetic nanoparticles and its carboligation reactivity. *Journal of Molecular Catalysis B: Enzymatic*, *95*, 41–47.

Turcheniuk, K., Tarasevych, A. V., Kukhar, V. P., Boukherroub, R., & Szunerits, S. (2013). Recent advances in surface chemistry strategies for the fabrication of functional iron oxide based magnetic nanoparticles. *Nanoscale*, *5*, 10729–10752.

Uebe, R., & Schüler, D. (2016). Magnetosome biogenesis in magnetotactic bacteria. *Nature Reviews. Microbiology*, *14*, 621–637.

Valko, M., Leibfritz, D., Moncol, J., Cronin, M. T. D., Mazur, M., & Telser, J. (2007). Free radicals and antioxidants in normal physiological functions and human disease. *The International Journal of Biochemistry & Cell Biology*, *39*, 44–84.

Veranth, J. M., Kaser, E. G., Veranth, M. M., Koch, M., & Yost, G. S. (2007). Cytokine responses of human lung cells (BEAS-2B) treated with micron-sized and nanoparticles of metal oxides compared to soil dusts. *Particle and Fibre Toxicology*, *4*, 2.

Verstraete, M. (2000). Third-generation thrombolytic drugs. *The American Journal of Medicine*, *109*, 52–58.

Wang, Q., Ma, X., Liao, H., Liang, Z., Li, F., Tian, J., & Ling, D. (2020). Artificially Engineered Cubic Iron Oxide Nanoparticle as a High-Performance Magnetic Particle Imaging Tracer for Stem Cell Tracking. *ACS Nano*, *14*, 2053–2062.

Wardlaw, J. M., Zoppo, G., Yamaguchi, T., & Berge, E. (2003). Thrombolysis for acute ischaemic stroke. *The Cochrane Database of Systematic Reviews*, CD000213.

Wawrzik, T., Ludwig, F., & Schilling, M. (2012). Magnetic Particle Imaging: Exploring Particle Mobility. In T. M. Buzug & J. Borgert (Eds.), *Magnetic Particle Imaging* (pp. 21–25). Berlin, Heidelberg: Springer.

Weber, K. (2007, June 29). Lentiviral Gene Ontology Vectors.

Weissleder, R., Kelly, K., Sun, E. Y., Shtatland, T., & Josephson, L. (2005). Cell-specific targeting of nanoparticles by multivalent attachment of small molecules. *Nature Biotechnology*, *23*, 1418–1423.

Weissleder, R., & Pittet, M. J. (2008). Imaging in the era of molecular oncology. *Nature*, *452*, 580–589.

Weizenecker, J., Borgert, J., & Gleich, B. (2007). A simulation study on the resolution and sensitivity of magnetic particle imaging. *Physics in Medicine & Biology*, *52*, 6363.

Weizenecker, Juergen, Gleich, B., & Borgert, J. (2008). Magnetic particle imaging using a field free line. *Journal of Physics D: Applied Physics*, *41*, 105009.

Widder, K. J., Senyei, A. E., & Ranney, D. F. (1979). Magnetically responsive microspheres and other carriers for the biophysical targeting of antitumor agents. *Advances in Pharmacology and Chemotherapy*, *16*, 213–271.

Widder, K. J., Senyel, A. E., & Scarpelli, G. D. (1978). Magnetic microspheres: A model system of site specific drug delivery in vivo. *Proceedings of the Society for Experimental Biology and Medicine. Society for Experimental Biology and Medicine (New York, N.Y.)*, *158*, 141–146.

Wu, L. C., Zhang, Y., Steinberg, G., Qu, H., Huang, S., Cheng, M., … Wintermark, M. (2019). A Review of Magnetic Particle Imaging and Perspectives on Neuroimaging. *AJNR. American Journal of Neuroradiology*, *40*, 206–212.

Yang, H.-W., Hua, M.-Y., Lin, K.-J., Wey, S.-P., Tsai, R.-Y., Wu, S.-Y., Ma, Y.-H. (2012). Bioconjugation of recombinant tissue plasminogen activator to magnetic nanocarriers for targeted thrombolysis. *International Journal of Nanomedicine*, *7*, 5159–5173.

Yin, L., Li, W., Du, Y., Wang, K., Liu, Z., Hui, H., & Tian, J. (2022). Recent developments of the reconstruction in magnetic particle imaging. *Visual Computing for Industry, Biomedicine, and Art*, *5*, 24.

Zhang, X., Le, T.-A., & Yoon, J. (2017). Development of a real time imaging-based guidance system of magnetic nanoparticles for targeted drug delivery. *Journal of Magnetism and Magnetic Materials*, *427*, 345–351.

Zhang, Y., Ni, Q., Xu, C., Wan, B., Geng, Y., Zheng, G., … Lu, G. (2019). Smart Bacterial Magnetic Nanoparticles for Tumor-Targeting Magnetic Resonance Imaging of HER2-Positive Breast Cancers. *ACS Applied Materials & Interfaces*, *11*, 3654–3665.

Zheng, B., Vazin, T., Goodwill, P. W., Conway, A., Verma, A., Ulku Saritas, E., … Conolly, S. M. (2015). Magnetic Particle Imaging tracks the long-term fate of in vivo neural cell implants with high image contrast. *Scientific Reports*, *5*, 14055.

Zhou, X. Y., Tay, Z. W., Chandrasekharan, P., Yu, E. Y., Hensley, D. W., Orendorff, R., … Conolly, S. M. (2018). Magnetic particle imaging for radiation-free, sensitive and high-contrast vascular imaging and cell tracking. *Current Opinion in Chemical Biology*, *45*, 131–138.

Ziemian, S., Löwa, N., Kosch, O., Bajj, D., Wiekhorst, F., & Schütz, G. (2018). Optimization of Iron Oxide Tracer Synthesis for Magnetic Particle Imaging. *Nanomaterials*, *8*, 180.

Zurkiya, O., Chan, A. W. S., & Hu, X. (2008). MagA is sufficient for producing magnetic nanoparticles in mammalian cells, making it an MRI reporter. *Magnetic Resonance in Medicine*, *59*, 1225–1231.

10. List of Figures and tables

11. Useful definitions for magnetism

Amplitude is the distance between the wave's resting position and its maximum displacement. Meter is the SI unit.

Drive field or excitation field: MPI generates an excitation field by the drive or send coils, that can magnetize the particles within their dynamic magnetization range.

Frequency: is the number of waves that pass by a specific point per second. Hertz (Hz) is the SI unit.

Gradient field or selection field: MPI generates a static magnetic field, highly inhomogeneous in space by a pair of permanent magnets or coils in Maxwell configuration (the gradient or selection coils). These opposing magnetic fields compensate for each other, developing one special location characterized by a magnetic field magnitude of zero. This area created by the drive field coils is named field free field (FFP) or a field free line (FFL).

Harmonics: any complex periodical signal can be acquired as the sum of the different "pure" sinusoidal waves at different frequencies and amplitudes, multiples of the fundamental frequency (also known as 1st Harmonic). These multiples of the fundamental frequency are called higher harmonics. For symmetrical waveforms, only odd harmonics (3rd,5th, 7th, etc.) appear.

Harmonics spectrum: is a graphical representation of the previous concept, where decomposition of distorted signal can be easily analyzed.

Langevin theory: the magnetization of superparamagnetic materials saturates quickly when magnetic induction increases.

Magnetic anisotropy: the dependence of magnetic properties on a preferred crystallographic direction, and it depends on the particles' crystalline, shape and surface structure. The anisotropy of a magnetic material is responsible for the preferred orientation of the magnetic moments in space.

Magnetic gradient field: situation whenever a magnetic field differs in magnitude or direction between two points in space. The magnetic flux lines are not parallel and converge or diverge within this region of space.

Magnetic moment: Is a vector that describes the tendency of a molecule, atom, nucleus, or subatomic particle, to interact with an external magnetic field.

Magnetic relaxation: is the phenomenon in which the magnetization approaches an equilibrium or steady-state condition when the magnetic field is changed. Magnetic relaxation is not instantaneous, and the characteristic time to reach the new state is also known as relaxation time.

Magnetic saturation: refers to when the maximum magnetic moment per unit of volume for a magnetic material is reached. Further increasing of the external field has no effect on the material's magnetization.

Magnetic susceptibility: measures how much a material will become magnetized with an externally applied magnetic field.

Oscillating magnetic field: is created by electromagnets of alternating current, then the intensity varies periodically according to the frequency, defining a sinusoidal wave.

Static magnetic field: is created by magnets or charges that move at a steady flow.

Superparamagnetism: is a magnetic behavior of small, single-domain magnetic particles without magnetic memory. In the presence of a magnetic field, the magnetic moments tend to align in the field direction with a significant magnetization of the whole set of particles. In the absence of a magnetic field, the magnetic moments of the particles are randomly oriented, and they do not retain any magnetization. It is more closely related to ferromagnetism than to paramagnetism.

12. Acknowledgments

The research work for this thesis was performed between March 2020 and August 2023 in the ERSI laboratory, Neurology Department, at the University Medical Center Hamburg-Eppendorf. These were three and a half quite intense years, and I am very grateful for all the support and help I received from my colleagues, collaborators, family, and friends. Thanks to Prof. Tim Magnus and Dr.med. Peter Ludewig for letting me join the ERSI lab and start my PhD. The doctoral years were hard, but I am very happy that I spent them in this lab. Thanks!

Thanks to my ERSI colleagues, past and present members. Especially thanks to Duan, you taught me everything and guided me at the very beginning of the project. Many thanks to Fynn and Florian. It was a pleasure to spend many hours collaborating on our projects. Danke Katrin for all the support, it took time to understand each other, but we know each other better now. PD.Dr. Berta Puig, gràcies per tota la teva ajuda, consells i perroterapia. Huge thanks to the lunch team, my fashionista Hind, my dear Lynn, my brilliant Karo.D, and my formidable best friend Santra Rebbeca. Thanks Santra for all the support, loads of laughs, and memorable moments I will keep in my heart forever.

Thanks to all my friends we have met in Hamburg, Gino, Ida, Dani, Cristian, and Anastasia, you made the beginning of my PhD smoother and funnier. Also thanks to my Spanish Crew por todo el apoyo y el cariño que me habeis dado, y me seguis dando. Joana gràcies per convidar-me a WeWork, moltes línies d'aquest treball han sigut escrites veient com et passejaves a la teva oficina fent res. Many many thanks to all my lifelong Cintruénigo friends, por vuestra alegría y apoyo en cada vuelta a casa. Gracias Andrea, por ser incansable y atenta conmigo. Siempre hemos estado cerca, pero ahora lo estamos más.

Gracias Mamá, Papa, Jorge y Daniel. Gracias yayo, eres el que más confiaste en mí. Gracias Edu por tu imparable apoyo en todo lo que hago, hacer que tengamos el mejor y mas envidiado hogar en Hamburgo. Por todas las aventuras que nos quedan!.

Many thanks to everyone!!

13. *Curriculum Vitae*

CV is omitted for data protection reasons

CV is omitted for data protection reasons

14. Eidesstattliche Versicherung

Ich versichere ausdrücklich, dass ich die Arbeit selbständig und ohne fremde Hilfe, insbesondere ohne entgeltliche Hilfe von Vermittlungs- und Beratungsdiensten, verfasst, andere als die von mir angegebenen Quellen und Hilfsmittel nicht benutzt und die aus den benutzten Werken wörtlich oder inhaltlich entnommenen Stellen einzeln nach Ausgabe (Auflage und Jahr des Erscheinens), Band und Seite des benutzten Werkes kenntlich gemacht habe. Das gilt insbesondere auch für alle Informationen aus Internetquellen.

Soweit beim Verfassen der Dissertation KI-basierte Tools („Chatbots“) verwendet wurden, versichere ich ausdrücklich, den daraus generierten Anteil deutlich kenntlich gemacht zu haben. Die „Stellungnahme des Präsidiums der Deutschen Forschungsgemeinschaft (DFG) zum Einfluss generativer Modelle für die Text- und Bilderstellung auf die Wissenschaften und das. Förderhandeln der DFG“ aus September 2023 wurde dabei beachtet. Ferner versichere ich, dass ich die Dissertation bisher nicht einem Fachvertreter an einer anderen Hochschule zur Überprüfung vorgelegt oder mich anderweitig um Zulassung zur Promotion beworben habe.

Ich erkläre mich damit einverstanden, dass meine Dissertation vom Dekanat der Medizinischen. Fakultät mit einer gängigen Software zur Erkennung von Plagiaten überprüft werden kann.

Unterschrift: ....